Voltage Induced Spreading and Liquid Optical Devices

Naresh Sampara

A thesis submitted in partial fulfilment of

the requirements of

Nottingham Trent University

for the degree of Doctor of Philosophy

August 1, 2013

A theory can be proved by experiment but no path leads from experiment to the birth of a theory.

Albert Einstein

This thesis is dedicated to my grand pa Late Mr Papa Rao Sampara.

Acknowledgements

I would like to start by thanking Nottingham Trent University for giving a such wonderful opportunity to pursuit a PhD in liquid physics and for funding. I would like to thank Prof Carl Brown and Prof Glen McHale for their support and theoretical ideas which helped me to gain three publications.

Thanks to Dr Carl Evans, Dr Gary Wells, Dr Ian Sage, Dr Neil Shirtcliffe and Dr Christophe Trabi for their excellent advices on experimental techniques which helped me to extend my knowledge in liquid optics during formal and informal meetings.

I would also like to thank Dr Fouzia Ouali, Dr Michael Newton, Dr Haida Liang, Dr David Fairhurst, Dr Steve Elliott and Dave Parker for their expertise and advice in experimental techniques and data analysis. I would like to take the opportunity to thank my colleagues individually for fruitful discussions: Haadi Javed, Fahad Shamim, Christopher Hamlett, Nicasio Geraldi, Yohana Msambwa, Amy Green and Rob Morris.

Finally I would like to thank my family members who are always very special to me: my dad Chinna rao, my mom Durga, my elder sister Hyma, her husband Suresh, my younger sister Aruna, her husband Narasimha rao and my fiancee Mrudula as well as Raghu, Chandu, Sundar and Babitha for their unconditional love.

I would like to thank my friends Pavan, Madhu, Prakash, Anand and Shanti for their weirdest discussions with a glass of wine and a piece of meat.

Abstract

An experimental investigation has been carried out into Liquid dielectrophoresis (LDEP), in which dielectric forces are used to actuate bulk liquid spreading and to imprint a deformation pattern at a liquid air surface. Our basic configuration uses a set of co-planar stripe interdigital electrodes to create a non-uniform A.C. electric field that exponentially decays in amplitude and penetrates above the structure into a dielectric liquid droplet. Dielectric forces drive a voltage-induced spreading of the droplet into a low contact angle droplet/film, an effect which will be referred to here as "dielectrowetting". Further application of the A.C. voltage to the electrodes results in a static sinusoidal wrinkle forming at the oil-air interface on the spread film.

Three main areas of investigations are reported, the first of which is a study of the statics and dynamics of the voltage induced spreading of a stripe of the material 1,2 propylene glycol. In the limit of thick droplets, a theoretical prediction has been derived that the cosine of the static equilibrium contact angle is proportional to the square of the amplitude of the voltage applied to the interdigital electrodes. This relationship is analogous to that found for electrowetting-on-dielectric (EWOD). Experimental observations confirm this predicted dielectrowetting behavior for the advancing static contact angle of the voltage induced spreading of a stripe of the material 1,2 propylene glycol. The predicted scaling relationship with the electrode dimensions has been confirmed for electrodes of linewidth 20 μm, 40 μm and 80 μm. It is also shown that with an appropriate surface treatment the induced wetting is made reversible. The dynamic contact angle (θ^o) of the liquid droplet was also measured as a function of voltage during spreading and the results are found to agree with the predictions of the Hoffman-de-Gennes macroscopic viscous dissipation approach extended to account for the electric field. Three distinct regimes have been investigated experimentally and

theoretically: partial wetting and exponential approach to equilibrium shape, spreading to complete wetting obeying a Tanner's law relationship, and super-spreading towards a complete wetting film.

The second area is the fabrication of the solid phase transmission grating with a minimized zeroth order using LDEP and a UV curable liquid resin. A new electric-field assisted approach to fabricate solid diffractive optical devices is demonstrated in which the optical properties of the device can be tuned by adjusting the applied voltage whilst the optical medium is in its liquid phase. Continuous adjustment of the voltage, and hence the optical diffraction pattern, during UV curing can produce a solid grating with suppressed intensity of the transmitted zero order.

The third area is a study of the dynamics of the formation of a periodic wrinkle deformation at the oil-air interface on a spread dielectric liquid film. An experimental study of how the switch on time t_{on} and the switch off/relaxation time t_{off} of the wrinkle scales as a function of the applied voltage V is presented. The amplitude A(V, t) of the wrinkle as a function of time was obtained from fitting the time dependent intensities of the positive zeroth, first and second diffracted orders of laser light transmitted through the oil film assuming that it acts as a thin sinusoidal phase grating. The results for relaxation have been compared with an analytical expression for t_{off} that has been derived by considering the LaPlace pressure restoring force at the oil-air interface under a creeping flow approximation.

Contents

List of Figures

List of Tables

Notations

The main variables used throughout this work are listed in this section unless otherwise stated.

n - Refractive index

η - Viscosity of the liquid

ε_r - Relative permittivity

ε_o - Vacuum permittivity

γ_{LV} - Liquid-vapour interfacial tension

γ_{SV} - Solid-vapour interfacial tension

γ_{SL} - Solid-Liquid interfacial tension

F - Surface energy

θ - Contact angle of the droplet

θ_{eq} - Equilibrium contact angle of a droplet when a voltage is applied

θ_y -Equilibrium contact angle of a droplet at no voltage is applied

$\theta(t)$ - Dynamic contact angle

S_{eq} - Equilibrium spreading coefficient

δ - Penetration depth

k - Wave number

λ_c - Capillary number E - Electric field

V - Applied voltage

V_{rms} - Root mean square voltage

W_E - Electrostatic energy

C - Capacitance

d - Electrode width

p - Electrode pitch

t - Time

Ω - Volume of the droplet

x_o - Width of the droplet

r_c - radius of the droplet

F_{DEP} - Dielectrophoresis force

$V_E(t)$ - Three phase contact line speed

q - Diffraction order

θ_q - Diffraction angle

η_q - Diffraction efficiency

m - Phase delay

λ - Wave length of the light

$\lambda_{material}$ - Wave length of the light in the material

$n_{material}$ - Refractive index of the material

n_{air} - Refractive index of the air

h - Thickness of the oil layer

A - Peak-peak amplitude of the wrinkle

τ - Wrinkle switch off time

t_{on} - Wrinkle switch on time

OPL - Optical path length

OPD - Optical path difference

A_{LV} - An area of liquid-vapor interface

A_{LS} - An area of liquid-solid interface

A_{∞} - Area of infinite space

Abbreviation

EW - ElectroWetting

EWOD - Electrowetting on Dielectric

DEP - DiElectroPhoresis

L-DEP - Liquid-DiElectroPhoresis

DSA - Drop Shape Analysis

IDT - InterDigiTated electrodes

IPA - IsoPropyl Alcohol

HMDS - HexaMethylDiSilazane

ITO - Indium Tin Oxide

AC - Alternative Current

LVDT - Linear Variable Differential Transformer

Chapter 1

Introduction

1.1 Motivation

In micrometre scale, a liquid will be dominated by the three interfacial tensions (such as liquid-vapour, solid-vapour and liquid-solid interfacial tensions), rather than gravitational force. For example, when a droplet is dispensed on a solid surface or a liquid layer, immediately it will adopt a shape of a spherical cap or a thin layer depends on the size of the droplet and liquid properties. These Interfacial tensions play a key role in various applications including Lab on a chip, painting, inkjet printing, liquid optics, cosmetics, and pharmaceuticals. Perhaps, let's discuss the main issue in lab on a chip, due to the interfacial tensions of the liquids microfluidic device requires an external pumping mechanism to transport liquid within a chip; such as syringe pump mechanism, peristaltic pump mechanism or pneumatic pump mechanism [5–8]. However these methods cause the increase in the final size of the detective device. Likewise, in inkjet printing, paint and liquid optics applications, if the droplet size is less than the capillary length of the droplet then it will not completely spread on the solid surface and have substantial contact angle.

To overcome these problems, after significant efforts researchers have been developed different methods such as surface gradient, electrowetting on dielectric (EWOD) and liquid Dielectrophoresis (LDEP) [9, 29, 78, 80]. In surface gradient method, increase in surface energy enables the liquid to flow through the channels or to increase the wetting on the solid surface. Nevertheless it is irreversible process. In Electrowetting on dielectric method the surface energy is altered if it is positioned on an electrode with an applied potential, therefore the wetting on the solid or flow through the channels are increased. EWOD method describes a configuration where a dielectric layer (insulating layer) become estranged a conductive liquid and an electrode. The disadvantages of this method are a conductive liquid is essential and liquid is in contact with an electrode which might lead contamination. In contrast Liquid dielectrophoresis method is in which di-

electric forces are used to actuate bulk liquid spreading on the solid surface and transmitting through the microfluidic channels. Unlike electrowetting method this is a contactless method (where the liquid is not in contact with the external electrodes) and either dielectric or conductive liquids can be used. Mainly LDEP used in biological applications including Lab-on-a-chip (LOC) for separation, mixing and transporting the micro/nano particles with in a micro channels and in optical applications such as variable lens, beam splitter and micro lens array[1, 9–11].

This thesis focuses on a dielectric liquid spreading using liquid Dielectrophoresis. Three main areas of investigations are discussed below.

Project A:

Chang et al. and Wang et al. illustrated that the LDEP can be used to fabricate the variable focal lens and the micro lens array [12, 13]. The theoretical relationship to contact angle and applied voltage has not been elucidated. Therefore, here, we have motivated to understand the relationship between the contact angle of the droplet and the applied voltage. Then we have initiated by using the below research questions.

Research questions 1a:

- In LDEP approach, what is the relationship between the static contact angle of the droplet and experimental parameters such as applied voltage, electrode geometry and dielectric liquid properties include surface tension, dielectric constant?
- Is the relationship similar to the EWOD?
- How can an isotropic spreading can be produced with a dielectric liquid droplet using LDEP?

These research questions have been reported in chapter 3 and also have explained the initial observation of the liquid spreading in other immiscible liquid.

Once we have shown the relation between the static contact angle and the applied voltage. We were keen to study how the dynamic contact angle of the droplet evolves as a function of applied voltage. Previously De-Gennes and Tanner showed the rate of spreading of a small viscous liquid depends on the viscous force and interfacial tensions, and it was proved using silicone oil spreading on a glass and silicone substrate [14–16]. What is missing so far that how the dynamic contact behaves in presence of electric field (either LDEP or EWOD)? To understand that we have started looking for answers for below research questions

Research question 1b:

- Using LDEP, the wetting (either partial or complete wetting) can be controlled by adjusting the applied voltage. How the dynamic contact angle is varied as a function of time at higher voltages and lower voltages.
- Does it follows the de-Gennes approach and Tanner's law at complete wetting regime?
- In the absence of LDEP, how the shape of the liquid changes as the liquid de-wets from complete wetting or partial wetting?

This research questions have been described in chapter 4 and also the theoretical prediction have elucidated by experimentally.

Project B:

Brown et al. reported a novel approach to produce a static wrinkle at air/oil interface using a dielectrophoretic force and this force was produced by applying a constant voltage to the interdigitated electrode array, of coplanar strip electrodes [17, 18]. Wrinkles, are static and stable, has been created at the surface of a thin film of oil and this phenomena been exploited to create a voltage programmable diffractive optical device. The amplitude of the wrinkle is directly proportional

to the applied voltage square for a range of oil layer thickness and line width of electrodes. Well the peak to peak amplitude of the wrinkle depends on the voltage and liquid properties, but the dynamics of the wrinkle has not been studied such as how fast the wrinkle can evolve and decay. More research questions are given in below.

Research questions 2:

- How can switching and relaxation of the wrinkle be characterised?
- Is there a relationship between the switching or relaxation time and experimental parameters including electrode geometry, applied voltage, thickness of the liquid and liquid properties?

I have discussed these research questions in chapter 6 and, however it has needed a further study to conclude them.

Previously researchers has been achieved the polymer surface patterns using electrohydrodynamic instabilities and this instability was produced by applying a voltage between two plates where one plate of a capacitor structure with a thin film of polymer melt [19–21]. However these patterns are irregular and challenging to produce the gratings with minimised zeroth order. Therefore we have used our approach to fabricate the solid gratings where the optical properties were controlled in liquid state. Therefore we have originated the study by looking for answers of below research questions.

Research questions 3:

- Using dieletrophoresis force, the solid grating with minimised zeroth order can be fabricated.
- How non uniform electric fields and the accompanying dielectrophoresis forces can be used to create a periodic phase grating of desired amplitude and desired optical properties in a liquid UV curable material which can be set to a solid using UV light to create a permanent diffraction grating?

These research questions have been reported in chapter 5.

1.2 Liquid properties

1.2.1 Surface Tension

Surface tension is a physical quantity whereby the liquid appears to be covered with a thin elastic membrane in steady state and it is measured by acting force per unit length. The cohesive force between the molecules in the liquid is equally distributed in all directions with neighbouring molecules. However the molecules at the surface of the liquid are exhibiting the strong attractive force on the inner molecules, and results of a thin elastic membrane at the surface as shown in figure 1.1. The surface tension is a restorative force which acts to reduce the surface area of the liquid [22, 23].

De-Gennes defined the surface tension as the energy that must be supplied to increase the surface area by one unit [32]. Arthur W Adamson has explained the

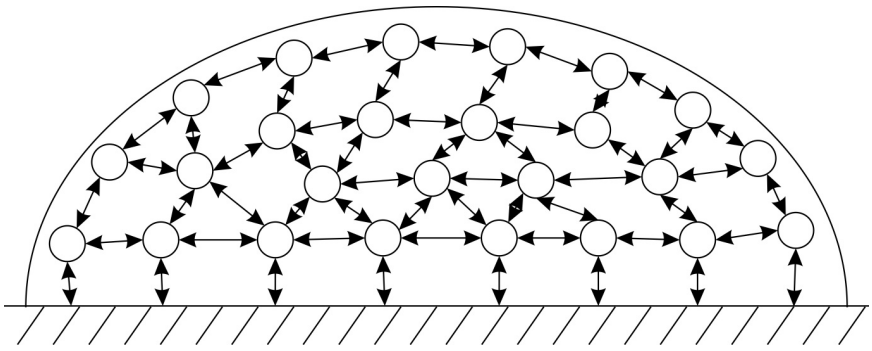

Figure 1.1: Schematic illustration of the molecular interaction in the liquid and at the boundaries of the liquid.

surface tension by considering a soap film stretched on a wire frame where one of the ends of the frame is movable as shown in figure 1.2 [22]. The work is done to stretch the soap film by the amount of dx and surface tension is, the restorative force, on the sliding bar of the frame in the opposite direction to the stretching. This is given by the equation

$$workdone = \gamma l dx = \gamma dA \tag{1.1}$$

Where, γ is referred as surface tension, A is the area of the frame.

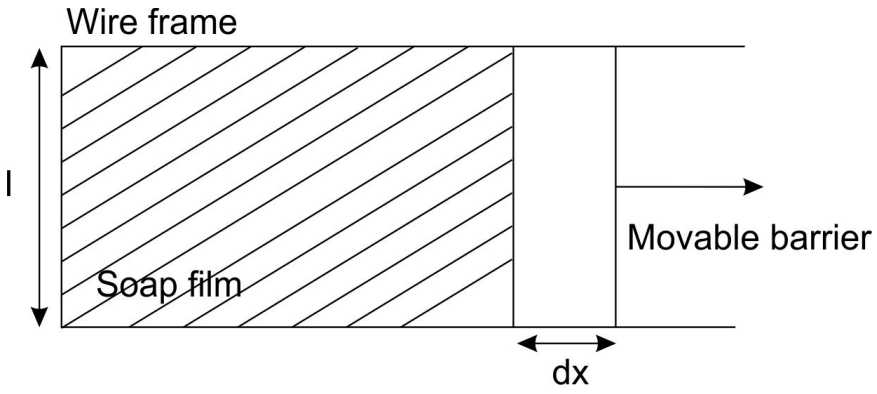

Figure 1.2: A soap film stretched across the wire frame with one movable side.

The molecules experience a strong attractive force between the two like molecules which referred to as a cohesive force. An attraction force between the unlike molecules such as liquid molecule and solid surface is referred as adhesive force. Wetting of the solid surface is governed by balancing between the cohesive and adhesive force. If the cohesive force of the molecules in the liquid is stronger than the adhesive force between the liquid and the surface then liquid does not wet the solid surface (the contact angle $\geq 90^o$), for example mercury on the glass substrate. The complete wetting occurs when the adhesive force is stronger than the cohesive force, and for example water on the glass plate.

1.2.2 Permittivity and refractive index

Permittivity (ε) is a measurement of the ability of the polarizability of material to get polarized by an electric field. It is an important characteristic of a dielectric material. A capacitor capacitance usually depends on permittivity (ε) of dielectric layers and also on the area A of a capacitor and distance d between the conductive plates (explained in the equation below equation). They are mathematically related as

$$C = \frac{\varepsilon A}{d} = \frac{\varepsilon_o \varepsilon_r A}{d} \tag{1.2}$$

Where, ε_r is the relative permittivity, ε_o is the vacuum permittivity, d is the distance between the plates and A is the area of the liquid in between the plates. The dielectric constant (ε_r) is the ratio of permittivity (ε) of material to the permittivity of vacuum (ε_o) that is $\varepsilon_r = (\varepsilon)/\ (\varepsilon_o)$. It is dimensionless number as it is the ratio of two similar quantities [23].

A low-permittivity is nothing but a dielectric which has a low capacity to polarize. They are very good insulators for isolating conductors. On the other hand a high-permittivity are good at holding a charge and usually used as capacitors and also used in memory cells to store data in the form of charge.

Refractive index

Refractive index (n) of a material is defined as a ratio of speed of light in vacuum (c) to the speed of light in the material (v_p).

$$n = \frac{c}{v_p} \tag{1.3}$$

Using the Maxwell's equation, the speed of light in a material has given in terms of the electric permittivity and magnetic permittivity.

$$v_p = \frac{1}{\sqrt{\varepsilon_o \mu_o \varepsilon_r \mu_r}} \tag{1.4}$$

Where ε_r is a relative permittivity of a material, μ_r is a relative permeability, ε_o vacuum permittivity and μ_o is a vacuum permeability.

The speed of a light in vacuum is given,

$$c = \frac{1}{\sqrt{\varepsilon_o \mu_o}} \tag{1.5}$$

Hence, taking the ratio of the two yields,

$$n = \sqrt{\varepsilon_r \mu_r} \tag{1.6}$$

The material is which not magnetic the permeability, μ_r is very close to 1, therefore n is approximately $\sqrt{\varepsilon_r}$.

1.3 Wetting

When a droplet of a liquid dispenses on the solid surface or liquid surface it either wets the surface or contract from the surface and this behaviour is called as wetting behaviour. It depends on the mutual properties of the two non-miscible liquids or liquid and solid [24]. It is versatile in many industrial applications such as

1. Chemical industries for paints and inkjet [5]
2. Soil Science for penetrating liquids into the porous rocks (oil recovery) [7, 8, 25]
3. In the drainage of water from highways [26, 27]

Interfacial tension of the liquid-liquid (γ_{LL}) defines the wetting behaviour of a droplet on an immiscible liquid and this behaviour truly depends on the mutual properties of the liquids. In this case the only difference between interfacial tension and surface tension is the liquid - liquid interface (γ_{LL}) instead of the liquid - vapour interface (γ_{LV}).

The wetting behaviour can be quantified by measuring the contact angle of the drop. Contact angle (θ) is an angle between the direction of the tangent to the solid-liquid and the direction of the tangent to the liquid-vapour.

Thomas Young, a British physicist, explained the behaviour of the wetting depends on the three interfacial tensions and derived the equilibrium contact angle with relation to the three interfacial tensions in 1805 [10]. The three interfacial tensions are influence the shape of the droplet on the solid surface; i.e. liquid-solid interfacial tension (γ_{SL}), solid-vapor interfacial tension (γ_{SV}) and liquid-vapor in-

terfacial tension (γ_{LV}).

As stressed by de-Gennes, Youngs equation is the best way to derive by considering a change in contact line position [15, 28]. Let us consider a small droplet with a constant volume and the diameter $=x_o$ at time t=0 (shown in figure 1.3). The gravitational force is neglected since the droplet is much smaller than the capillary constant. The free energy of the system can be written as:

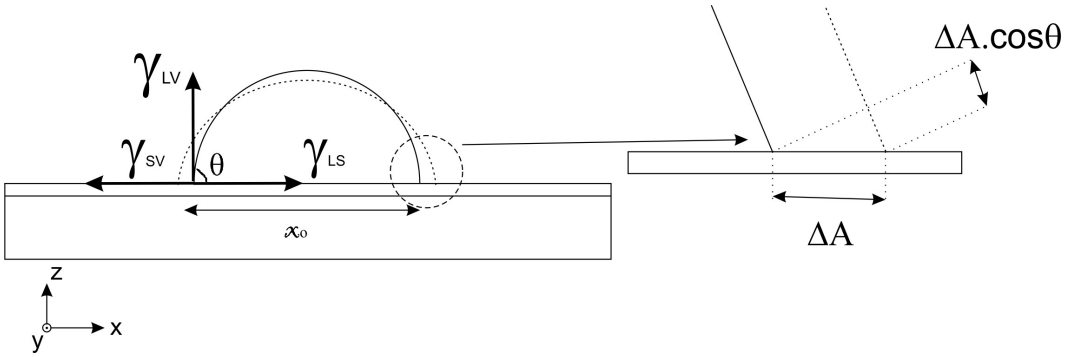

Figure 1.3: Schematic representation droplet shape at t=0 and at equilibrium position. The arrows represents the three interfacial tensions such as solid-vapour interfacial tension γ_{SV}, liquid-vapour interfacial tension γ_{LV} and solid-liquid interfacial tension γ_{SL}. The contact angle of the droplet θ is a angle between the two tangent of the solid-liquid tangent line and liquid-vapour tangent line. Inner picture is an illustration of three phase contact line (dash line) at t=0 and (dotted line) at equilibrium.

$$F = A_{LV}\gamma_{LV} + A_{LS}\gamma_{LS} + \gamma_{SV}(A_\infty - A_{LS}) \tag{1.7}$$

where A_{LV} is an area of liquid-vapor interface, A_{SV} is an area of solid-vapor interface (A_{SV}=A_∞-A_{LV}), A_{LS} is an area of liquid-solid interface and A_∞ is an area of infinite space. The three phase point increased by ΔA area hence the solid-vapour interface is replaced by the solid-liquid interface and in addition the liquid-vapour surface area increased by $\Delta A\cos\theta$ as shown in 1.3.

$$\Delta F = \Delta A cos(\theta_y)\gamma_{LV} + \Delta A(\gamma_{LS} - \gamma_{SV}) + \gamma_{SV}A_\infty \tag{1.8}$$

The surface free energy is minimum at the equilibrium position (ΔF/ΔA=0)

and A_∞ is neglect since the ΔA is much smaller than the A_∞ .

$$cos(\theta_y) = \frac{\gamma_{SV} - \gamma_{LS}}{\gamma_{LV}} \tag{1.9}$$

Where, θ_y is the equilibrium contact angle. This is called Young's equation for equilibrium contact angle [15, 29]. Young's equation is one of the oldest and most used equations in liquid physics.

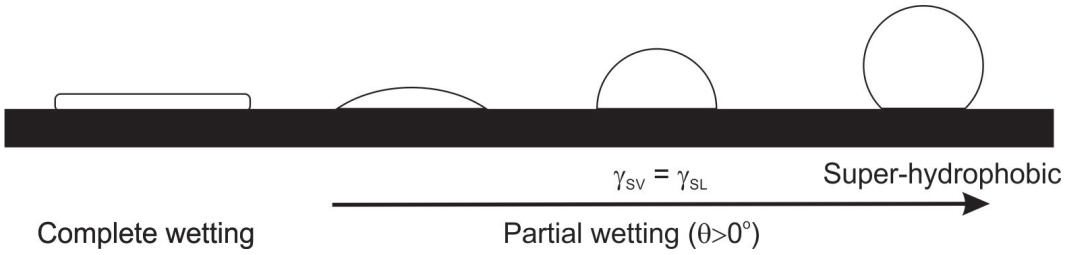

Figure 1.4: illustrates the two wetting states: complete wetting and partial wetting.

Usually the equilibrium spreading coefficient is also used to distinguish the wetting behaviour, and is given by an equation;

$$S_{eq} = \gamma_{SV} - (\gamma_{SL} + \gamma_{LV}) = \gamma_{LV}(cos\theta_y - 1) \tag{1.10}$$

Where, θ_y is the equilibrium contact angle and S_{eq} is equilibrium spreading coefficient.

There are two types of wetting: complete wetting and partial wetting.

Complete wetting: if the interfacial tension of the solid-vapour is equal to the sum of the solid-liquid and liquid-vapour interfacial tensions ($\gamma_{SV} > \gamma_{LV} + \gamma_{SL}$), then at the equilibrium state the liquid completely wets the solid surface and this is called a complete wetting (shown in figure 1.4). For example a water drop on the glass substrate since the glass critical surface tension is high. These kind of materials called as hydrophilic surfaces.

Partial wetting: If the interfacial tension of the solid-vapour is smaller than the sum of the solid-liquid and liquid-vapour interfacial tensions ($\gamma_{SV} < \gamma_{LV} +$

γ_{SL}), then it will perform a partial wetting which means the equilibrium contact angle of the drop should be greater than 0^o as shown in figure 1.4.
When the adhesive force between the liquid molecules and solid surface is much smaller than the cohesive force in the liquid, the liquid wet very small limited area of the solid surface and the contact angle would be more than 150^o. For example, water drop on the super hydrophobic surface (for example micro pillars) [30–32].

1.4 Electrowetting

Wetting can be significantly modified by applying an external electric potential between a liquid drop and solid surface (which should be conductive). In this case, a capacitive system is created in which the charging of the solid-liquid interface induces wetting. Gabriel Lippmann, a French physicist, observed a change in the capillary rise of the mercury in the presence of electric charges. This phenomenon expressed in Lippmanns equation.

$$\gamma = \gamma_o - \frac{1}{2}cV^2 \tag{1.11}$$

Where, γ is resulting surface tension of the solid-liquid interface, γ_o is the surface tension of the solid-liquid interface at no voltage is applied, c is the capacitance per unit area and V is the applied voltage.
The original Lippmanns approach: a small droplet on the metal surface and other metal wire in the liquid. A small potential difference is enough to spread the droplet as shown in the figure 1.5. When an electric potential applied across the liquid and the surface, an potential difference is built at the interface of the liquid and metal surface. The surface tension of the liquid-solid lowers because the repulsion between the like charges in the liquid therefore the three phase contact line moves until to reach an equilibrium position.

In this approach, the modification of the contact angle of the droplet is limited

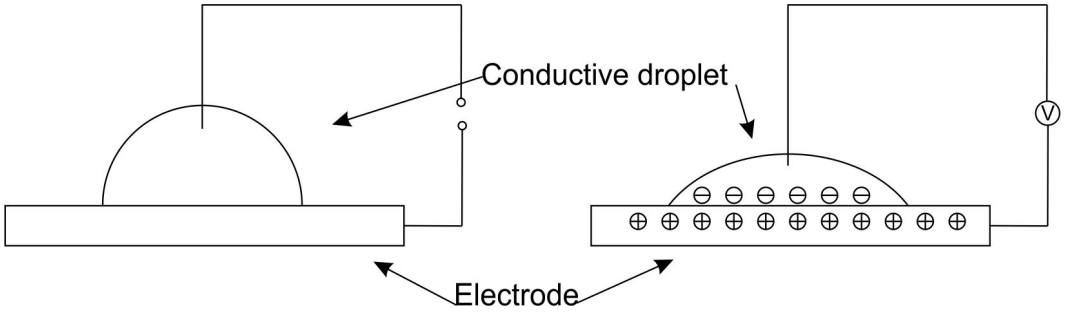

Figure 1.5: A conductive droplet on conductive plate (a) under no voltage and (b) a voltage is applied between the droplet and conductive plate leads the increase in contact area due to the charges in the liquid.

due to the current flow between two electrodes. Therefore an elementary electric field was used in this approach and it can only have an control of 10^o. later, To prevent the current flow, a dielectric layer has introduced between the conductive droplet and conductive plate, and refereed as electrowetting on dielectric (EWOD).

1.5 Electrowetting on dielectric layer (EWOD)

Electrowetting on dielectric (EWOD), is an modified electrowetting, describes a configuration where a dielectric layer (insulating layer) become estranged a conductive liquid and an electrode as shown in figure 1.4. In 1969, Dahms was illustrated electrocapillary response using EWOD and not specifically in the contact angle change [33]. Later in 1993, Berge was reported experimentally that the voltage-induced contact reduction observed on an insulating surface covering conductor [34]. Main advantage of introducing the insulating is to prevent the dielectric breakdown and current flow between droplet and active electrode [9, 10, 35, 36]. Additionally the dielectric layer is treated with the hydrophobic solutions or coated with a very thin layer of hydrophobic layer to increase the contact angle of the droplet. Furthermore, in this practice any kind of liquid can be used.

When a droplet (where the droplet width is less than the capillary length)

is dispensed on the dielectric layer, initially the droplet forms a spherical cap because of the three interfacial tensions on the drop. When a voltage is applied

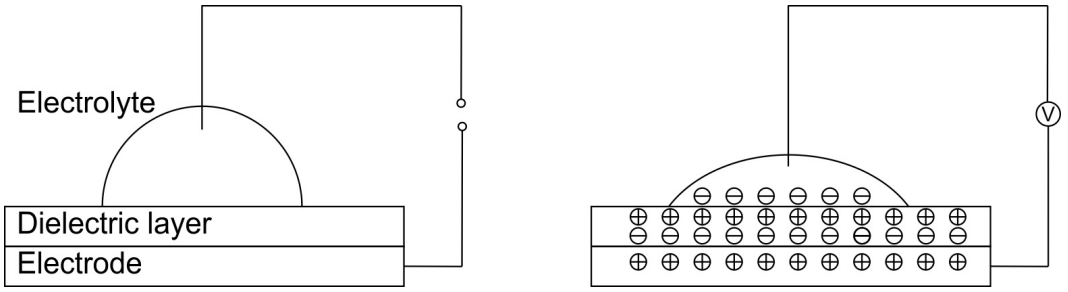

Figure 1.6: schematic illustrations of the liquid wetting of the dielectric layer which is covered on the conductive layer before and after applying voltage.

across the electrode wire and bottom electrode, an electric field induced charge accumulation at the solid-liquid interface and is referred as an electric double layer (EDL). In the presence of the electric field, the interfacial tension of the liquid reduces at the interface of the liquid and the hydrophobic surface, due to the repulsion between the like charges in liquid. Therefore wetting area is increased. The capacitance per unit area is obtained by considering the thickness and dielectric constant of the insulating layer.

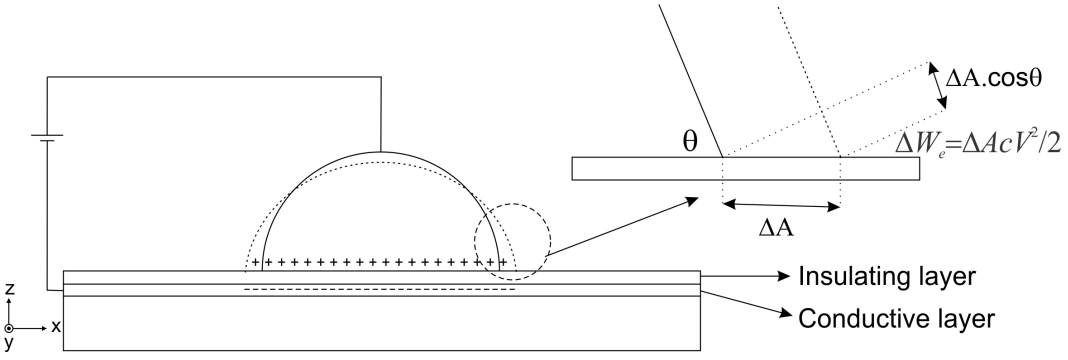

Figure 1.7: Schematic representation of the electrowetting on dielectric (EWOD). Inner picture is an illustration of three phase contact line (dash line) at no voltage, Young's equilibrium, and (dotted line) at equilibrium state of applied voltage.

Due to the capacitive system the three phase contact line is increased by ΔA area hence the solid-vapor interface is replaced by the solid-liquid interface and in addition the liquid-vapor surface area increased by $\Delta A\cos\theta$ as shown in figure 1.5. The strength of the electrowetting effect is controlled by the $-1/2\Delta CV^2$.

Where $\Delta C=\frac{\varepsilon_o \varepsilon_r \Delta A}{d}$, V is the voltage and ΔC is the capacitance per unit area in the region of contact between a metal surface and an electrolyte drop. The change in free energy of the system can be written as:

$$\Delta F = \Delta A cos(\theta)\gamma_{LV} + \Delta A(\gamma_{LS} - \gamma_{SV}) - \frac{\varepsilon_o \varepsilon_r \Delta A V^2}{2d} \tag{1.12}$$

At equilibrium $\frac{\Delta F}{\Delta A}$ is 0.

$$0 = cos(\theta)\gamma_{LV} + \gamma_{LS} - \gamma_{SV} - \frac{\varepsilon_o \varepsilon_r V^2}{2d} \tag{1.13}$$

Therefore,

$$cos(\theta) = \frac{\gamma_{SV} - \gamma_{LS}}{\gamma_{LV}} + \frac{\varepsilon_o \varepsilon_r V^2}{2d\gamma_{LV}} \tag{1.14}$$

Since $cos(\theta_y) = \frac{\gamma_{SV} - \gamma_{LS}}{\gamma_{LV}}$,

$$cos(\theta) = \cos(\theta_y) + \frac{\varepsilon_o \varepsilon_r V^2}{2d\gamma_{LV}} \tag{1.15}$$

Equation 1.15 is called Youngs-Lipmann equation. The equilibrium contact angle (θ) of the droplet induced by voltage depends on the applied voltage and liquid properties such as permittivity and surface tension. The cosine of the contact angle depends on the square of the applied voltage [37].

The EWOD phenomena is important for wide range of applications such as: microfluidics [6], digitally controlled droplet-based chemical reactions, biological assays [38, 39], liquid based optics [34, 40, 41], control of the mixing of two or more liquids, dispensing of liquid, and droplet motion [42] in microfluidics.

1.6 Dielectrophoresis

Dielectrophoresis is defined as the translational motion of a neutral matter caused by polarization effects in a non-uniform electric field [43–46]. Dielectrophoresis phenomenon is unlike electrophoresis, and it requires an uncharged particle to

move or translate. Pellat noticed the dielectrophoresis in his experiment in which a dielectric liquid raised between the two parallel electrodes when voltage was applied between the electrodes [47].

Dielectrophoresis force on polarisable particle: Figure 1.8 shows the difference between the dielectrophoresis and electrophoresis, and also shows the behaviour of a charged particle and neutral particle in uniform (a) and non-uniform (b and c) electric field. In either uniform or non-uniform electric field a charged particle always moves along the field lines towards the electrode of opposite polarity unlike a neutral particle. A neutral particle is first polarized by the presence of the electric field, which induces a dipole moment such that a negative charge appears near the positive electrode and a positive charge appears near the negative electrode (in other words separation of charges on neutral particle creates a dipole) as shown in figure 1.8.a. A dipole in a uniform electric field does not experience a force but experience a torque.

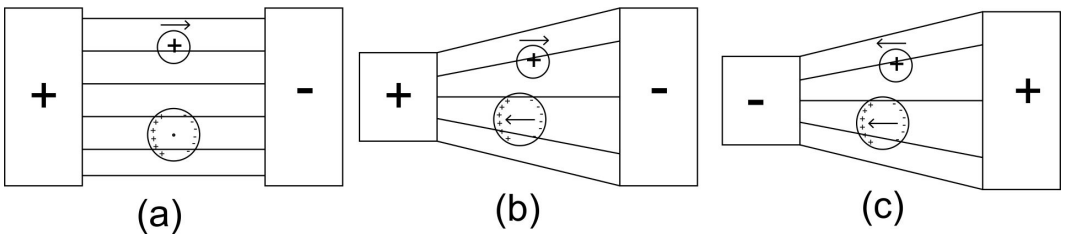

Figure 1.8: (a) Charged and neutral particles in a uniform electric field. The charged particle on the top is moved toward opposite charge, whereas the dipole induced in the uncharged particle will not result in a net force (b) and (c) the neutral particle is attracted towards the region of highest electric field gradient in non-uniform electric field.

In non-uniform electric field, a charged particle moves along the electric field towards the opposite polarity electrode. The neutral particle experience a bulk force towards the high field gradient because the force on the particle is unequal and result of the rise in net force on the particle, as shown in figure 1.8. b and c. The polarization of the neutral particle in the non-uniform electric field is bringing the force on the particle to move towards the strong electric field. The

neutral particle moves towards the high electric field gradient even the polarity of the electric field switched as shown in the figure 1.8. Dielectrophoresis force is given below equation [48, 49].

$$F_{DEP} = \frac{1}{2}\varepsilon_o(\varepsilon_r - 1)\bigtriangledown \mid E \mid^2 \tag{1.16}$$

Equation 1.16 gives the three important results:

1. The dielectrophoretic force is proportional to the square of the gradient of the electric field and the medium is drawn towards the high field gradient.

2. This is independent to polarity of the field.

3. The force is also depends on the dielectric constant of the medium. A larger dielectric constant will give a lager force for the same electric field.

DEP phenomenon has shown the versatile applications including Microfludics, Lab on a chip, camera lenses and etc [12, 13, 50–60]. Dielectrophoresis can be operated either in a droplet based manner or flow through manner [50].

Droplet based manner : For biological applications, a droplet containing the target particles is injected onto the DEP platform.

Flow through manner: A steam of medium containing the target particles is flow through the micro channels which is attached with DEP platform and this approach is mainly used in Lab-on a chip (PCR analysis, DNA analyser and some other biology applications [50–52]).

In either of the manner, DEP force should be high enough to overcome the forces including gravity, surface-adhesive force, hydrodynamic and intra-particle force. For optical applications, the droplet is injected on the DEP platform where the contact angle of the droplet is controlled by DEP force. The system response depends on the applied voltage, liquid properties including dielectric constant, surface tension and viscosity.

The industrial applications:

- Transportation, mixing, concentration, separation [55–59] and characterization of the biological sample such as cells, bacteria, DNA, protein and viruses [50–54].
- Separation and manipulation of the rare earth oxide particles [60].
- Variable focus lens and a micro lens array [12, 13].

1.7 Liquid-Dielectrophoresis

Originally Pohl defined DEP as the translation motion of a neutral particle caused by polarisation effects in a nonuniform electric field. Liquid dielectrophoresis (LDEP) is an electromechanical phenomenon; describes the motion of polar liquids which induced by nonuniform electric fields. In LDEP, liquid actuation is not concerned with particles inside the liquid; relatively it exploits the force to manipulate liquid masses. Phenomenological it is related to particulate DEP in that polarizable liquids also are drawn into regions of stronger electric field intensity, but additionally the shape of the liquid will be appeared as the electric field.

Initially this phenomenon was demonstrated by Pallet's in 1895, shown in figure 1.9. Pellat's experimental set-up is contained of a pair of parallel electrode plates are oriented vertically and separated by a gap s [1]. The electrodes partially immersed in a reservoir of dielectric liquid. By applying a voltage across the electrodes, due to the nonuniform electric field the dielectric liquid between the electrodes rises vertically upwards to the new equilibrium height h_u given by equation 1.17. This is called **dielectric height-of-rise**. Instead, like capillarity, it creates new hydrostatic equilibrium, which may be exploited to contain liquids in "wall-less" flow structures. The nonuniform electric field provides this containment; much like gravity holds water in a ditch or the capillary force confines kerosene in a lamp wick.

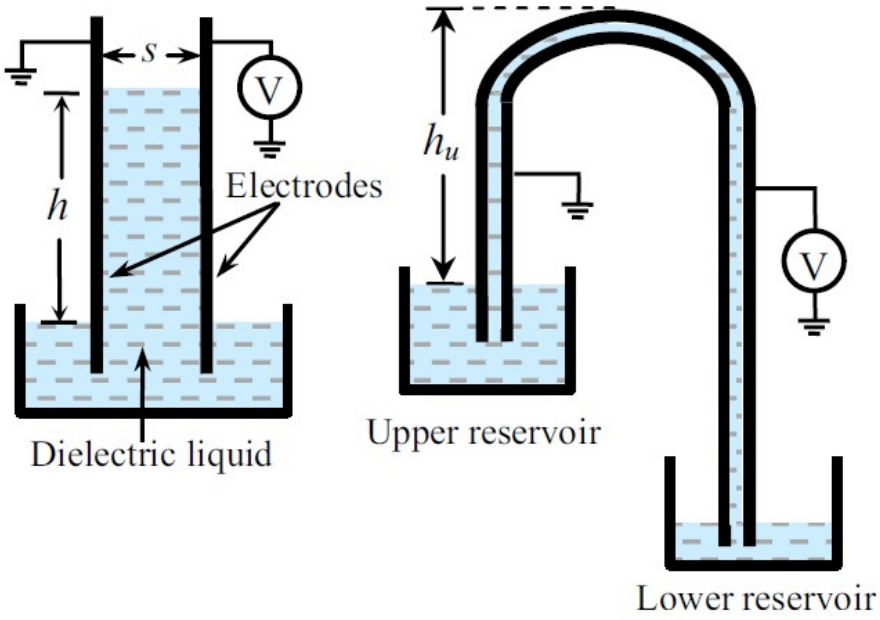

Figure 1.9: Dielectrophoresis of insulating dielectric liquids. (a) Pellat's original experiment [1]. (b) The dielectric siphon experiment [2–4].

$$h_u = \frac{(\varepsilon_r - \varepsilon_o)V^2}{2s^2\rho g} \tag{1.17}$$

Whereas ρ is density of the dielectric liquid, ε_r is the permittivity of the liquid, g is acceleration due to gravity, ε_o is the permittivity of free space and V is the applied voltage.

In 1971, Jones et al developed a dielectric siphon, modified Pallet's experiment, consisting of two reservoirs connected through a pair of electrodes. An upper reservoir filled with dielectric liquid and lower initially empty reservoir [2]. By applying a sufficient voltage ($V \geq V_{min}$) between the electrodes, due to the nonuniform electric field the dielectric liquid between the electrodes rises vertically upwards to the height h_u (the highest point of the siphon). At this point the hydrostatic pressure difference between the two reservoirs establishes and sustains the liquid flow between the two reservoirs.

$$V_{min} = \sqrt{\frac{2s^2\rho g h_u}{(\varepsilon_r - \varepsilon_o)^2}} \tag{1.18}$$

Later L-DEP is extended with the highly pure water replaced the dielectric liquid [11]. The main challenge to activate the water droplet motion using L-DEP is to overcome the electrolysis and joule heating. A dielectric layer, insulating layer, is coated on the electrode geometry to avoid the electrolysis similar to the electrowetting on dielectric (EWOD). Joule heat is generated when a strong electric field is applied to the water droplet to activate the liquid motion. The heat is dissipated through the contact area of the drop to the substrate. Therefore, the smaller electrode array and a smaller water droplet will be reducing the joule heat effect. T B Jones, in his research, has shown the water droplet actuation on the electrode array without joule heat effect or electrolysis [3, 11].

Basic principle of the LDEP

The basic principle of the LDEP is illustrated in figure 1.10 and consists of two parallel conductive plates divided by distance s. The electric field between the conductive plates will induce dipole moment in dielectric material. Negative charges appear on surface near positive plate, positive charges appear on surface near to negative plate. An attractive force at the advancing edge of the liquid in capacitor pulls the dielectric material in to the capacitor.

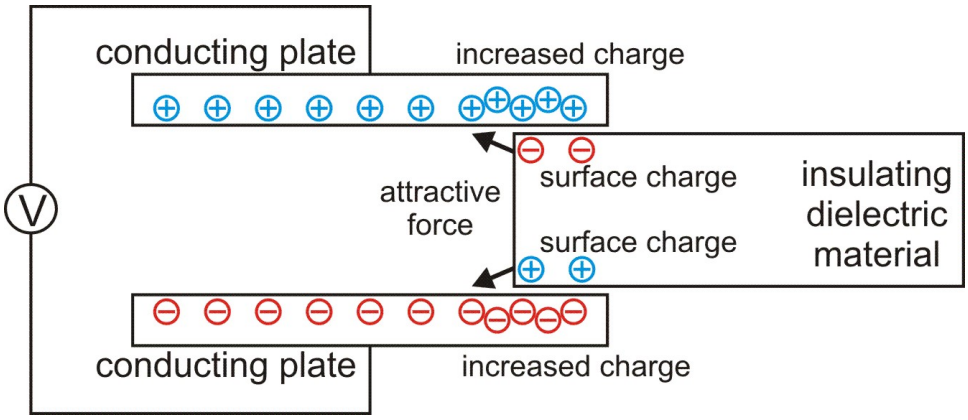

Figure 1.10: schematic illustration of the basic principle of the liquid dielectrophpresis (LDEP). A dielectric liquid is pull between the two conducting plates due to the attractive force.

In our configuration, interdigitated electrode array having equal line gaps and

widths, a multi-plate capacitor consists of number of parallel plates arranged as shown in figure. When a voltage was applied to each alternative electrode finger with the interposed electrodes at earth potential in an interdigitated array of electrodes, the attractive force at edge of the dielectric liquid pulls the dielectric liquid along the electrodes. Therefore the contact angle of the droplet will be reduced as the voltage increased and the droplet will be consisted to move along the electrodes (no cross spreading).

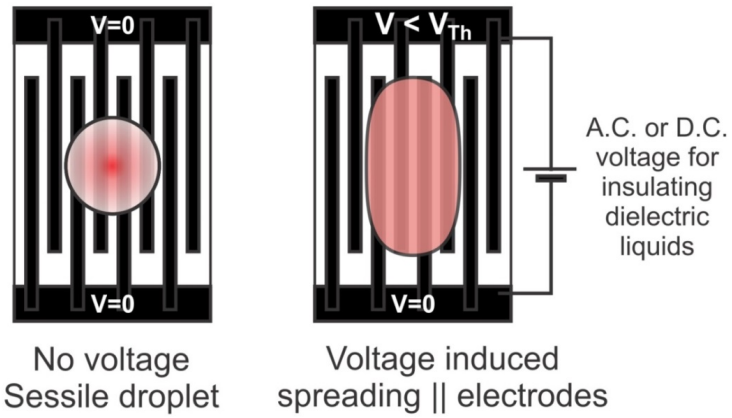

Figure 1.11: (a) shows that top view of the droplet resting on an interdigitated electrode array with equal line gaps and widths (b) shows the droplet spreading along the interdigitated electrodes when the voltage was applied.

Feasible applications using LDEP:

The practically feasible applications of L-DEP necessitate that the dominating effect of macrolevel forces such as gravity and viscosity be subdued, and actuation voltages reduced to more nominal values. In 2001, Jones et al was achieved the liquid actuation by implementing L-DEP at a microscale [11]. Chin-Cheng Chan has shown the fabrication of the variable focus liquid lenses using the L-DEP [12], and similarly Yu-Chi Wang has shown the fabrication of the lens array with a programmable focus gradient using the L-DEP [13]. The Carl Brown group has demonstrated a novel optical effect in which a wrinkle is induced at an oil/air interface by applying a periodic potential profile in the plane of the interface [17, 18].

1.8 Diffraction Gratings

A diffraction grating is a collection or series of diffracting element such as apertures (a pattern of transparent slits) or a collection of obstacles (grooves) which have the effect of periodically altering either the amplitude or the phase. These kind of structures allows the light to diffract in to several beams, diffraction orders, in different directions [61]. The directions of the diffraction spots depend on the spacing between the slits or grooves and the wavelength of the light [61].

Grating have been used in optical applications for example tunable gratings are able to redirect, focus or modulate the light which are controlled by user input signal [62]. Similar kind of devices are developed include liquid crystal gratings [63–67], blazed grating [68] which are made from micro pillars and liquid phase grating where the pitch are controlled by the external sources. The phase gratings created by tuneably buckling gold coated elastometric surfaces or silicon sheet polymer [69, 70],

The amplitude of the passing wave front has an effect by introducing a set of transparent and opaque regions in the diffraction grating and this type grating referred as amplitude grating. If the grating consists of an array of stripes with varying optical thickness or a series of two materials then a modulation in the phase of the passing wave front occurs. This kind of gratings referred as a phase grating.

1.8.1 Amplitude Grating

Figure 1.12 is an amplitude grating which consists of a series of transparent slits. When a plane waves are incident on an array of slits, the light is diffracted into several diffracted beams. The amplitude grating equation is given in equation.

$$b.sin(\theta_q) = n\lambda \tag{1.19}$$

Where b is the distance from center to center between the slits, θ_q is the diffraction angle, λ is the incident light wavelength and n is the diffraction order.

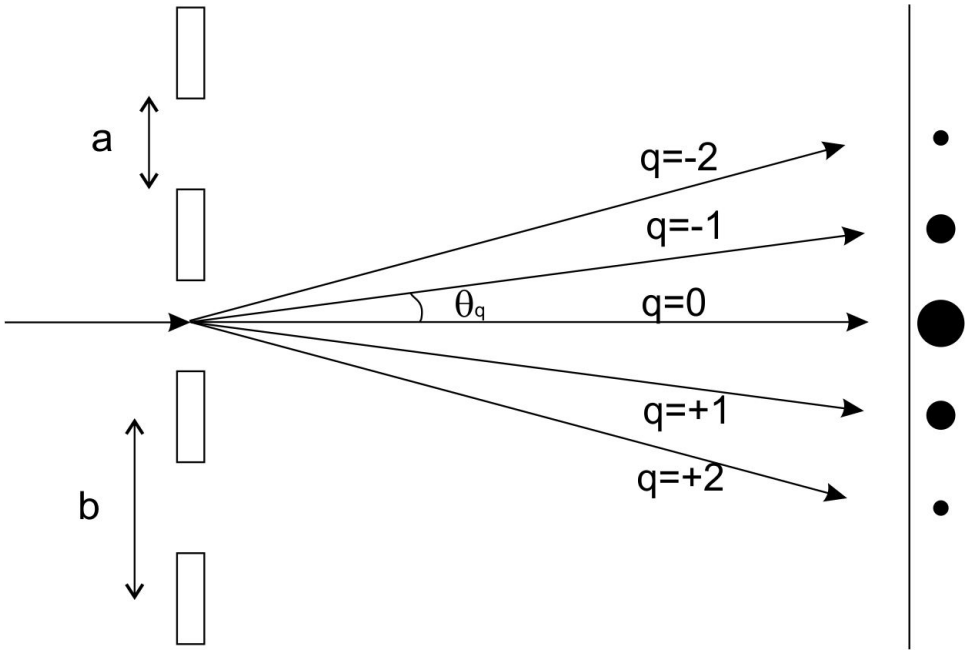

Figure 1.12: schematic picture of the amplitude grating with N slits, and width of the slit is a, width of center to center of the slit is b.

The equation of the amplitude grating (equation 1.20) having N identical slits, where a center to center spacing b and a slit width is a, gives the information about the intensities of the diffraction spots.

$$I(\theta_q) = \frac{I(0)}{N^2}\left(\frac{sin(\beta)}{\beta}\right)^2\left(\frac{sin(N\alpha)}{\alpha}\right)^2 \tag{1.20}$$

Where $I(\theta_q)$ is the intensity at angle θ, I(0) is the incident light intensity, $\alpha = \frac{ka}{2}sin\theta_q$, $\beta = \frac{kb}{2}sin\theta_q$ and $k = \frac{2\pi}{\lambda}$ is the wave vector.

1.8.2 Phase Grating

A conventional phase grating consists of two transparent materials which have different refractive indices as shown in figure 1.13.a. When a light is illuminated in transmission through one of the material and this ray will experience a phase retardation which depends on the thickness, the refractive index of the material

and the wavelength of the light. The phase retardation at normal incidence is given in the equation 1.21 for a particular material.

$$\delta\phi = \frac{2\pi t n_1}{\lambda} \tag{1.21}$$

Where λ is the wavelength of the light, t is the thickness of the grating and n_1 is the refractive index of the material M1.

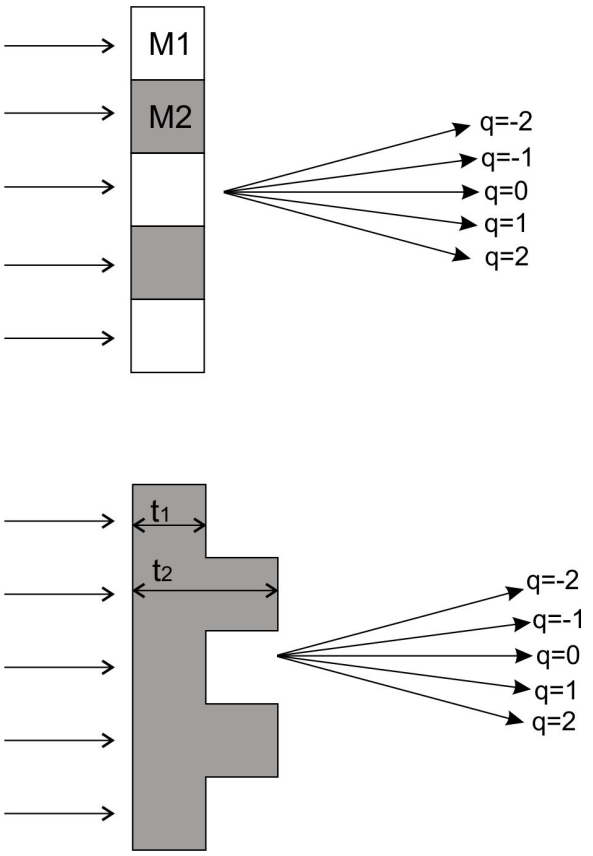

Figure 1.13: Schematic illustration of the two different phase gratings: (a) a phase grating with two different materials of different refractive index, (b) a phase grating of a one material with a periodic variation of thickness.

When a ray travelling through the M2, if M2 has a different refractive index than the M1, it will have a different phase retardation to that of the light passing through M1. Due to the difference in phase retardation it leads to a diffraction pattern in the far field. This phase difference is given by the below equation.

$$\delta\phi = \frac{2\pi t(n_1 - n_2)}{\lambda} \tag{1.22}$$

The incident light is diffracted into the higher orders and the diffraction angle, an angle between zero order to other diffraction orders, depends on the material properties and periodic variation.

There is an alternative phase grating which have a singular refractive index but with a periodically varying the thickness of the substrate as shown in figure 1.13.b.

$$\delta\phi = \frac{2\pi n(t_1 - t_2)}{\lambda} \tag{1.23}$$

The phase difference between a ray travelling through peak and trough or region of different thickness leads to a diffraction pattern and the destructive interference occurs between the light rays when the phase difference is 2π radians. The diffraction angles and intensities of the diffraction spots depend on the periodicity and thickness variation.

1.8.3 Thin sinusoidal phase grating

Thin sinusoidal phase grating is a grating where the thickness of the material varies periodically (like waves). Surface ripple is created at the interface of the material and air by an external force such as mechanical and thermal agitation. For example, a polymer is filled between two parallel electrodes and then a voltage is applied across the electrodes. A normal electric field creates electrohydrodynamic instabilities at the interface between a polymer film and an air layer within the capacitor which evolve to give regular self-organized structures[19–21]. Other example, our approach, micrometer sinusoidal structures are produced by using a set of co-planar stripe interdigital electrodes to create a non-uniform A.C. electric field that exponentially decays in amplitude and penetrates above the structure into a dielectric liquid droplet [17, 18].

When a light is illuminated in transmission through these kinds of gratings, the light is diffracted into multiple spots due to the sinusoidal variation in the

thickness of the material which would lead to a sinusoidal variation in the optical path length of the light. The amplitude grating equation is rewritten as the diffraction angle equation where the spacing between the slits is replaced with the pitch of the sinusoidal surface profile Λ i.e.

$$\Lambda sin\theta_q = n\lambda \tag{1.24}$$

The intensities of the diffraction spots depend on the peak to peak amplitude of the wrinkles or optical path length between the peaks and troughs of the wrinkles.

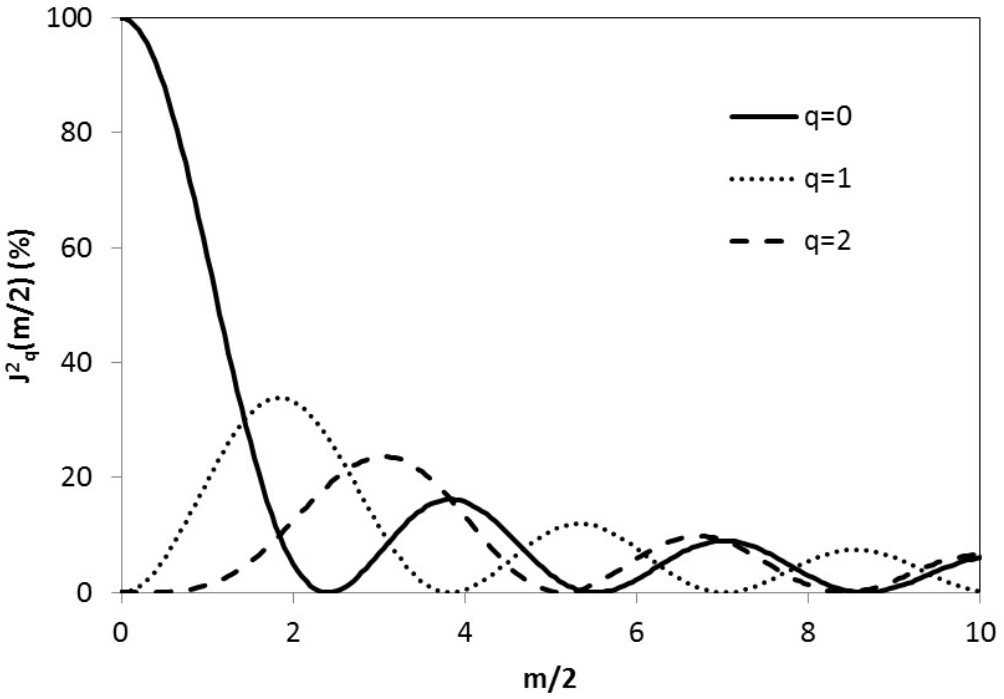

Figure 1.14: Diffraction efficiency of the 0th, 1st and 2nd of the diffraction pattern as a function of phase delay (m).

In this grating, the zero order energy diffracted into a multiple higher order and no power is observed in this grating. Therefore the sum of the intensities of the all orders remains constant and also equal to the incident light intensity. The intensity patterns, η_q vs m/2, of the thin sinusoidal phase grating is given in the

figure 1.14. The diffraction efficiency of the q^{th} order is given in equation.

$$\eta_q = J_q^2(m/2) \tag{1.25}$$

Where the parameter m represents the peak-to-peak excursion of the phase delay.

The maximum diffraction efficiency is diffracted into the -1 and +1 order spots. The maximum intensity of the first order is 33.8% of the actual incident light intensity as shown in figure 1.14 which is far greater than for the case of amplitude gratings [71].

Chapter 2

Experimental techniques

2.1 Introduction

This research work focuses on the wetting, dewetting and creating wrinkles at the air/liquid interface of a liquid drop using dielectrophoresis on interdigitated electrodes (IDT).These forces occur as a result of the polarisation of the liquid in the highly non uniform electric fields created by the co-planar interdigitated electrodes on which the droplet rests. This chapter describes the experimental methods and techniques including IDT fabrication process which includes chemical etching and gold deposition. Surface treatment of the dielectric layer is also discussed according to the experimental requirement. Experimental setups are also discussed here including interferometer, drop shape analysis, stylus profilometer and optical diffraction measurement.

2.2 Device Fabrication

2.2.1 Electrode Geometry

The Interdigitated electrode array area of 5mm×5mm was transferred to the pre coated indium tin oxide layer (ITO) having thickness of 25nm on the borosilicate glass using standard photo lithography. The co-planar interdigital fingers in xy and xz direction are shown in figure 2.1. The electrode width is equal to the space between the electrodes for all of the devices studied in this thesis apart from the radial electrode geometry. The black area in the figure represents the electrodes and the white area is the gap between the electrodes.

A 10 kHz square wave voltage was applied to the each alternative electrode finger with the interposed electrodes at earth potential to create a highly non-uniform electric field. The AC voltage was provided by a TTi TGA1244 arbitrary waveform generator (Thurlby Thandar Instruments Limited, Cambs, UK) with each Signal being amplified 100 times by a PDZ350 amplifier (Trek Inc., Medina, New York, USA). An oscilloscope (DSO6014A, Agilent Technologies) and a multi

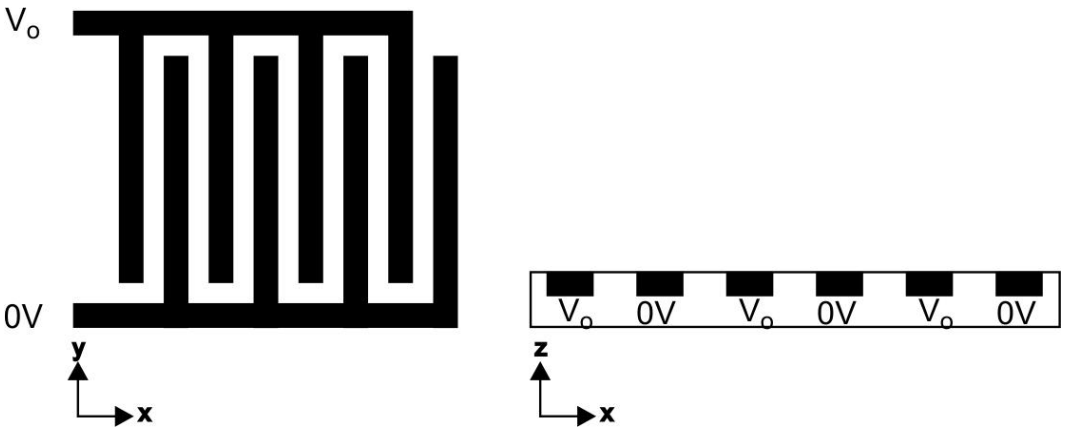

Figure 2.1: Schematic picture of the interdigitated electrodes from top view (x-y axis) and side view (x-z axis).

meter were connected in the circuit to monitor the wave form and V_{rms} voltage.

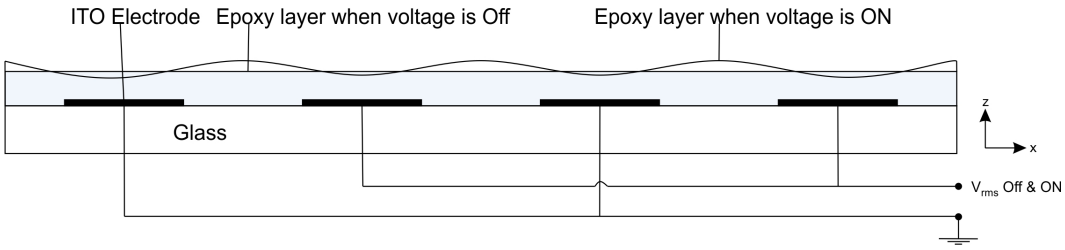

Figure 2.2: Schematic illustration of wrinkle formation at epoxy/air interface.

A 10 kHz square wave voltage was applied to each alternative electrode fringes in the coplanar strip electrode array and interposed electrodes were earthed hence a non-uniform electric field was created. In this non-uniform electric field a dielectric material, UV curable epoxy, experiences a dielectrophoretic force in the direction of high magnitude of electric field gradient. The electric field gradient is high in between the electrodes so the dielectrophoretic forces in these regions cause the oil to collect there preferentially, and in turn liquid from the region above of the electrodes are removed as shown in figure 2.2.

To characterize the dynamic effect of the wrinkle (discussed in chapter 4), the square wave signal was modulated with either a low frequency square or triangular wave signal. The modulation was created by the internal inter-channel modulation function of the waveform generator. In triangular modulation, the amplitude was linearly increased and decreased from minimum voltage to maxi-

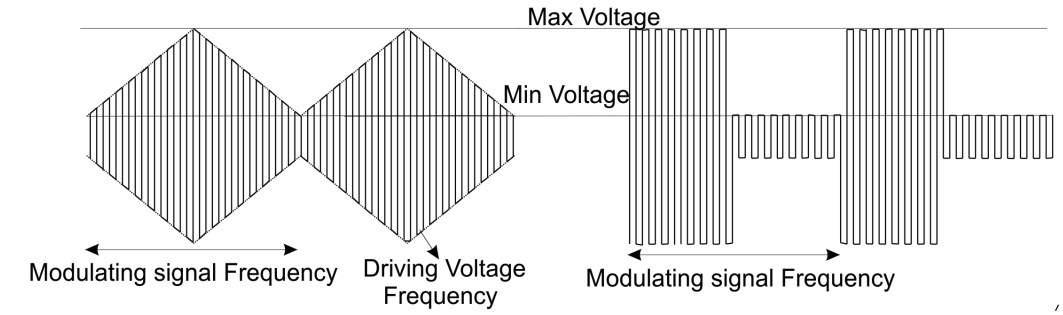

Figure 2.3: Schematic diagram of the square signal was modulated with either a lower frequency triangular wave (giving a periodic voltage ramp) or a lower frequency square wave.

mum voltage (shown in figure 2.3a). The triangular modulation used to monitor the monotonically increased and decreased of the wrinkle amplitude. In square wave modulation, the voltage was increased and decreased from the minimum voltage to the maximum voltage (shown in figure 2.3b). The square modulation was used to monitor the rising and falling of the wrinkles.

2.2.2 ITO Etching Process

Pre coated ITO (Indium Tin Oxide) glass slides (100Ω/square) were used to fabricate the interdigitated electrode array. The fabrication process involves six steps; cleaning process, spinning process, UV exposing process, developing the S1813 process, ITO etching process and removing the S1813 process (shown in figure 2.4)[49, 72].

Initially ITO pre-coated borosilicate slides were cut into 25mm X 25mm size.

Cleaning process (Step 1): Substrates were cleaned in an ultrasonic bath with 5% of Decon 90 (Decon Laboraties Limited, Sussex, UK) in deionised water warmed to 90^{o}C to remove any contaminations and dust particles. These samples were then transferred to another beaker with 0.5% of decon 90 in deionised water warmed to 90^{o}C to remove the detergent on the samples and followed by cleaning in ultrasonic bath with deionised water warmed to 90^{o}C. These samples were rinsed in Isopropyl alcohol (IPA) warmed at 45^{o}C and followed by drying with

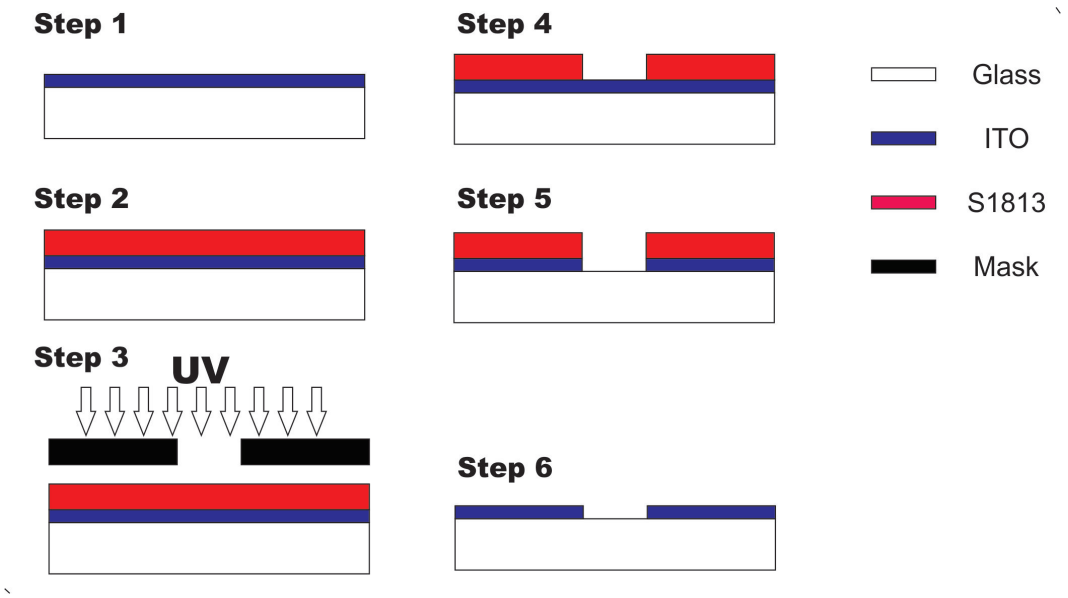

Figure 2.4: Schematic diagram of the photolithography procedure in step by step process. Step 1: Cleaning the ITO slides, Step 2: Photo resist layer coating, Step 3: UV light exposure through photo mask, Step 4: Photo resist development, Step 5: Developed pattern etching and Step 6: Removable of photo resist

N_2.

Spinning process (Step 2): a positive photo resist (S1813) was spin coated on the cleaned ITO slides using a Laurell WS-6505-6NPP spin coater. S1813 was filtered by using the 2μm filters and was dispensed on the ITO slide. The thickness of the S1813 layer depends on the spinning speed and duration. To achieve the required S1813 thickness, spinning process is done in two steps: the first was for 10sec at 500rpm to remove any excess of photoresist and the second was for 30sec at 3000rpm to get uniform thickness of the S1813. The samples were then baked at 105^{o}C for 75 Sec to remove the solvent in S1813. The thickness of the S1813 was obtained 1.4μm.

UV exposing process (Step 3): Using a Microtec SUSS MJ4B Mask aligner, the samples were exposed with UV light through a positive mask (chrome on glass photolithography mask), containing an interdigitated electrode pattern, for 1.4 Sec.

Developing the S1813 process (Step 4): The exposed area was removed by developing where the sample was immersed in 50-50 water-microposit devel-

oper solution for 15 seconds to reveal the pattern in the photo resist and the electrodes. To make the S1813 layer robust and resistant to chemical attack, the samples were then baked at 105^{o}C for 10min.

ITO etching process (Step 5): To etch the ITO the samples were then immersed for 8 minutes in a solution prepared with 1% of nitric acid, 12.5% of hydrochloric acid and 12.5% of deionised water. Samples were then rinsed with deionised water to stop etching.

Excess the S1813 process (Step 6):S1813 was removed by rinsing with acetone for a few seconds. Samples were rinsed with IPA followed by the dry nitrogen to remove the solvent.

2.2.3 Gold Lift-Off Process

The gold deposition method was also used to fabricate the electrodes to reduce the electrode thickness and increase the conductivity compared to the ITO electrodes. The electrodes were fabricated in six steps; cleaning, spinning, exposing UV, S1813 development, titanium and gold deposition, removing the S1813 as shown in figure2.5 [73].

Cleaning process (Step 1): The microscopic glass slides were cleaned in an ultrasonic bath with 5% of Decon 90 in deionised water warmed to 90^{o}C to remove any contaminations and dust particles. These samples were then transferred to another baker with 0.5% of decon 90 in deionised water warmed to 90^{o}C to remove the detergent on the samplesr and followed by cleaning in ultrasonic bath with deionised water warmed to 90^o. These samples were rinsed in IsoPropyl Alcohol (IPA) warmed at 45^{o}C and followed by drying with N_2. To increase the adhesiveness between the S1813 and glass substrates, The microscopic glass slides were immersed in 2% volume proportion Hexamethyldisilazane, HMDS (Sigma-Aldrich, UK) and toluene (Sigma-Aldrich, UK) overnight. These samples were rinsed with IsoPropyl Alcohol (IPA) and followed by blow drying with N_2.

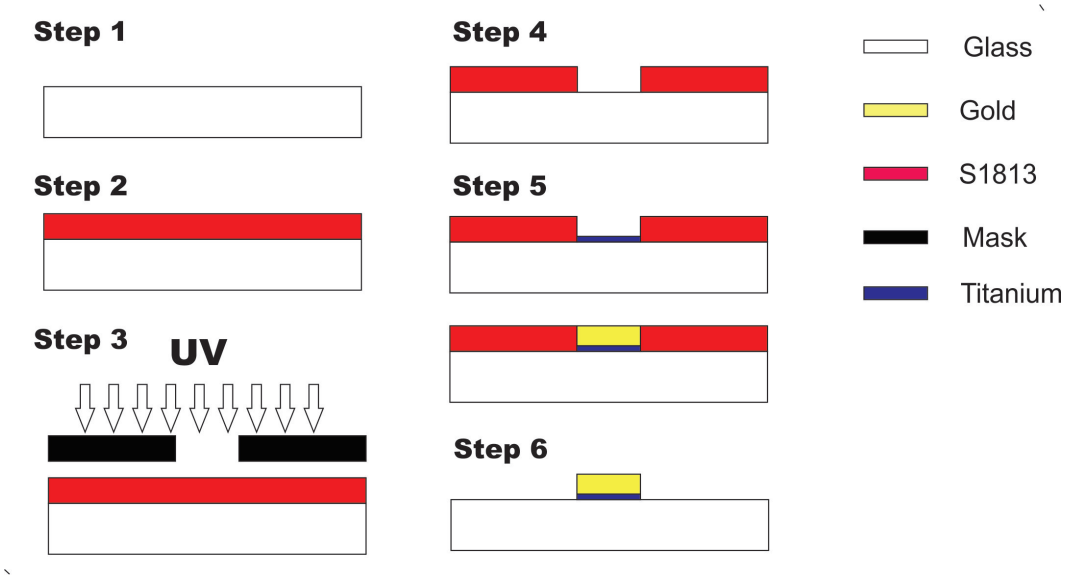

Figure 2.5: Schematic diagram of the gold lift off procedure. Step 1: Cleaning the ITO slides, Step 2: Photo resist layer coating, Step 3: UV light exposure through photo mask, Step 4: Photo resist development, Step 5: Gold deposition and Step 6: Removable of photo resist

Spinning process (Step 2): a positive photo resist (S1813) was spin coated on the cleaned glass slides using a Laurell WS-6505-6NPP spin coater. S1813 filtered by using the 2μm filters and dispensed on the glass slides. The Thickness of S1813 depends on the spinning speed and duration. To achieve the required S1813 thickness, spinning of the S1813 on the ITO slides were done at two different durations and at two different speeds: the first was for 10sec at 500rpm to remove any excess of photoresist and the second was for 30sec at 3000rpm to get uniform thickness of the S1813. The samples were then baked at 105^{o}C for 75 Sec to remove the solvent in S1813.

UV exposing process (Step 3): by using Microtec SUSS MJ4B Mask aligner, the samples were exposed with UV light through a negative mask which have the interdigitated electrode pattern for 1.4 Sec.

Developing the S1813 process (Step 4): samples were developed in 50-50 water-microposit developer solution to reveal the pattern in the photoresist and the exposed part of the S1813 removed. To make the S1813 harder, these samples were backed at 105^{o}C for 10min.

Titanium and gold deposition (Step 5): the samples were sputter coated with TiO_2 for 24sec and Au for 15sec using the sputter coater (EMITECH sputter coater, K575X,quorum technologies).

Removing the S1813 process (Step 6):S1813 was removed by using the acetone. Samples were rinsed in IPA followed by the dry nitrogen to remove the solvent.

2.2.4 Dielectric Layer fabrication

A Dielectric layer (SU8 layer) was deposited on electrodes to avoid the contact between a liquid droplet and electrode to reduce the chance of electrostatic breakdown and because some of the dielectric liquid had a residual conductivity. The fabrication of the dielectric layer procedure divided into five steps; cleaning process, spinning SU8, soft baking, UV exposing to polymerise and post baking as shown in figure 2.6.

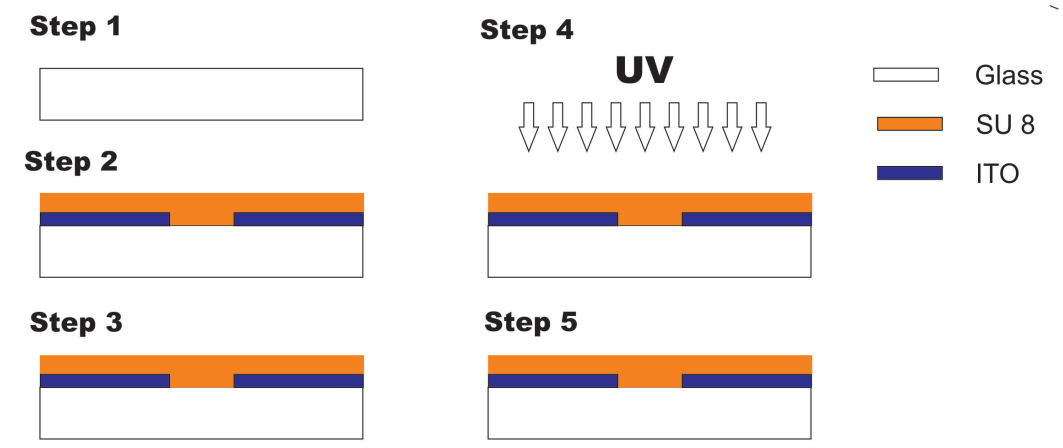

Figure 2.6: Schematic diagram of the dielectric layer deposition procedure. Step 1: Cleaning the glass slides, Step 2: SU8 layer coating, Step 3: Soft backing, Step 4: UV light exposing and Step 5: Hard baking.

The cleaning process is same as described in section 2.2.1.

Spinning SU8 process (Step 2): 50:50 by volume proportion of SU 8 10 (negative photo resist) and microdev solvent was spin coated on the electrodes in Laurell WS-6505-6NPP spin coater. To achieve the required S1813 thickness,

spinning of the S1813 on the ITO slides were done at two different durations and at two different speeds: the first was for 10sec at 500rpm to remove any excess of photoresist and the second was for 30sec at 3000rpm to get uniform thickness of the SU8. Thickness of the SU8 was measured using the stylus profilometer (Dektak 6M, Veeco, NY USA) and was 2μm.

Soft baking (Step 3): samples were baked at 65^{o}C for 1min followed by at 95^{o}C for 1min to remove the solvent in the SU8 and solidfy the film.

UV exposing to cross link (Step 4): samples were flood exposed with UV light for 6sec in Microtec SUSS MJ4B Mask Aligner to make them hard and resistant to chemical attack.

Hard Baking (Step 5): The samples were baked at 65^{o}C for 1min, 95^{o}C for 3min and 155^{o}C for 10min. The samples were left on the hot plate whilst it cools down.

2.2.5 Surface Treatment

The contact angle of the drop of the 1, 2 propylene glycol on an untreated SU 8 layer was below 30^o as shown in figure 2.7. In order to increase the contact angle of the droplet on the SU 8 layer surface, the SU8 layer was treated with a solution, called Granger solution, which was designed for waterproofing breathable fabric (Granger's extreme Wash-in, Grangers International Ltd, Alfreton, UK). Granger solution consists of fluorocarbon emulsified in water with a detergent [74].

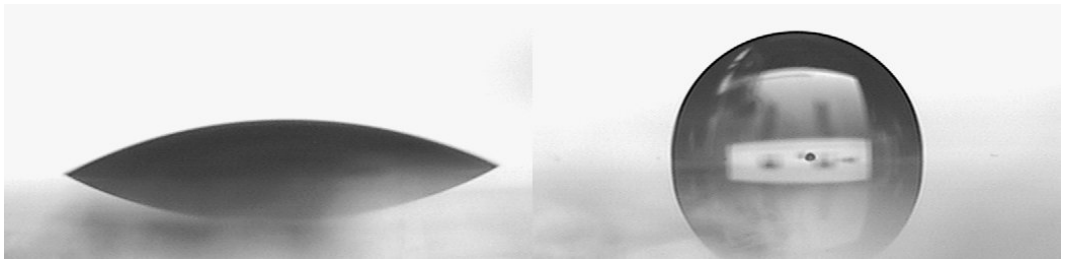

Figure 2.7: shows a sessile drop of the 1, 2 propylene glycol on SU8 layer (a) before and (b) after treatment with granger solution.

To increase the surface energy of the SU 8 layer, the SU8 samples were oxi-

dized in UV/Ozone ProCleaner (Bioforce nanoscience, USA) for 20min and then immersed in the deionised water and Granger solution having concentration of 20:1 for 20min; the sample was then rinsed using deionised water followed by blow drying using dry nitrogen. The samples were then baked at 80^{o}C for 20min on a hot plate. The contact angle of the 1, 2propylene glycol drop was increased from 30^o to 90^o as illustrated in figure 2.7.

2.3 Stylus Profilometer

Stylus contact profilometer (Dektak 6M, Veeco, NY USA) was used to get the 2D profile of the solid surface on a micro scale and to measure the amplitude of the surface wrinkle in solid state. The working principle of the stylus profilometer is based on the electromechanical measuring method (contact profile) similar to AFM. Dektak 6M software was used to control the stylus contact profilometer. The working setup of the stylus contact profilometer is shown in Figure 2.8 [75].

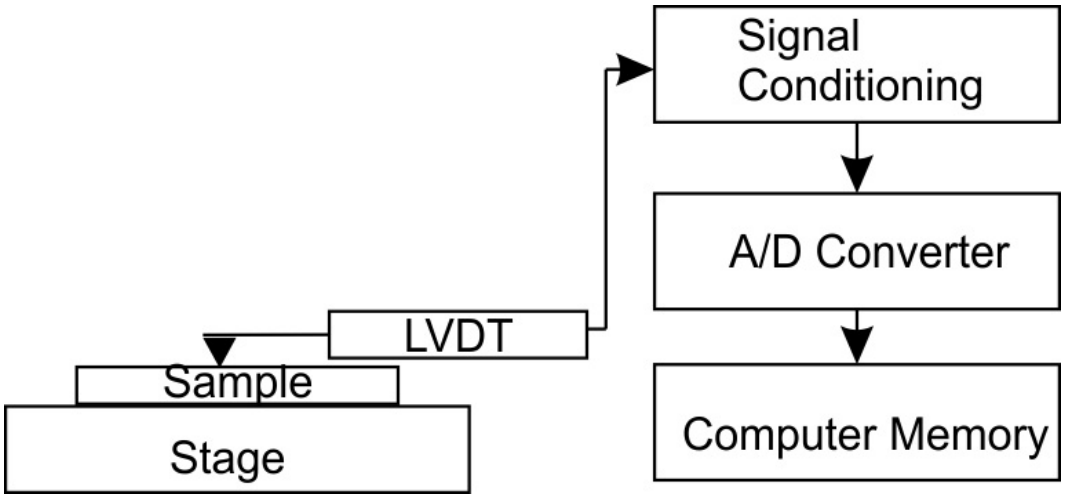

Figure 2.8: Schematic picture of the stylus profilometer.

One end of the cantilever is attached to a diamond tip having a typical diameter of 5μm and the other end is coupled to the Linear Variable Differential Transformer (LVDT). The LVDT is fixed to the tower and the sample holder can be moved according to the requirement such as scan length, speed and tip force

on the sample. As the sample holder moves with a constant speed, the diamond tip rides over the sample and the tip translates the variations on the surface of the sample. Hence the core of the LVDT produces an electrical signal of the diamond tip moment to the signal conditioning. In signal conditioning, the LVDT scales the AC electrical signal proportional to the position change and then the analogue signals are converted into the digital signal which is then stored in the computer memory [75].

2.4 Contact Angle Measurement

When a liquid drop is dispensed on a solid surface, the liquid drop either spreads or contracts by balancing the three interfacial tensions; i.e. liquid-solid, solid-vapour and liquid-vapour interfacial tensions. Below the capillary length scale, where surface forces dominate gravity, the nearspherical surface profile of a sessile droplet is maintained close to the contact line, and a tangent drawn at the intersection can be used to measure the contact angle.

The wettability of the liquid on the solid surface can be quantified by measuring the contact angle of the drop. The contact angle (θ) is an angle between the direction of the tangent to the solid-liquid and the direction of the tangent to the liquid-vapour as shown in the Figure 2.9.

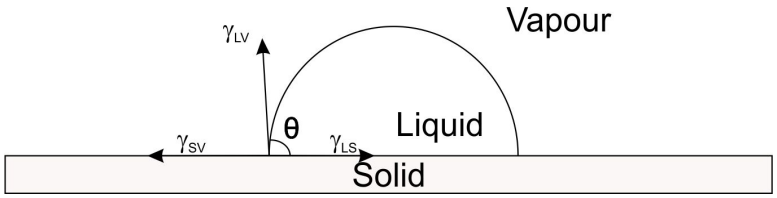

Figure 2.9: Droplet of the liquid on a solid substrate. Three tangential lines are the liquid-solid interfacial tension (γ_{SL}), solid-vapor interfacial tension (γ_{SV}) and liquid-vapor interfacial tension (γ_{LV}).

The advancing and the receding contact angles are dynamic angles when the droplet is in the process of spreading or receding/evaporating.

2.4.1 Contact Angle Measurement Methods

There are different approaches to measure the contact angle, one of them is the optically tensiometry technique. Tensiometry is the setup of back light source, two lenses, translation stage in 3 axis, image capture and drop shape analysis software (section 3.4). Drop Shape Analysis [DSA] software (KRUSS) was used to analyse the sessile drop shape by fitting the one of a number of possible mathematical expressions [76]. DSA software can calculate the static contact angle and dynamic contact angle of the drop.

When a liquid drop is dispensed on a solid surface after some time it reaches an equilibrium state where the three phase line of the drop doesn't change. The images of the droplet from side view taken from JVC camera are illustrated in figure 2.10. The baseline (red line under the drop in the figure 2.10) of the drop was adjusted manually in the drop shape analysis software. Once camera is set, the magnification was calibrated by measuring a standard and entering the known and measured values on the Calibration tab. Software determines the bright pixels from square root of the secondary derivative of the brightness level in the image and then automatically it results the point of great change in brightness such as drop boundary. There are five mathematical methods to fit the shape of the drop boundary and to measure the contact angle, height and the width of the drop; (1) circle method, (2) height & width method, (3) tangent 1 method, and (4) sessile drop fitting method.

Height and Width method : In this method the software determines the height and width of the drop from the fitting. A rectangle is drawn that encloses the counter line (red boundary line of the droplet) providing the values of height and width of the droplet. The rectangle is regarded as a circle segment in this method and the contact angle of the drop is calculated from the rectangles height

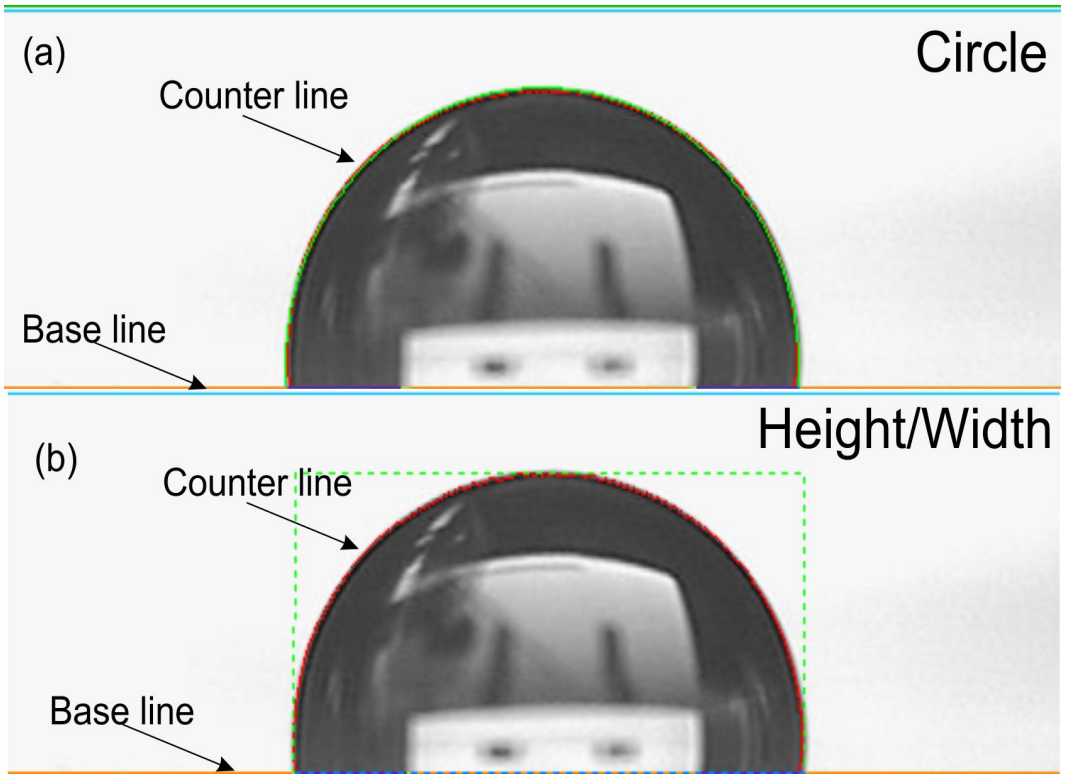

Figure 2.10: The image illustrate the circular method and height & width method fitting in drop shape analysis software to measure the contact angle of the 1, 2 propylene glycol drop on hydrophobised SU8 layer.

and width relationship shown in equation 2.1.

$$\theta = 2arctan\left(\frac{2h}{w}\right) \tag{2.1}$$

Where, θ is the contact angle of the sessile drop, h is the height of the drop and w is the width of the drop.

Circle fitting method: This method is similar to the Height-Width method. In this method the counter line fits to a circular segment function and then the contact angle is determined from circular segment (figure 2.10 a). The advantage of this method is that θ can be calculated in the presence of the needle within the field of view unlike the Height-Width where the boundaries of the droplet need to be well defined.

Tangent 1 method: In this method, the complete profile of the sessile drop is fitted using a general conic section equation. The slope at the 3 phase contact point, which is the intersection point of the baseline and contour line, is derived from the conic section equation, and hence the contact angle of the drop is calculated.

Tangent 1 method requires an excellent image quality especially in the area of the 3 phase contact point.

Sessile drop fitting (Young-Laplace) method : theoretically this method is the most precise method to calculate the contact angle and the most complicated method as well. The fitting considers two parameters the first one is the interfacial effects which produces the drop shape and second one is the weight of the liquid which makes a drop to distort. After fitting the drop with Young-Laplace equation, the contact angle of the drop is obtained from the slope of the contour line at the 3 phase point. The major drawback of this method is that the contact angle must be greater than 30^o.

Mainly height and width method and circular method are more accurate for smaller drops where the droplet width is less than the capillary size which is

similar to the theoretically assumed spherical cap form. Tangent method and sessile drop fitting (Young-Laplace) method are suitable for the bigger volume droplets where the droplet is no more spherical cap shape. However the contact angles, were measured using H&W method and circular method, are compared with the theta which was measured manually using Image J. The contact angle measurements standard will be traceably accurate to $\pm 1.5^o$ for above 25^o. In image J software, an angle between the tangent of the solid-liquid and the tangent of the liquid-vapour.

2.4.2 Static Contact Angle

In static contact angle measurement, the contact angle of the 1, 2 propylene glycol drop was not changed during the measurement. A drop of the 1, 2 propylene glycol was gently dispensed on the hydrophobic SU8 layer. The droplet was examined from the side view of the drop using the camera (JVC) and in the meantime the optical settings were adjusted such as focus, magnification and contrast. The scale is essential to be calibrated for the DSA software. The image of the drop which was captured from the side view using the camera was uploaded to the DSA. The base line of the drop was determined manually in the drop shape analysis software and then the contact angle measured using circle and height & width method.

2.4.3 Dynamic Contact Angle and High Speed Photography

In dynamic contact angle measurement, the advancing contact angle was measured with respect to the time using the drop shape analysis as shown in figure 2.11. 1, 2 propylene glycol droplet was dispensed on the interdigitated device and the voltage was applied to the interdigitated electrode device resulting in the drop being spread along the electrodes. The drop was examined from two

different views 1) the perpendicular view using a high speed camera (Hotspot, NAC image technology) to record the dynamic contact angle with a frame rate of 3000 frames per second 2) Top view to image the drop spreading and recovering along the electrodes. The base line of the drop was determined manually in the drop shape analysis software and video calculation function allowed to measure the contact angle, height and diameter of the drop as a function of the frame.

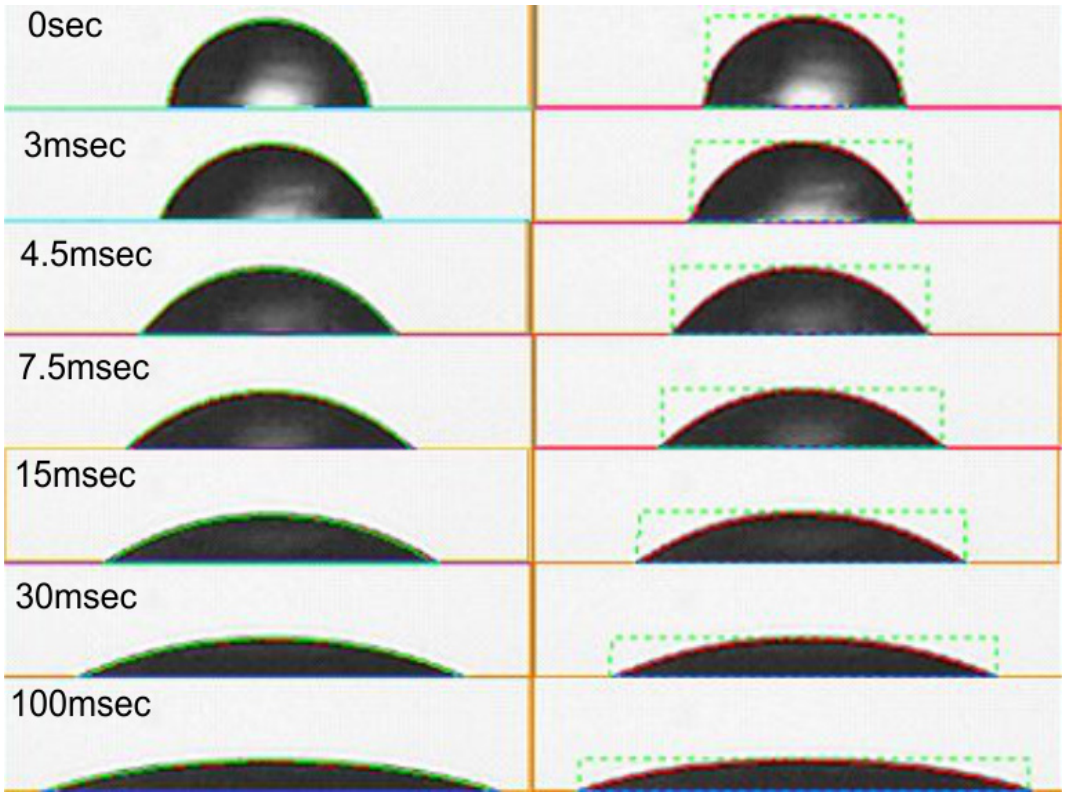

Figure 2.11: The figure illustrates that the advancing contact angle was evaluated with respect to time using circle method (Left hand side) and height & width method (right hand side) in drop shape analysis software. The droplet spreading has performed on 40μm electrode width at 230V.

2.5 Mach-Zehnder Interferometer

2.5.1 Principle

A Mach-Zehnder interferometer was used to measure the change in optical path length produced by a layer of transparent materials which works on a two beam

interference technique. The basic principle of the interferometer is dividing the beam into two separate beams, travelling in two different paths and recombining the two beams as demonstrated in figure 2.12. At beam splitter (BS1) a coherent

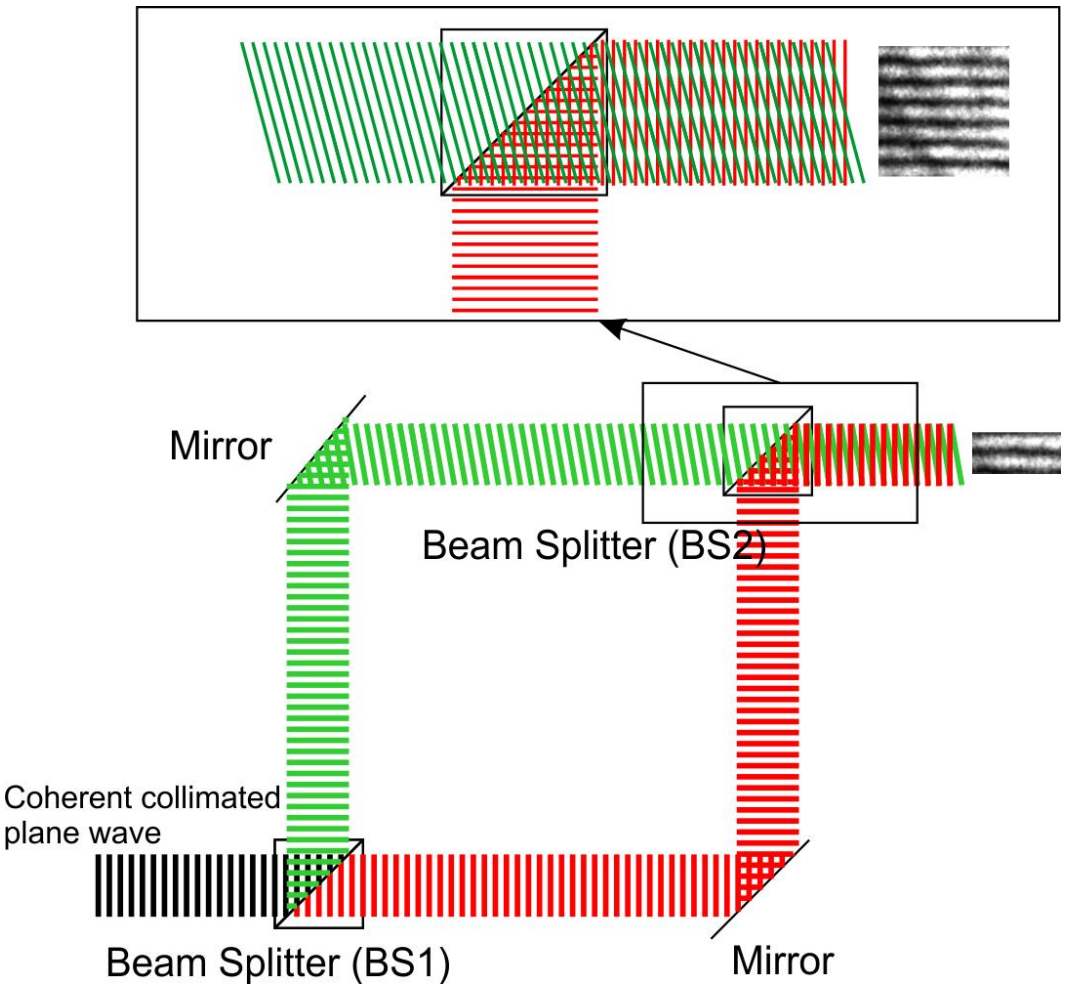

Figure 2.12: Working principle of the interferometer and the inner picture illustrates the recombination of the sample beam and reference beam.

collimated beam is divided into two separate 50% intensity beams, the first beam travelling horizontally and second beam travelling vertically. These two different beams travelling either horizontally or vertically are reflected using two different mirrors tilted at 45^o to reflects both beams towards the another beam splitter (BS2) as shown in Figure 2.12 If the lengths of the two separate arms of the interferometer are exactly the same then the original beam with the original full intensity is reconstructed at BS2. And also one of the mirror was slightly rotated from the 45^o angle so the beams are slightly inclined on each other after

recombination of the two beams at the second beam splitter (BS2). The variation in the phase causes the interference pattern in a series of parallel linear fringes with a sinusoidal intensity profile as a function of the vertical coordinates [49, 72, 77].

2.5.2 Experimental setup

The Mach-Zehnder interferometer is divided into three parts; beam source, interferometer main body and image capture system. The light source is coherent, collimated and monochromatic with a wave length of 632nm produced by a 17mW He-Ne laser source. The beam polarisation is controlled by the half wave plate ($\lambda/2$). The resulting beam is expanded and filtered using a spatial filter system.

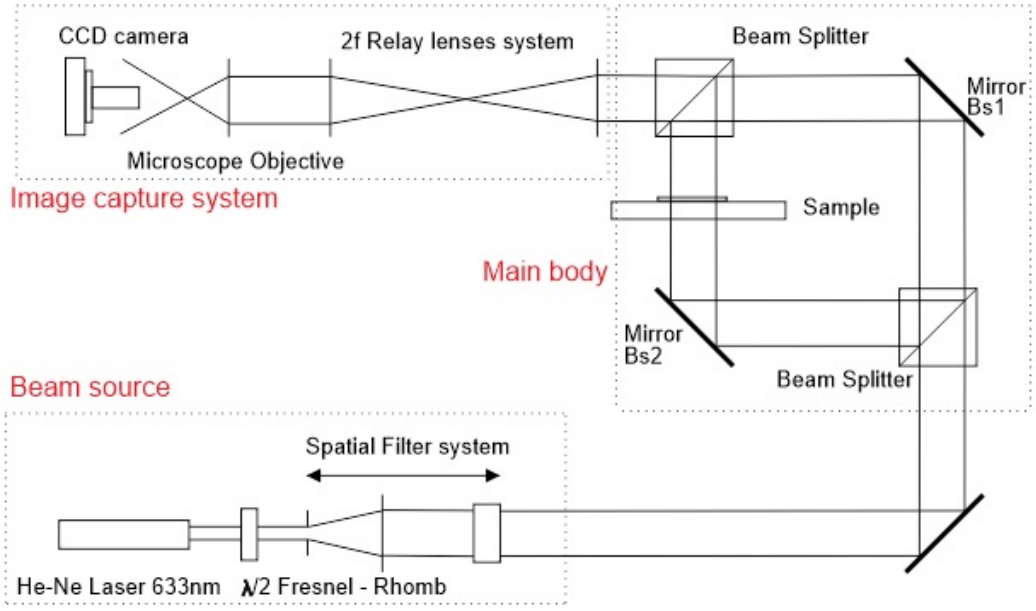

Figure 2.13: Schematic representation of the interferometer experimental setup.

In the main body of the interferometer the expanded beam is divided in two beams, reference beam and sample beam, by a 50:50 beam splitter. The sample beam is the beam which travels through the samples. The main body consists of the mirrors which tilts the beams at 45^o to guide the reference beam and the sample beam towards the second beam splitter (BS2).

In image capture system, the localized pattern is spatially transformed through the relay lens system into the microscope object to expand the pattern and the received pattern is recorded using CCD camera. The relay system is necessary because of the short working distance of the objective.

2.5.3 Measuring the oil thickness by Fractional Fringe Shift

A transparent isotropic sample is placed in a sample holder through which the sample beam passes resulting in a change of the optical path length which causes the fringe shift. Using the refractive index value of the material the surface height can be measured and it is possible to profile the shape of the material by using the relative shift of the fringes.

2.6 Optical diffraction measurement

When a voltage is applied to the interdigitated electrodes it creates a highly non-uniform electric field which is periodic. In this non-uniform electric field a dielectric material experiences a dielectrophoretic force in the direction of increase in the magnitude of electric field gradient and creates the undulation shape at the oil/air interface. The undulation creates a periodic variation in the optical path length of light transmitted through it. This optical path length leads to interference and the creation of a series of diffracted spots. The amplitude of the undulation depends upon the applied voltage and liquid properties. The experimental setup of the optical diffraction measurement, shown in figure 2.14, was used to characterize the dynamic effect of the periodic undulation and to fabricate the solid grating.

The optical diffraction measurement setup was constructed using a laser diode (543nm, green laser), two silver mirrors (PF10-03-P01, Thorlabs, uk), aperture, diverging lens, three Plano concave lens, three Photo diode detector(DET36A/M,

Si biased detector, 350-1100nm, THORLABS, UK) and a oscilloscope (DSO6014A, Agilent Technologies, U.K.).

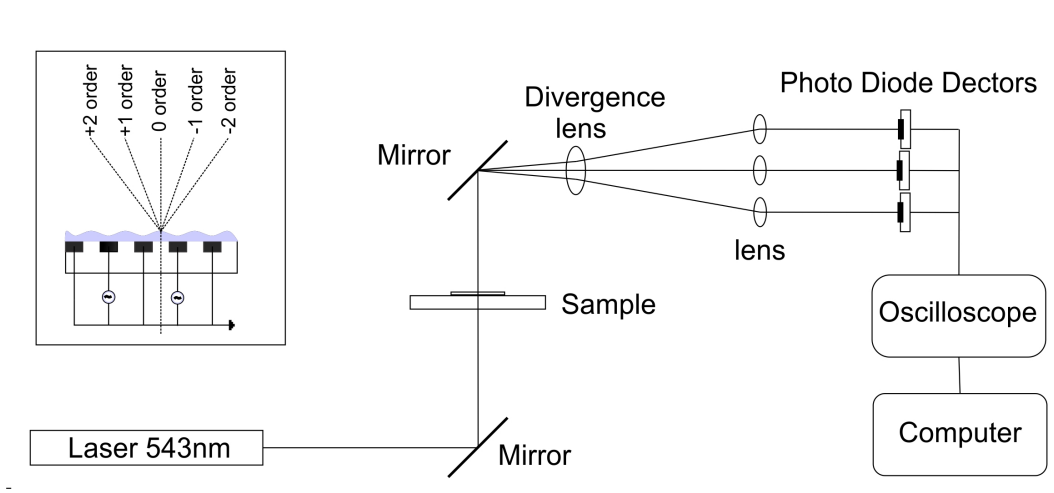

Figure 2.14: Schematic diagram of the working setup for optical diffraction measurement and the inset picture shows the diffraction creation from wrinkle surface.

The interdigitated device was placed in a sample holder and a drop of liquid was dispensed on the IDT. When the voltage was applied to the electrodes, it created the undulation (wrinkles) at the liquid and air interface. A green laser beam (543nm laser diode) was reflected at an angle of 90^o from first mirror and was transmitted through the liquid gratings (undulation surface) hence, the diffraction order was created which was then reflected at 90^o from the second mirror to photo diode detectors. An aperture was used to allow only three diffracted orders such as zero, first and second order either positive or negative side. The three diffracted orders were diverged at divergence lens and the combination of the divergence lens and plan concave lens allowed the diffracted orders to be transmitted to the individual Photo diode detectors which measure the intensity of the light. These detectors were connected to the oscilloscope and the output voltage of the detectors was stored in the computer via oscilloscope.

Chapter 3

Dielectrospreading

3.1 Introduction

The literature suggests that the wetting of solid surface can be modified by changing the surface chemistry [29], surface topography [78], or by the external force on the liquid including electrostatic [9]. In recent years Electrowetting on Dielectric (EWOD) has been shown to be an effective method to control the contact angle of the drop which describes the wetting on the solid surface [9, 79]. Briefly summarising electrowetting on a dielectric layer, a continuous electrode is coated with a super hydrophobic dielectric layer and a conductive liquid is dispensed on to dielectric layer. A voltage applied between the liquid and the electrode causes the liquid contact angle to decrease. The EWOD phenomenon is important for wide range of applications such as: microfluidics [6], digitally controlled droplet-based chemical reactions, biological assays [38, 39], liquid based optics [34, 40, 41], control of the mixing of two or more liquids, dispensing of liquid and droplet motion [42] in microfluidics. EWOD requires a conducting liquid and a thin dielectric layer that is resistant to dielectric breakdown.

Liquid dielectrophoresis, in this approach an external electrode does not need to be contacted with a liquid droplet to drive the three phase contact line of the droplet unlike electrowetting on dielectric (EWOD) approach where an external electrode is attached to the liquid droplet. The main advantage of this approach is being prevented from the chemical reaction between the external electrode and the droplet. A droplet is dispensed on the electrode device which is coated with super hydrophobic dielectric layer, and the drop forms a spherical shape by balancing the three interfacial tensions. When the voltage is applied to the conductive layer the electric field is localized in the liquid with depth of penetration. When a dielectric material (liquid) experience a uniform field, the force on the two charges of the dipole is equal which is induced by polarization. But the force on the two charges will not be equal when the electric field is non-uniform, hence, an overall force occurs on the dipole and bulk force on liquid causes liquid motion

[3, 4]. This is called Liquid-Dielectrophoresis (L-DEP). The resulting of the net dielectrophoresis force causes the droplet contact angle decreases. We can use a conductive liquid in the L-DEP but it requires a high frequency AC voltage to activate the liquid area modulation [80].

This chapter demonstrates dielectric liquid wetting and dewetting on noncontacting interdigitated electrodes under the influence of a nonuniform electric field. Voltage control of contact angles over a wide range with a low degree of contact angle hysteresis, and anisotropic spreading has been achieved. The theoretical relationship of the spreading between the cosine of the contact angle and square of the applied voltage (Dielectrowetting equation) is also derived and demonstrated experimentally [81].

An isotropic spreading and the dewetting of a dielectric liquid droplet on the radial and the circular electrode geometry using liquid dielectrophoresis (L-DEP) is also illustrated in this chapter, which extends the Yu-chi Wang [13] and Chin-Cheng Cheng [12] approach. Preliminary work will be presented on the anisotropic spreading of a liquid droplet in another immiscible liquid using L-DEP.

3.2 Device geometry

An interdigitated electrode array pattern area 5mm × 5mm was transferred onto pre coated indium tin oxide (ITO) thickness of 25nm on borosilicate glass using standard photolithography (discussed in section 2.2.1). A schematic diagram of the interdigitated electrodes is shown in figure 3.1 in the x-y plane view and the z-y plane view. The electrode width is equal to the space between the electrodes. 20μm, 40μm and 80μm line width of the interdigitated electrodes were fabricated for the static study of the dielectrowetting.

A dielectric layer (SU8) was fabricated on the interdigitated electrode array with a typical thickness of 2μm to help prevent dielectric breakdown. The

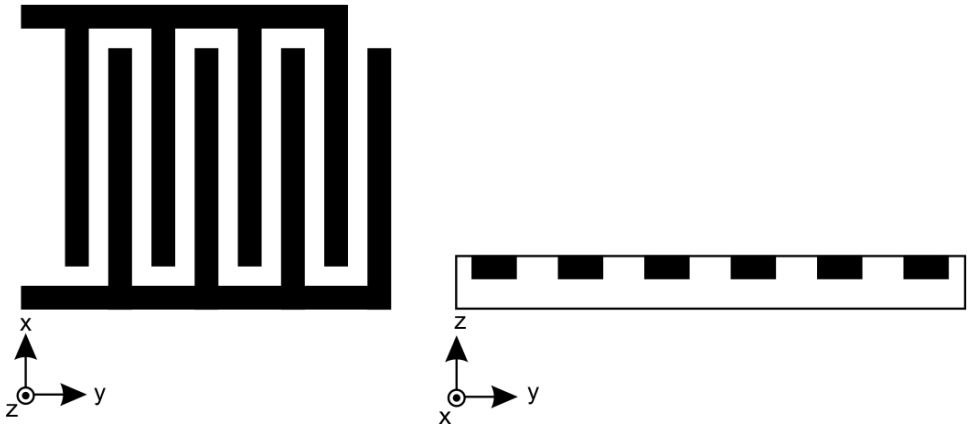

Figure 3.1: Image shows top view (x-y view) and side view (z-y view) of the interdigitated electrodes whereas line width is equal to the gap between the electrodes.

fabrication process was discussed in the section 2.2.4. In order to increase the hydrophobic nature of the SU8 layer surface, the SU8 layer was treated with a Granger solution (Granger's Extreme Wash-in, Grangers International Ltd, Alfreton, Derbyshire, UK) consisting of fluorocarbon emulsified in water with a detergent (a process discussed in section 2.2.5).

Pinning of the three phase contact line of the droplet due to defects (lumps) in the hydrophobic SU8 surface is a most common problem in dielectrowetting experiments; it can result in asymmetry in the contact angle at the right and left hand of the droplet from x-direction. Another common problem is dielectric breakdown in the dielectrowetting, which is due to the micro holes in the dielectric layer (SU8). Samples were chosen which have a uniform surface layer without any defects including lumps or micro holes on the SU8 layer.

3.3 Experimental set-up

During the wetting and dewetting experiments the droplet was monitored perpendicular to the electrodes array (from the x-direction) to measure the contact angle of the drop as a function of applied voltage and from top view to characterize the three phase contact line shift along the electrodes (x-direction). The

experimental set-up is consisted of two cameras with lens attached, two back light sources and a computer as shown in figure 3.2.a.

An Interdigitated electrode device was mounted in sample holder and was con-

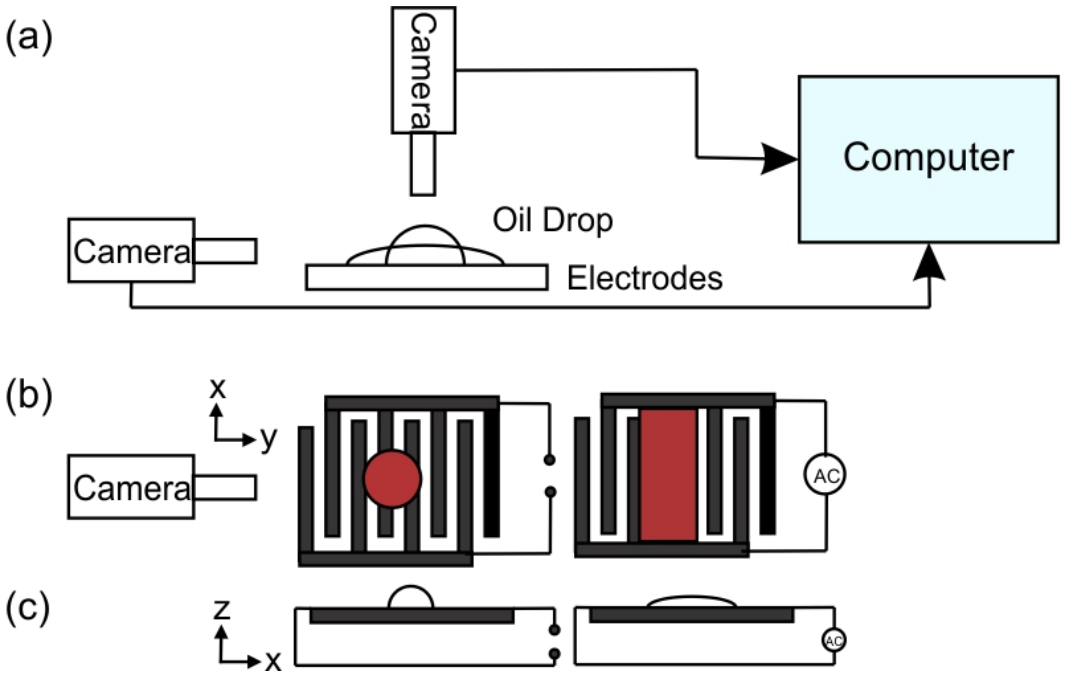

Figure 3.2: Schematic representation of the dielectrowetting experimental set-up; figure (a) shows that the droplet monitor from the top and perpendicular to the spreading, the two cameras controlled by drop shape analysis software (DSA); (b) shows that top view (x-y plane) of the droplet spreading along the interdigitated electrodes with equal line gaps and widths when the voltage was applied; (c) shows that the perpendicular (x-z plane) view of the droplet spreading when voltage was applied.

nected with the electrical addressing unit (described in section 2.2.1). one of the cameras (TK-C920U, security camera, JVC) was mounted perpendicular (x-direction) to the interdigitated electrode array and a back light source was mounted at the side of the droplet to get better contrast of the image. The second camera was mounted above the droplet with a back light source underneath the droplet holder. The side camera was fitted with a 4× objective lens and whilst the top camera was fitted with a 4× objective lens. The two cameras were controlled by using Drop Shape Analysis software (KRUSS GmbH, Hamburg, Germany). Schematic pictures of the droplet spreading along the electrodes under applied voltage from x-y plane (top) view and x-z plane (side) view are shown

in figure 3.2.b and c.

3.4 Dielectrowetting equation

Figure 3.3 shows the schematic diagram of the dielectrowetting in x-z plane. A droplet is rested on an interdigitated electrode array. When the voltage is applied across the electrode array, the electric potential exponentially decays into the liquid with penetration depth. The 2d potential profile in the x-z plane approximated by this 1d potential profile, is given in the equation 3.1.

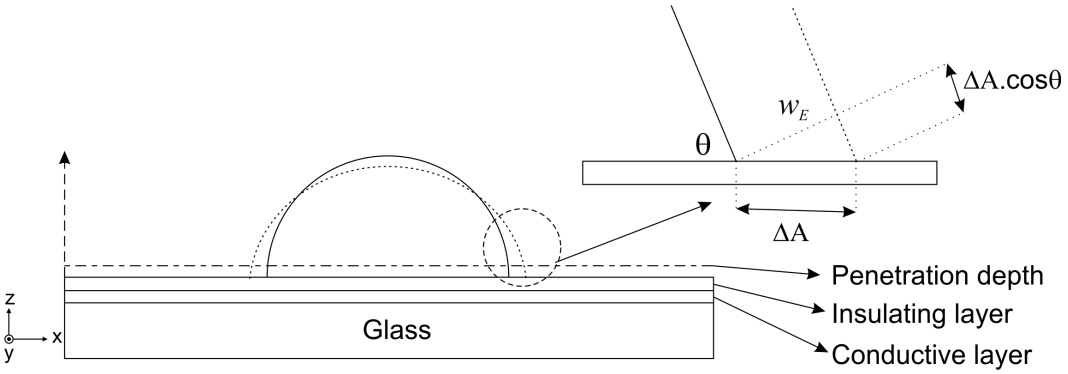

Figure 3.3: Schematic representation of the drop on the interdigitated electrodes (dielectrowetting). Inner picture is an illustration of three phase contact line (dash line) at no voltage, Young's equilibrium, and (dotted line) at equilibrium state of applied voltage.

$$V(z) = V_o exp(-2z/\delta) \tag{3.1}$$

where, V_o is the voltage difference between the adjacent electrodes and δ is the penetration depth.

The electric field, E is determined by the gradient of the potential;

$$E = -\nabla V(z) = \frac{2V_o e^{\frac{-2z}{\delta}}}{\delta} \tag{3.2}$$

The electrostatic energy per unit area W_E, is found by integrating the dielectric energy and electric field, given in equation 3.3.

$$W_E = \int_0^h \frac{\varepsilon_o \varepsilon_r E.E}{2} \, \mathrm{d}z. \tag{3.3}$$

where, ε_r is the dielectric constant of the liquid, ε_o is the vacuum permittivity.

Using equation 3.2 gives;

$$W_E = \frac{\varepsilon_o \varepsilon_r}{2\delta^2} \int_0^h 4V_o^2 exp(-4z/\delta) \, \mathrm{d}z. \tag{3.4}$$

$$W_E = \frac{-\varepsilon_o \varepsilon_r V_o^2}{2\delta} (exp\left(\frac{-4h}{\delta}\right) - 1) \tag{3.5}$$

It will be assumed that the height of the liquid is much higher than the penetration depth, hence exp($\frac{-4h}{\delta}$) $\longrightarrow$0.

$$W_E = \frac{\varepsilon_o \varepsilon_r V_o^2}{2\delta} \tag{3.6}$$

The electrostatic energy is therefore given in terms of the dielectric constant of the liquid, applied voltage squared and penetration depth.

Due to the highly non-uniform electric field which moves the contacted line by distance Δx, giving an increase in contact area $\Delta \mathrm{A} = L_o \Delta x$. The solid-vapor interface is replaced by the solid-liquid interface with area ΔA, and in addition the surface area of the liquid-vapor interface is increased by $\Delta \mathrm{A} \cos\theta$ resulting in a surface free energy increase of γ_{LV} ΔA $cos(\theta)$ [28]. The additional energy on the droplet, -W_E, is considered in the nonuniform potential approximation of equation 3.1 and assuming the height of the drop is larger than the penetration depth.

$$\Delta F = \Delta A cos(\theta) \gamma_{LV} + \Delta A(\gamma_{LS} - \gamma_{SV}) - W_E \Delta A \tag{3.7}$$

In electrostatic energy equation 3.6, ε_r is replaced by $(\varepsilon_r - 1)$ since, in real time, the air is replaced by the dielectric liquid (dielectric constant of air is 1) of an

area of ΔA, and it is illustrated in the inner figure 3.3.

$$\frac{\Delta F}{\Delta A} = cos(\theta)\gamma_{LV} + (\gamma_{LS} - \gamma_{SV}) - \frac{\varepsilon_o(\varepsilon_r - 1)V_o^2}{2\delta} \tag{3.8}$$

At the equilibrium ΔF / ΔA = 0 giving:

$$0 = cos(\theta)\gamma_{LV} + (\gamma_{LS} - \gamma_{SV}) - \frac{\varepsilon_o(\varepsilon_r - 1)V_o^2}{2\delta} \tag{3.9}$$

Therefore,

$$cos(\theta) = \frac{(\gamma_{SV} - \gamma_{LS})}{\gamma_{LV}} + \frac{\varepsilon_o(\varepsilon_r - 1)V_o^2}{2\delta\gamma_{LV}} \tag{3.10}$$

Since $\cos\theta_y = \frac{(\gamma_{SV} - \gamma_{LS})}{\gamma_{LV}}$, hence equation 3.11 is replaced by equation 3.10.

$$cos(\theta) = cos(\theta_y) + \frac{\varepsilon_o(\varepsilon_r - 1)V_o^2}{2\delta\gamma_{LV}} \tag{3.11}$$

Where θ_y is a equilibrium contact angle of a droplet at no voltage (Young's contact angle). Equation 3.11 is the dielectrowetting equation which describes how Liquid dielectrophoresis (LDEP) modifies the wetting property of the liquid; it can be referred as L-DEP modified Young's law. The voltage induced wetting depends on the penetration depth δ and the permittivity difference between the dielectric liquid and air $\varepsilon_o(\varepsilon_r - 1)$.

3.5 Investigation of Dielectrowetting on IDT electrodes

In order to test the prediction of the dielectrowetting induced wetting and dewetting, a 1, 2 propylene glycol droplet was dispensed into the centre of the interdigitated electrode array. Here 80μm line width IDT was used and it was coated with a 2μm SU8 layer. The volume of the droplet was controlled using the Gilsen 0.1-2μl Micro-pipette (Gilson, Inc., Middleton,USA). This device was mounted

in the experimental set-up where it was connected to the voltage addressing unit. When a voltage was applied to each alternative electrode finger with the interposed electrodes at earth potential in an interdigitated array of electrodes, it creates a highly non-uniform electric field which is periodic and determined by the electrode pitch.

d is the width and gap between the electrodes, **2d** is the pitch of the electrode which is twice the size of the electrode width, electrical period is **4d** and a wave number k $=\pi/2$d. When the voltage is applied to the interdigitated electrodes, electric field decays in to 1, 2 propylene glycol layer with depth of penetration $\delta=4\text{d}/\pi$.

In this non-uniform electric field, the 1, 2 propylene glycol experiences the dielectrophoretic force towards the high field gradient which results in the droplet being spread along the electrodes. 1, 2 propylene glycol is a high dielectric medium (dielectric constant of 27.5). The oil drop spreading in the presence of voltage is due to dielectrophoresis and the oil drop recovery close to its original shape after removing the voltage is due to restorative force generated by surface tension of the oil. Before applying the voltage to electrodes, images of the 1, 2 propylene glycol drop were captured 5min after the deposition. The contact angle of the 1, 2 propylene glycol was measured using drop shape analysis software. In DSA software, the height and width method and the circular method are more accurate for smaller drops where the droplet width is less than the capillary size which is similar to the theoretically assumed spherical cap form. In our experiments, the droplet size is less than the capillary size.

A 10 kHz sinusoidal voltage was applied and was increased in steps of 10V from 0V to 312V with delay of 30sec in between each step to allow the droplet to reach equilibrium state. An anisotropic spreading along the electrodes, without leaking to the neighbouring pitch, was observed from the top view as voltage was increased and then decreased as shown in figure 3.4. The periodicity of

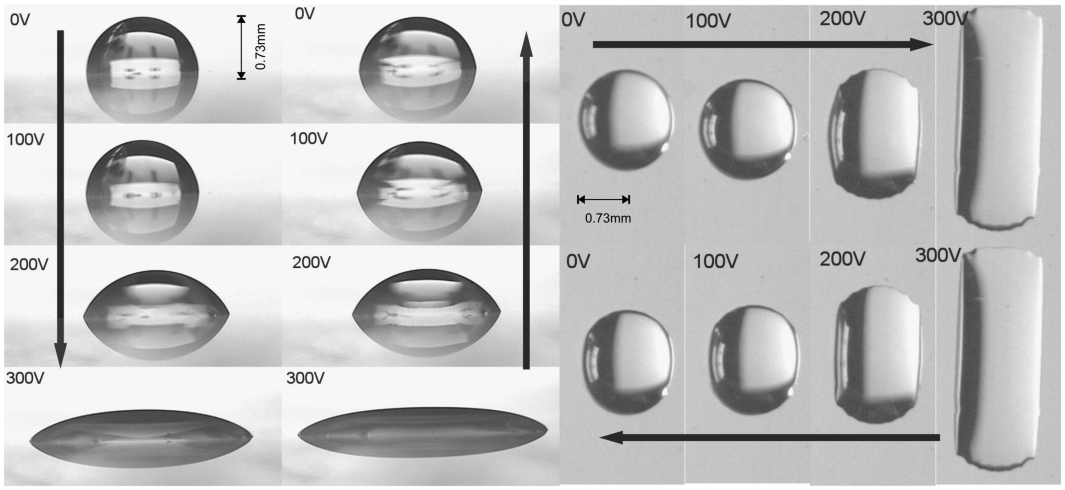

Figure 3.4: Images show 1, 2 propylene glycol droplet wetting and dewetting on the interdigitated electrodes when the voltage is increased and subsequently decreased; (left side) x-z view (perpendicular the electrode array) to spreading to monitor the contact angle and (right side) top view monitor the anisotropic spreading and recovering.

the electrodes creates an energy barriers to lateral spreading perpendicular to the electrodes and the droplet spreads along the electrodes as shown in figure 3.4 (right hand side). The contact angle of the 1, 2 propylene glycol reduces monotonically as a function of increasing voltage, and then steadily increases as a function of decreasing voltage as shown in figure 3.4. The quasistatic contact angle of the 1, 2 propylene glycol with applied voltage was obtained using the height - width method and the drop shape analysis software (discussed in section 2.5.2).

3.5.1 Relationship between the $cos(\theta)$ vs V^2

The initial contact angle of the droplet was 96^o at 0V, fell to 23^o as the voltage was increased to 312V, and then gradually the contact angle increased to 84^o as voltage decreased to zero voltage. The quasistatic change of the contact angle with applied voltage is shown in figure 3.5. The solid lines in the figure 3.5 are fits to equation 3.11 of the voltage increasing and decreasing data. The initial data point of the contact angle vs voltage, the contact angle of the drop at 0V, lies above the fit to the contact angle as the applied voltage is increased due to

pinning and it being above the receding angle for the surface. The first four data points of the contact angle recovery as voltage decreased from maximum to 0V lies away from the trend line due to the change from a receding contact angle to an advancing contact angle. The hysteresis of the contact angle was found to be around the 10^o. To check accuracy of the contact angle measurement, θ of a 1, 2 propylene glycol droplet at time (t=0) were measured using height and width method and circular method, were reported 96.3^o and 95.2^o respectively. Using two methods, the contact angle was measured at each voltage. The contact angle measurements standard will be traceably accurate to $\pm 1.5^o$ for above 25^o.

The solid lines in the inset figure 3.5 show the same fit to equation 3.11 of the

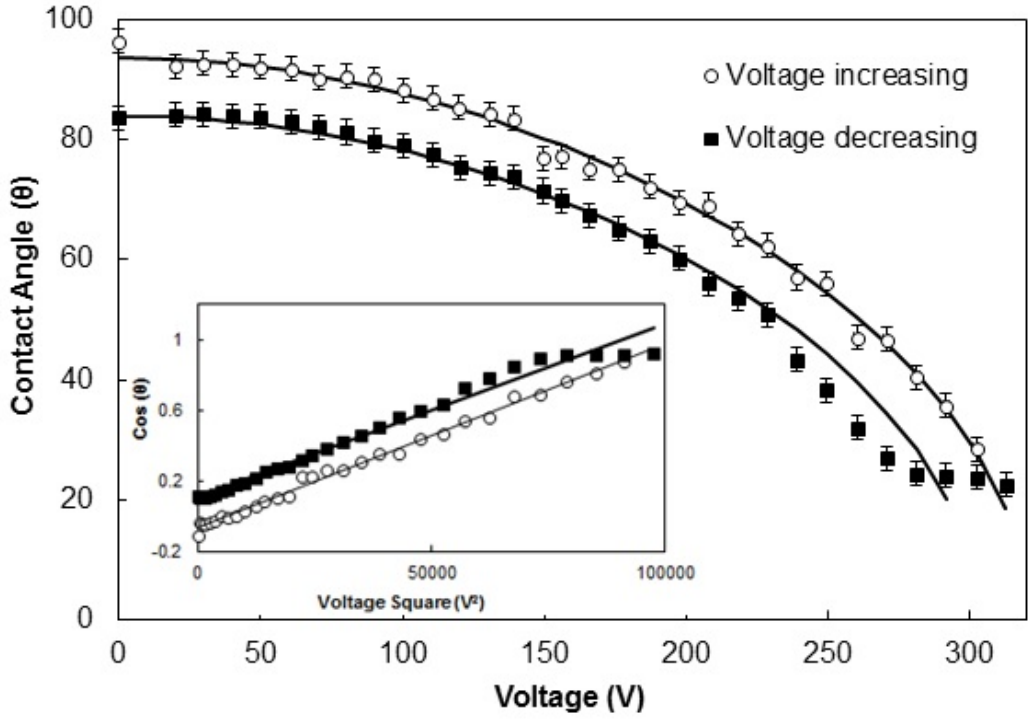

Figure 3.5: Graph illustrates the contact angle of the drop as function of voltage, incremented and decremented with a step of 10V. The inner picture shows the cosine of the contact angle as a function of the voltage squared V^2 according to the equation 3.11.

cosine of the contact angle versus applied voltage squared for forced wetting and dewetting. The linear dependence of the cosine of the contact angle as a function of the applied voltage square for wetting and dewetting condition is shown with

an offset of 6^o due to contact angle hysteresis as illustrated in figure 3.5. The linear dependence of cosθ versus V^2 is consistent with the prediction of Liquid-Dielectrophoresis (L-DEP) and we have shown the ability to spread the droplets over wide contact angle range (70^o).

3.5.2 Model for voltage reduction factor C

The slope of the experimental data for wetting is m_{exp}=1.07 $\times$ 10^{-4} V^{-2}, but, according to the L-DEP equation 3.11 is m_p = 0.39 $\times$ 10^{-4} V^{-2} 1, 2 propylene glycol (ε_l=35.0, γ_{LV}=38mN^{-1}m). To more accurately compare, we take into account that the SU-8 layer will cause a capacitive division of the voltage so that the effective voltage in the liquid, V_c, is reduced compared to that applied to the interdigitated transducers, V_o. The voltage reduction factor C is derived with a simple model.

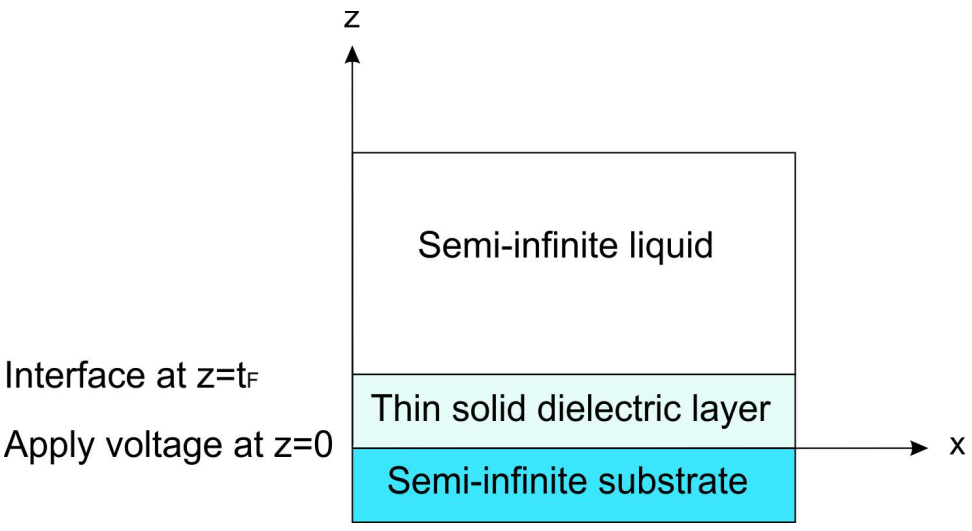

Figure 3.6: Schematic model of capacitive voltage division.

When the voltage is applied to the semi-infinite substrate (electrodes), the electric field exponentially decays in to the upper layers (dielectric layer and oil layer). And this can be modelled be a single Fourier component.

Let $V_o$cos(kx) be the actual voltage applied at the substrate and k is the wave number.

$$V_{applied}(x,z) = V_o \cos(kx) exp(-kz) \tag{3.12}$$

The potential profiles in the dielectric layer and the oil can be modelled by equations 3.13 and 3.14, which satisfy the Laplace equation.

$$V_{dielectric}(x,z) = A\cos(kx)exp(-kz) + B\cos(kx)exp(kz) \tag{3.13}$$

$$V_{oil}(x,z) = C\cos(kx)exp(-kz) \tag{3.14}$$

Where, $V_{dielectric}$ is the voltage in the thin solid dielectric layer and V_{oil} is the voltage in the oil, A, B and C are coefficients that can be obtained by applying the boundary conditions.

Boundary conditions :

1. Continuity of the potential at the interfaces z=0.

$$V_{applied}(x,0) = V_{dielectric}(x,0) \tag{3.15}$$

$$V_{applied}(x,0) = V_o \cos(kx) \tag{3.16}$$

$$V_{dielectric}(x,0) = A\cos(kx) + B\cos(kx) \tag{3.17}$$

$\Longrightarrow$

$$V_o = A + B \tag{3.18}$$

2. Normal component of the displacement field continuous at z=t_F

$$\varepsilon_o \varepsilon_{liquid} \left[\frac{dV_{liquid}(x,z)}{dz}\right]_{z=t_F} = \varepsilon_o \varepsilon_{dielectric} \left[\frac{dV_{dielectric}(x,z)}{dz}\right]_{z=t_F} \tag{3.19}$$

$\Longrightarrow$

$$\varepsilon_{liquid} C e^{-kt_F} = \varepsilon_{dielectric}(Ae^{-kt_F} - Be^{kt_F}) \tag{3.20}$$

3. Tangential component of the electric field continuous at z=t_F

$$\left[\frac{dV_{liquid}(x,z)}{dz}\right]_{z=t_F} = \left[\frac{dV_{dielectric}(x,z)}{dz}\right]_{z=t_F} \tag{3.21}$$

$\Longrightarrow$

$$Ce^{-kt_F} = (Ae^{-kt_F} - Be^{kt_F}) \tag{3.22}$$

Equations 3.18, 3.20 and 3.22 can be solved to give the A, B and C coefficients.

$$A = \frac{V_o}{1 + \left(\frac{\Delta\varepsilon}{\varepsilon}\right) e^{-2kt_F}} \tag{3.23}$$

$$B = \frac{V_o \left(\frac{\Delta\varepsilon}{\varepsilon}\right) e^{-2kt_F}}{1 + \left(\frac{\Delta\varepsilon}{\varepsilon}\right) e^{-2kt_F}} \tag{3.24}$$

$$C = \frac{V_o \left(1 + \frac{\Delta\varepsilon}{\varepsilon}\right)}{1 + \left(\frac{\Delta\varepsilon}{\varepsilon}\right) e^{-4t_F/\delta}} \tag{3.25}$$

However, comparing the equation 3.12 and 3.14 at the same value of z does not give the same depth into the liquid, to do so we shift z by t_F. Using:

$$V_{oil}(x,z) = C\cos(kx)exp(-kz) \tag{3.26}$$

The voltage correction factor is therefore:

$$C = \frac{e^{-2t_F/\delta}\left(1 + \frac{\Delta\varepsilon}{\varepsilon}\right)}{1 + \left(\frac{\Delta\varepsilon}{\varepsilon}\right) e^{-4t_F/\delta}} \tag{3.27}$$

The limiting cases are as follows:

1. When the solid film thickness vanishes, i.e. t_F=0, the coefficient C=1.

2. When the solid film thickness is large compared to k^{-1}, the coefficient C=(1+$\Delta\varepsilon/\varepsilon$)exp(-k$t_F$).

3. When the solid film thickness is large and the film permittivity is much larger than that of the liquid, C=2exp(-kt_F).

The reduction in the voltage due to the presence of the dielectric layer can now be estimated using the parameters $\varepsilon_{liquid} = 35.0$, $\varepsilon_{liquid} = 3.0$, d = 80$\mu$m, $t_F = 2\mu$m to be C = 0.684. The predicted gradient for cosθ versus V^2 with the correction is $C^{-2}m_p = 0.834 \times 10^{-4}V^{-2}$ which is 23% smaller than the experimental value $m_{exp} = 1.07 \times 10^{-4}V^{-2}$.

3.5.3 Three different electrode pitches

Dielectrowetting experimentation with 1, 2 propylene glycol droplet was repeated on the lower width of the IDT electrodes (20μm and 40μm) which is capped with 0.6μm layer of the hydrophobic SU8. The spreading and recovering of the drop was observed as voltage was increased and decreased from 0V to 120V for the 20μm line width of IDT device and 0V to 220V for the 40μm line width of IDT device.

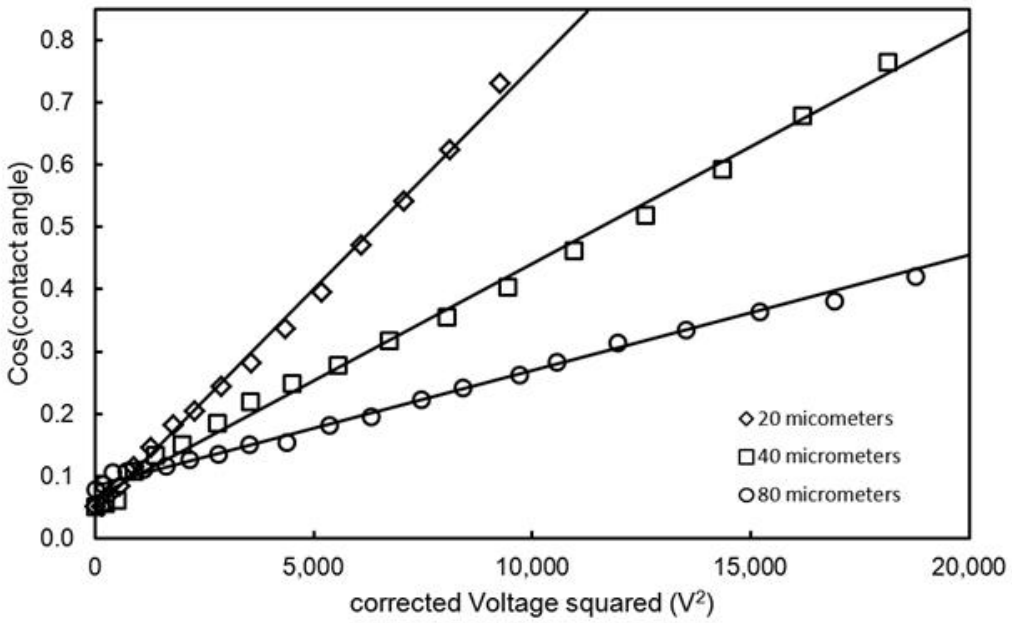

Figure 3.7: shows that the cosine of the contact angle as a function of the effective voltage square for three electrode pitches (20, 40, 80μm).

40μm: The initial contact angle of the droplet was 97^o at 0V and fallen to 22^o as the voltage was increased to 215V and then gradually the contact angle increased to 84^o as voltage decreased to no voltage. The contact angle was recovered with a hysteresis of 13^o.

20μm: The initial contact angle of the droplet was 95^o at 0V and fallen to 43^o as the voltage was increased to 156V and then gradually the contact angle increased to 85^o as voltage decreased to no voltage and recovered with hysteresis of 10^o.

Dielectric breakdown was observed when the applied voltage was more than 160V to the 20μm IDT device which because of the electrode periodicity in the structure and also it could be the dielectric layer having a thickness of 0.6μm. The linear relationship between the cos θ and V^2 was obtained by fitting the data of the increasing voltage and reducing voltage for the 20μm and 40μm as predicted from the dielectrowetting equation (equation 3.11). A slight systematic offset of the slope of the data fit was observed between the reducing voltage half-cycles and increasing voltage half-cycles for 20μm and 40μm, similar to the 80 μm data which is shown in figure 3.7.

The cosine of the contact angle is plotted against the effective voltage square for 20μm, 40μm and 80μm width respectively and the best fits were obtained for individual data set as shown in figure 3.7. The reduction factor C from the equation 44 was calculated for the 80μm and other electrode sizes with knowledge of the permittivity and surface tension of the 1, 2 propylene glycol. The C values were 0.655, 0.760 and 0.613 for the 80μm, 40μm and 20μm. The slope of the 20μm data is greater than the other data slope. The strength of the dielectrowetting being controlled by selection of the electrode pitch and the penetration depth of the electric potential was essential as illustrated in figure 3.7.

The oil drop recovers to its original shape by removing the voltage due to restorative force generated by surface tension of the oil. The data of the cosine of the contact angle as a function of the effective voltage reduction is plotted against the ratio of the effective voltage square to the pitch of the electrode geometry,

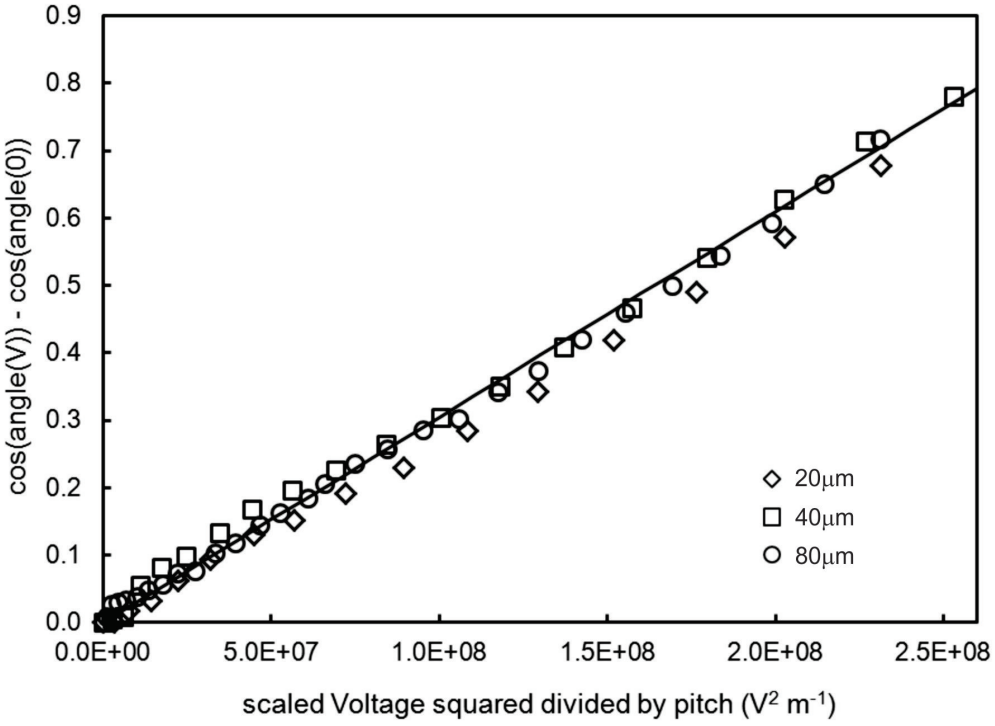

Figure 3.8: shows that the cosine of the contact angle as a function of the effective voltage square normalized by the electrode mechanical pitch for three electrode pitches (20, 40, 80μm).

where p=2d. Data of the 80μm, 40μm and 20μm are overlaid each other and solid line in the figure 3.8 is the linear fit to the data.

3.6 Investigation of the Dielectrowetting on Circular Electrodes

So far anisotropic liquid spreading has been shown on the interdigitated electrodes under the influence of the non-uniform electric field. In contrast radial and circular electrodes were introduced to produce an isotropic spreading, which may have application as a variable focus lens.

Radial electrode geometry

The radial electrode geometry, covering an area of 10mm diameter, was used to produce isotropic liquid spreading with L-DEP. The radial electrode geometry is shown in figure 3.9.a. The size of the gaps between the electrodes in the entire electrode array were all equal at 40μm. The radial geometry was divided into three distinct regions as shown in the figure 3.9. The inner region has 26 electrodes, the number of electrodes in region 2 is twice of the region 1 and the number of electrodes in the outer region is twice that of the region 2 (26, 52 and 104 electrodes respectively). The widths of the each alternative electrode were not constant in the geometry and increased with radius within each region. The size of the interposed electrodes was constant in the entire electrode array as similar to the gap between the electrodes.

The radial electrodes were fabricated using standard photolithography, as described in the section 2.2.1. A 1μm SU8 layer was fabricated on the radial electrode array to prevent dielectric breakdown and treated with Grainger solution to increase the contact angle of the droplet as described in section 2.2.5.

A droplet of 1, 2 propylene glycol was dispensed on the centre of the electrode

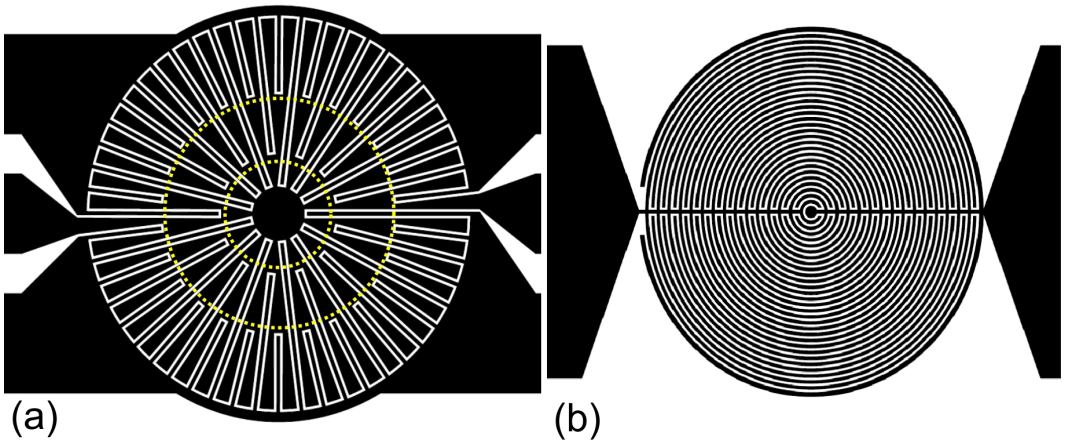

Figure 3.9: shows that top view of the (a) radial and (b) 0 offset electrodes.

array and it forms a spherical cap shape by the balance between the three interfacial tensions. The volume of the drop was controlled using a Gilsen 0.1-2μl micro pipette. The initial contact angle of the 1, 2 propylene glycol was 94^o, measured using the drop shape analysis software. A 10 kHz sine wave voltage was applied

to the each alternative electrode and interposed electrodes were earthed, hence, a non-uniform electric field was created in the droplet where the electric field is high between the electrodes. The liquid was activated to occupy the region of high field gradient due to L-DEP. Hence the three phase contact line of the drop moves equally in all directions unlike dielectrowetting on the interdigitated electrode array (IDT). Simultaneously the shape of the drop was changed.

A 10 kHz sinusoidal voltage was applied and was increased in steps of 10V from

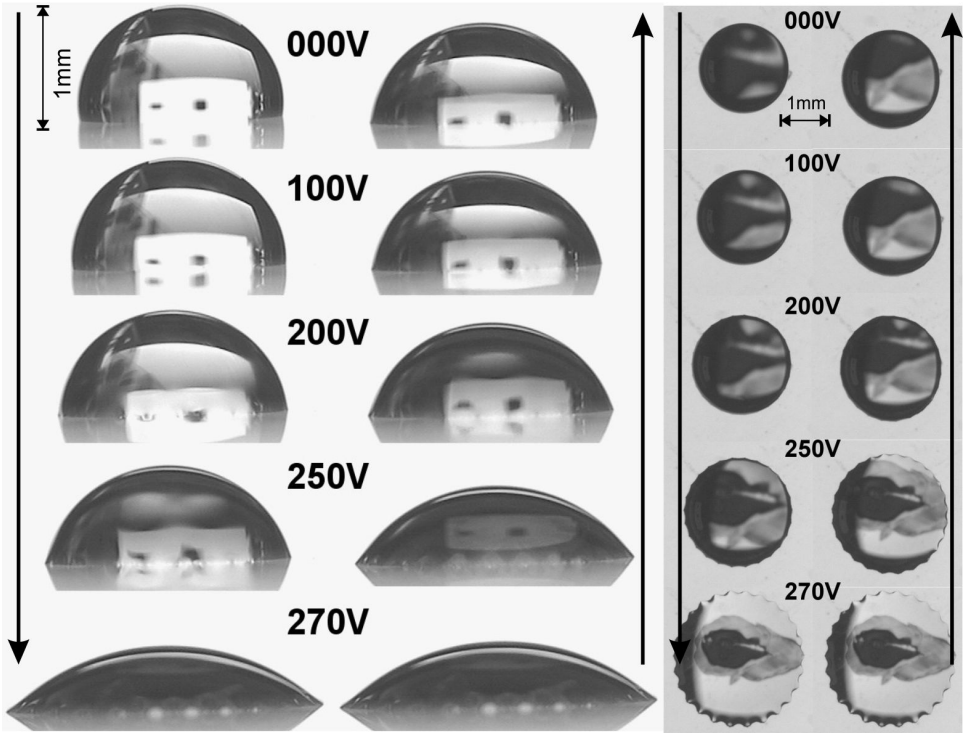

Figure 3.10: Images show that 1, 2 propylene glycol droplet wetting and dewetting on the hydrophobic 2μm SU8 layer on top of the radial electrodes when the voltage increased and subsequently decreased; (left side) perpendicular view and (right side) top view.

0V to 256V with delay of 30sec in between each step to allow the droplet to reach equilibrium state. An isotropic spreading was captured from the top and side view of the droplet as voltage was increased and then decreased as shown in figure 3.10. The contact angle of the 1, 2 propylene glycol reduces monotonically as a function of increasing voltage, and then steadily increases as a function of decreasing voltage as shown in figure 3.11. The quasistatic contact angle of the

1, 2 propylene glycol with applied voltage was obtained using the drop shape analysis software as described in section 2.5.2.

The initial contact angle of the droplet was 94^o at 0V, fell to 23^o as the voltage was increased to 256V, and then gradually the contact angle increased to 81^o as voltage decreased to zero voltage. The quasistatic change of the contact angle with applied voltage is shown in figure 3.11.

As the voltage increasing from 0V, the droplet was spread and confined in the region 1 (having a diameter of 3mm) at 97V. In figure 3.11, the first 10 data points of wetting show that the contact angle decrement where the droplet was being spread in region 1 and at 11th data it was confined in region 1 (having a diameter of 3mm). As the voltage increased from 106V, the three phase contact line was shifted from region 1 to region 2. Well the contact angle was decreased in similar manner and the droplet was bounded with an angle of 23^o in region 2 at 256V. A further application of higher voltage (at 280V), liquid fringes were extended from the droplet and is shown in figure 3.12.

The contact angle of the droplet was increased from 42^o to 81^o as voltage was decreased to no voltage due to restorative force generated by surface tension of the droplet.

The relation between the cosine of the contact angle and voltage square of the dielectrowetting on the radial electrodes is shown in the inset picture of the figure 3.11. The voltage square law for wetting was not obtained (equation 3.11) due to the electrode pitch variation in the geometry.

0 offset electrode geometry

The 0 offset electrode geometry is the other kind of the geometry to produce the isotropic liquid spreading using L-DEP. This geometry is similar to the interdigitated electrode array geometry where the electrode size is equal to the gap between the electrodes. The geometry consist the two electrode bones as shown in figure 3.9. A every each alternative electrode finger were circularly extended

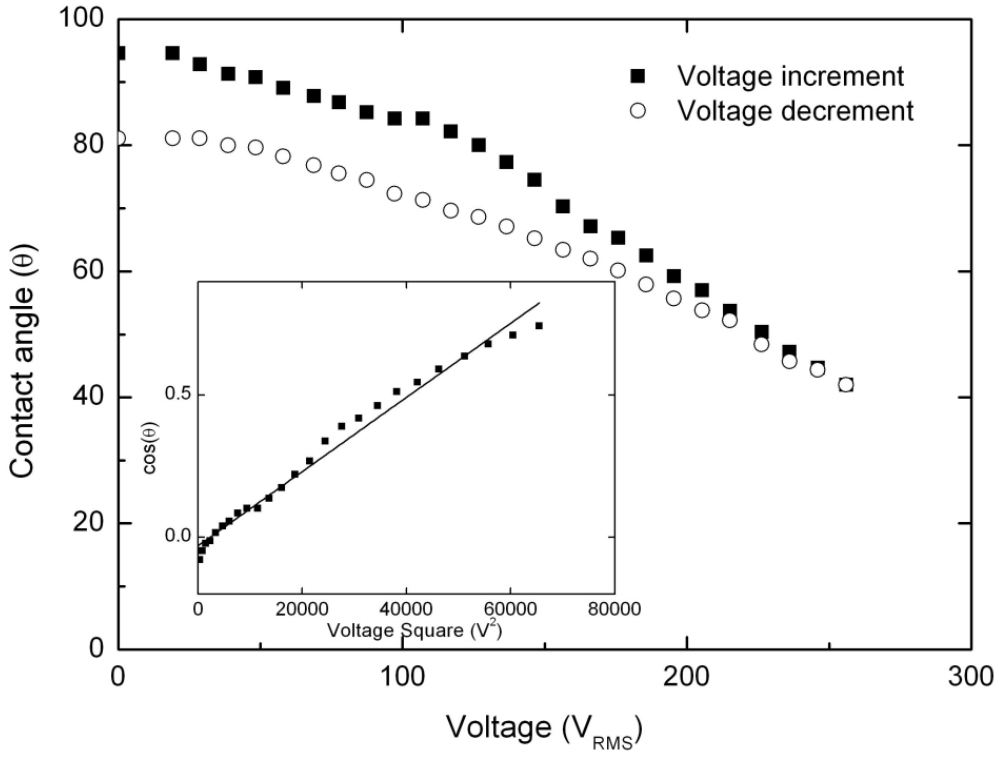

Figure 3.11: illustrates contact angle θ versus voltage V for 1, 2 propylene glycol on radial electrodes and the inner picture shows Cosθ versus voltage square (V^2) for 1, 2 propylene glycol on radial electrodes.

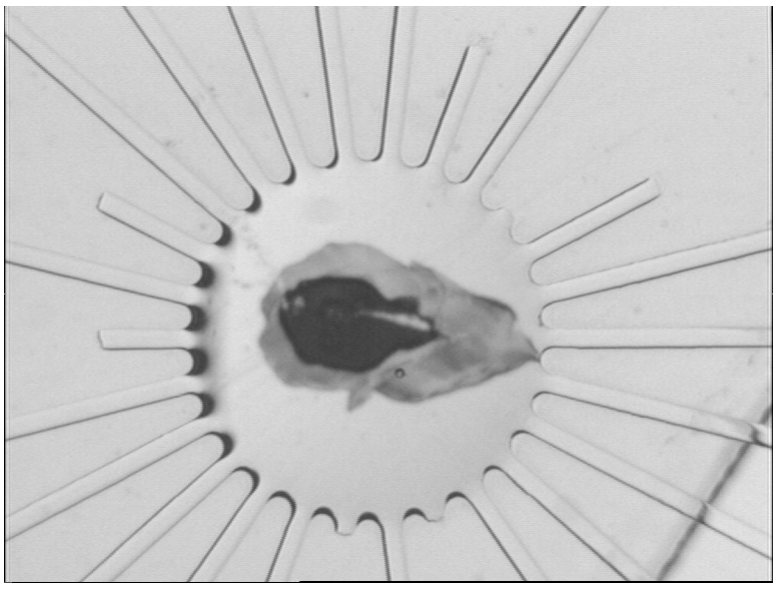

Figure 3.12: Figure shows the fringes are extending from droplet at 280V which was bounded in region 2.

from one of the electrode bone and interposed electrode fringes were extended from the other electrode bone. The width of the electrode is 40μm = gap between the electrodes. The 0 offset electrodes were fabricated using the standard photolithography as described in the section 2.2.1. The electrode array was coated with a SU8 layer having thickness of 1μm and was treated with Grainger solution as described in section 2.2.5.

A drop of the 1, 2 propylene glycol was dispensed on the centre of the electrode

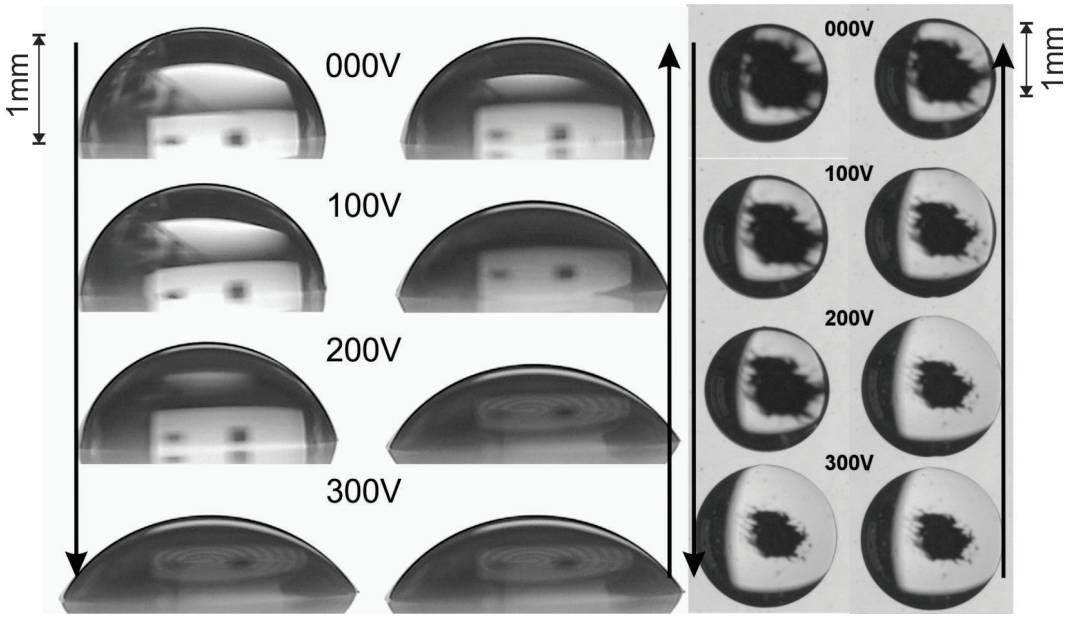

Figure 3.13: shows that 1, 2 propylene glycol droplet wetting and dewetting on the hydrophobic 2μm SU8 layer on top of the 0 offset electrodes when the voltage increased and subsequently decreased; (left side) perpendicular view and (right side) top view.

array having 40μm electrode width and volume was controlled using the Gilsen 0.1-2μl. Initial contact angle of the 1, 2 propylene glycol was 84^o. When a 10 kHz sine wave voltage was applied across the two electrode bones, which means the voltage is applied to each alternative electrode and interposed electrodes were earthed, the circular non-uniform electric field was created in the electrode device. The non-uniform electric field is periodic and pitch of the electric field is equal to double of the electrode pitch. The 10 kHz sine wave voltage was increased and decreased in steps of 10V from 0V to 300V with interval of 30sec for each voltage.

The quasistatic images of the drop were captured from the top and the side view of the drop (shown in Figure 3.13).

The droplet spreading in the interdigitated electrodes has shown no spreading

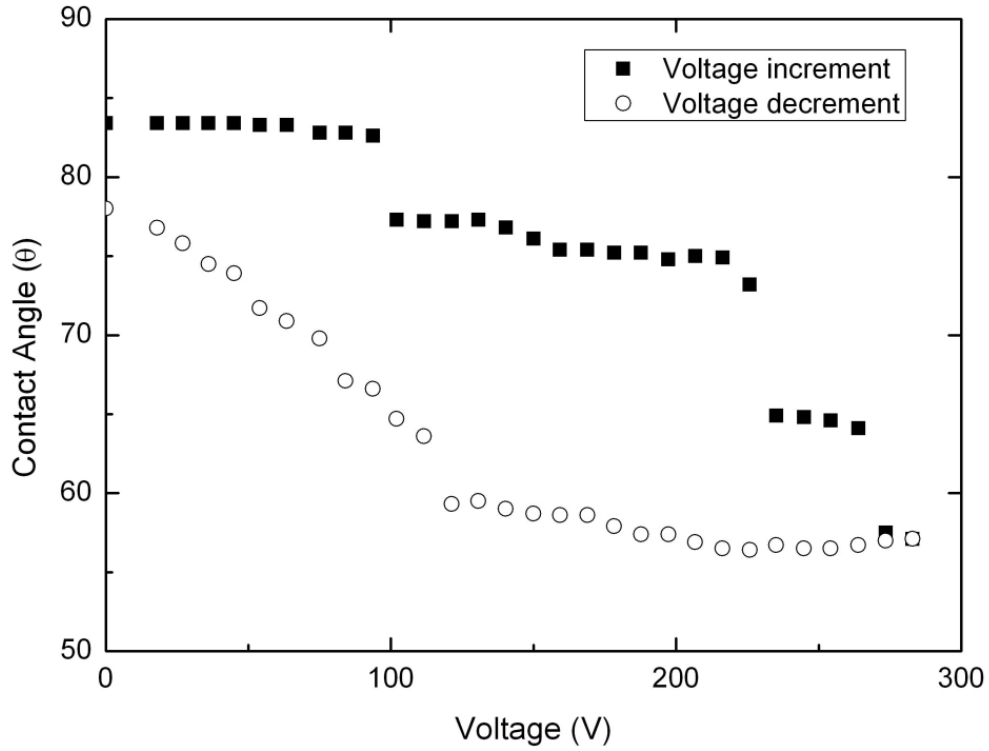

Figure 3.14: illustrates that contact angle of the drop as a function of voltage increment and decrement with a step of 10V.

across the electrodes due to the periodicity of the electric field and energy barriers. However, in the 0 offset electrode geometry the drop was not able to move across the energy barriers and in contrast the three phase contact line of the drop was moved along the electrode bones. Therefore the contact angle of the drop was decreased in quantized steps as shown in figure 3.14.

The initial contact angle of the droplet was 84^o at 0V, fell to 68^o as the voltage was increased to 300V, and then gradually the contact angle increased to 81^o as voltage decreased to zero voltage. The quasistatic change of the contact angle with applied voltage is shown in figure 3.14

The initial 10 data points in the voltage increment in the figure 3.14 were

Material	Dielectric constant	Refractive index
1, 2 propylene glycol	27.5	1.4324
Hexadecane	2.05	1.4345

Table 3.1: Liquid properties

where the drop was confined in the energy barrier, and then the drop moved through the electrode bone and was occupied in the preferential place and result of sudden change in the contact angle of the drop as shown in figure 3.14. The shift of the three phase contact line of the drop was measured using image J software, that is 80μm (which is equal to the electrode pitch). The step size of the shift was reduced as voltage increased and shown in figure 3.15.

3.7 Investigation of the liquid spreading in liquid media

So far an isotropic and anisotropic wetting and dewetting of 1, 2 propylene glycol droplet on circular and interdigitated electrode were shown in air medium with a hysteresis of around 10^o. In contrast new approach, preliminary experiments of liquid in liquid medium were performed on the interdigitated electrodes which were covered with a treated SU8 layer having thickness of 1um. B. Berge and S Kuiper have demonstrated the variable focus liquid lens with two non-miscible liquid using the electrowetting on dielectric (EWOD) [34, 41]. Our approach is purely based on the liquid dielectrophoresis. In this case the two liquids were non-miscible liquids, one is high polar liquid than the other liquid and two liquids are transparent. Liquid was hexadecane and the droplet was 1, 2 propylene glycol and the liquid properties were given in table 3.1.

Here we were used a 80μm line width IDT electrode array which is coated with a hydrophobic SU8 layer thickness of 1μm as previously mentioned. A well, $15mm^2$, was constructed on the electrodes array. Initially glass slides were cut in

to 15mm squares and then bottom edge of the glasses was glued with UV curable resin (Norland Ltd, USA) to the SU8 layer in four sides. The glue was cured in a 8 Watt UV light (T5 UV fluorescent tube, Philips Lighting, Netherlands) for 20mins. After 20mins the walls of the wells were strongly bonded to the SU 8 layer and also corners of the walls were glued to gather to prevent the leaks from corners while experimenting.

Figure 3.15: Image shows that shape of the 1, 2 propylene glycol droplet on the hydrophobic 1μm SU8 layer on top of the interdigitated electrodes in hexadecane oil at 0V, 200V and 0V.

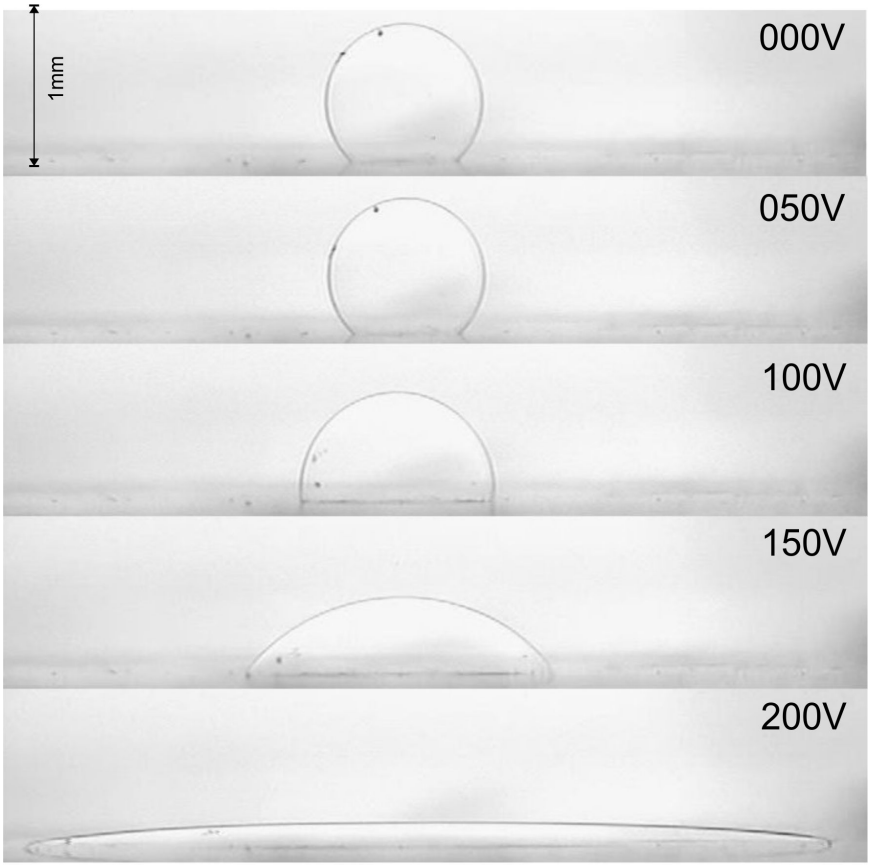

Figure 3.16: Image shows that a 1, 2 propylene glycol droplet wetting on the hydrophobic 1μm SU8 layer on top of the interdigitated electrodes in hexadecane oil when the voltage increased.

The device, 80μm electrode line width and well, was mounted in sample holder

in the same experimental setup which was used for dielectrowetting experimentation, and was connected to the voltage addressing unit. A droplet, 1μL, of 1, 2 propylene glycol was dispensed on centre of the electrode array and filled the well with hexadecane up to 6mm height of the well using Gilsen 2-10μL micro pipette. In mean while the droplet was monitored from the side view which is perpendicular to the electrode array. The boundary of the 1, 2 propylene glycol droplet was clear. A 10 kHz square wave was applied to each alternative electrode in the interdigitated electrode array and interposed electrodes were earthed hence a non-uniform electric field was created on the device. The droplet was experienced the L-DEP and resulting of the three phase contact line of the drop was moved towards the high gradient which means the contact angle of the drop also changed with respect to the applied voltage.

The initial contact angle of the 1, 2 propylene glycol droplet in hexadecane on the treated SU8 layer was 133.8^o at no voltage, which is different from the initial contact angle of the 1, 2 propylene glycol on the same surface but in air medium due to the density around the droplet. In order to check the hysteresis of the contact angle, the images of the droplet were taken at 0V, 200V and 0V from perpendicular to the electrode array. The contact angles are 133.8^o, 12^o and 133.8^o at 0V, 200V and 0V respectively. It has shown no hysteresis in the contact angle. Figure 3.15 showing the shape of the 1, 2 propylene glycol droplet at 0V, 200V and 0V.

In order to check the voltage square law, the voltage was increased from 0V to 200V in steps of 5V whilst quasistatic images were captured from the perpendicular view to the interdigitated electrode array. Figure 3.16 shows the change of the 1, 2 propylene glycol droplet shape as a function of applied voltage increasing. The contact angle was reduced as a function of the applied voltage. The contact angle of the droplet was determined using manual method such as finding the gradient of the line at the edge of the droplet using Image J software and shown in figure 3.17. The inset figure 3.17 shows the linear dependence

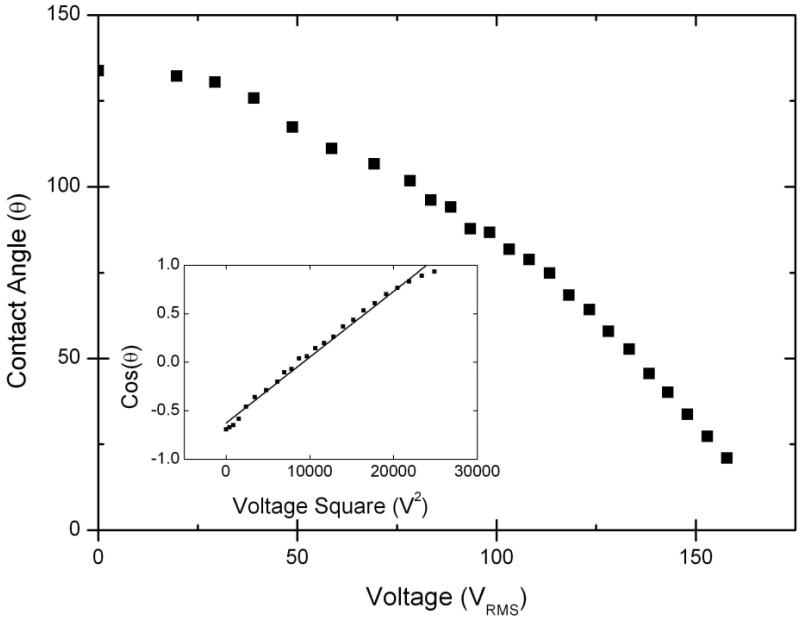

Figure 3.17: Illustrates contact angle of the droplet θ versus applied voltage for liquid in liquid medium on interdigitated electrodes and the inset picture shows cosθ versus voltage square.

of the cosine of the contact angle and voltage square which is similar to the dielectrowetting prediction.

An astonishing scene has been recorded during a wetting and dewetting of a liquid droplet in an another liquid such as the droplet is divided in to two droplets and then combined in to the single droplet in voltage controlled manner as shown in the figure 3.18. The contact angle of the 1, 2 propylene glycol droplet in hexadecane liquid at 0V was 138^o on the IDT electrode line width of 40μm (which is coated with a hydrophobised SU8 layer with thickness of 1μm).

The dielectrophoretic force, which was generated by applying a voltage to IDT array, was initiated the droplet spreading along the electrodes and then it was transformed in to a thin film at 240V. Usually when the voltage is switched off, then the droplet de-wets from the surface with a hysteresis of 0^o. But, in our case, the thin film is transposed to two small droplets. In first place when the voltage is removed, the three phase contact lines are very strongly pulled towards the centre due to the restorative force therefore at the centre of the film become

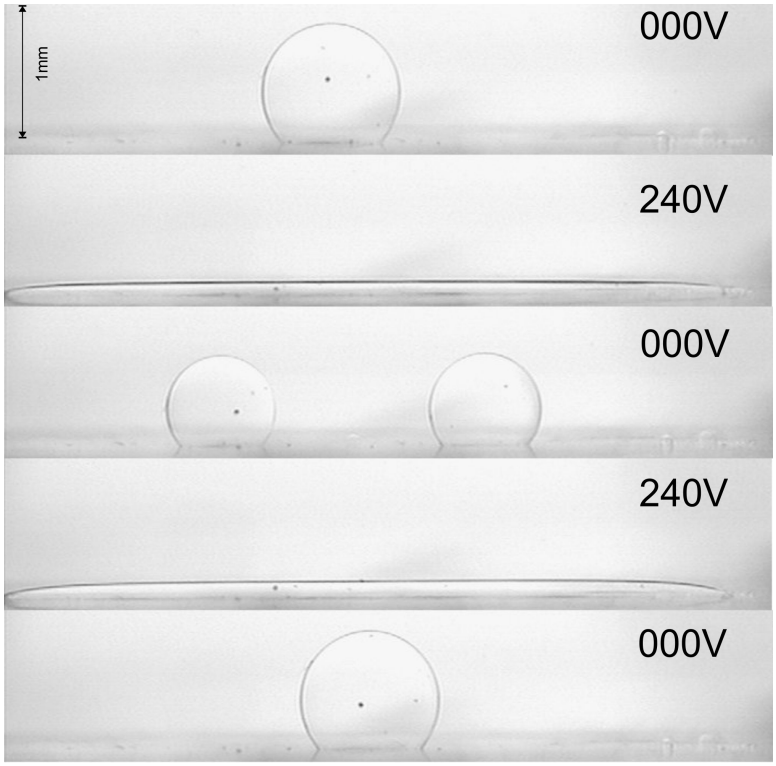

Figure 3.18: Figure shows, a single droplet at 0V, a thin film at 240V, formed in to two droplet after the voltage is switched off (at 0V), again a thin film at 240V and converted into a single droplet at 0V.

thinner then it broken. The two broken thin films were became two equal volume droplets after few msec. After the equal or slight higher voltage is applied to the device, then it again created a thin film where the two thin films were combined. The thin film is switched to a single droplet after the voltage is switched off.

De-wetting of the 1, 2 propylene glycol droplet in air has shown without transferring to the two drops even with the smaller drops. This fascinated results are need to explain in more scientific way by considering the densities and volume of the two droplets.

3.8 Conclusion

Dielectrowetting approach has shown the wetting and dewetting of the droplet on the solid surface in a voltage controlled manner whereby the shape and contact angle of the drop was changed according to the applied voltage. In this approach

the liquid can be conductive or non-conductive and is not necessary to be contact with the electrodes, and, this is the complementary to electrowetting. A non-uniform electric field was produced by the interdigitated, radial and 0 offset electrode geometries, which is essential in the dielectrowetting to drive the three phase contact line of the drop where the penetration depth is much smaller than the height of the drop. The liquid droplet is 1, 2 propylene glycol. The experimental results, an isotropic spreading, has proven the dielectrowetting prediction such as the linear dependence of the cosine of the contact angle of the drop and square of the applied voltage for wetting and dewetting of the drop with an offset of 6^o due to contact angle hysteresis on interdigitated electrodes. And also it has shown the strength of the dielectrowetting can be controlled by the pitch of the electrodes. The effect of the voltage loss due to the dielectric layer such as hydrophobic SU8 layer was considered.

An isotropic spreading was governed by the radial and 0 off set electrode geometry but it does not proved the dielectrowetting prediction. Nevertheless it has shown the wetting and dewetting of the drop with a hysteresis of 10^o and allowed a wide range of the contact angle difference up to 50^o which may have applications as a variable focus lens.

A preliminary experiments of the droplet spreading in a liquid has shown a wetting and a dewetting with a hysteresis of 0^o.

Chapter 4

Dynamics of dielectrowetting

4.1 Introduction

In briefly when a droplet is dispensed on a solid surface or liquid, it will rapidly adopt a spherical shape by balancing the three interfacial tensions force which due to surface tension and gravity. It has a dynamic contact angle which evolves with time until it reaches the equilibrium angle and obeys the Young's law at equilibrium [15, 16, 28, 29].

De-Gennes et al. demonstrated a simple view of spreading of a small droplet where the droplet size is less than the capillary length. The spreading is obtained due to the driving force given by the unbalanced surface tension, gravity and it resisted by viscous forces [28]. He has shown a simple power law between the dynamic contact angle and time i.e. $\theta \propto (t + t_o)^{-3/10}$ for axisymmetric spreading. A similar power law such as $r_c \propto (t + t_o)^{1/10}$ has been derived by Tanner's [14]. Using a PDMS oil on the silicon or glass substrate, these power laws has been investigated and the data has shown a good agreement with the theoretical prediction [14–16].

McHale et al. shown a stripe spreading power law with circular arc cross-section, $\theta \propto (t + t_o)^{2/7}$, and this phenomenon was observed using a PDMS oil on a glass substrate and on a lithium niobate substrate [82, 83]. They demonstrates a complete wetting to create a super-spreading by introducing the topographic effect [84]. The exponent in time goes from $3/10^{th}$ power law to a $3/4^{th}$ for the super-spreading of a droplet induced by roughness.

The rate of spreading can be controlled by topography and this control is defined by the surface design therefore it cannot easily be changed. Well the equilibrium contact angle can be controlled using the electrowetting on dielectric (EWOD) and in this case a conductive droplet is a contact with a conductive substrate (which is capped with an insulating layer). By applying a potential between the droplet and conductive substrate, a capacitive system is created and resulting of induced wetting. But we have used dielectrowetting, another method

to control the equilibrium contact angle. The dielectrowetting is demonstrated in previous chapter.

In chapter 3 the wetting and the dewetting of a small droplet of viscous liquid on an interdigitated electrode array with the liquid-dielectrophoresis has been demonstrated and has also shown the relationship between the contact angle of the droplet as a function of applied voltage [81]. In the same chapter the theoretical relationship between the cosine of the angle and voltage square is derived and demonstrated experimentally. This chapter demonstrates dynamics of the dielectrowetting of a droplet on the interdigitated electrode array having line width of 40μm, which is capped with a 0.85μm SU8 layer. In general, this chapter explains how the contact angle of the droplet behaves as a function of time at different voltages. Additionally this chapter illustrates super-spreading of the droplet without any additional surfactants in the liquid. Using a modified Hoffman-de Gennes law we predict three distinct spreading regimes such as (i) partial wetting regime: where the droplet exponentially approach to an equilibrium shape, (ii) complete wetting regime: spreading to complete wetting obeying a Tanner's law-type relationship, and (iii) super-spreading regime: towards a complete wetting film. We also demonstrates the quantitative agreement between the experimental results of the dielectrowetting (induced spreading of a 1, 2 propylene glycol droplet) and the theoretical predictions of the three distinct regimes.

4.2 Experimental set-up and Data capturing

An interdigitated (IDT) electrode array pattern is used in these experiments to characterize the dynamics of the three phase contact line movement of the droplet. The interdigitated electrode array, with an area of 5mm $\times$ 5mm, was fabricated using standard photolithography techniques (indium tin oxide (ITO) thickness of 25nm) on borosilicate glass. To increase the contact angle of the 1, 2 propylene glycol droplet on the SU8 layer, the SU8 layer was treated with a Granger solution

(Granger's Extreme Wash-in, Grangers International Ltd, Alfreton, Derbyshire, UK) consists of fluorocarbon emulsified in water with a detergent as described in section 3.2.

A modified experimental set-up of the dielectrowetting statics (chapter 3) was used to study the dynamics of the dielectrowetting. In this set-up the x-axis viewing camera (TK-C920U, security camera, JVC, Thor Labs, Ely, UK) was replaced by a high speed camera (Hotspot, NAC image technology, Devon, UK). During the dielectrowetting, a droplet of the 1, 2 propylene glycol was examined from the side view of the droplet (x-direction) using a high speed camera (Hotspot, NAC image technology, Devon, UK) fitted with a 10× objective lens and whist the droplet spreading along the electrode array was examined from the top view using a USB camera (DCC1645C, Thor Labs, Ely, UK) fitted with a 4× objective lens. The droplet spreading was recorded with 3000 frames per second at each voltage and then the video was converted to the avi format using the Hotspot software (Hotspot, NAC image technology, Devon, UK).

4.3 Experimental Results

Initially a drop (volumes used were in the range 0.08 ± 0.01 μL) of 1, 2 propylene glycol (dielectric constant = 27.5, surface tension = $45.6 mN m^{-1}$) was dispensed at the center of the IDT electrode array (line width = 40μm) which is coated with a hydrophobic SU8 layer having a thickness of 0.85μm and the device was placed in the experimental setup. A 10kHz sine wave (270V) was applied to each alternative electrode and the interposed electrodes were earthed which results in a non-uniform electric field. This non uniform electric field exponentially decayed with a penetration depth into the liquid. The three phase contact line of the droplet was moved along the electrode array in the x-direction as a function time, in other words the contact angle of the drop was reduced as a function of time until it reaches equilibrium contact angle at fixed voltage. The time depen-

dent droplet images were recorded viewing from the y-direction during droplet spreading. Voltage step of 10V step in between 40V and 270V were used and back to 0V between steps.

The time dependent data of the droplet that includes the contact angle, width, and height of the droplet were extracted from the images of the droplet by image processing and using the automated Drop Shape Analysis (DSA) software. At the beginning the time dependent droplet spreading was imported into the DSA software and a baseline was defined manually (and this did not change for a sequence of images at a given voltage). In DSA software, video calculation function was used to measure the contact angle of the droplet by fitting the circular arc to the image in sequence. The extracted contact angle values were used in figure 4.1 from the height and width of the arc using standard trigonometry. At the above 200V, the fitting was done for shorter times due to the droplet profile (which were not well described by the circular arc method).

The 2D actual droplet profile was extracted by image processing. To begin with the contrast of the droplet images were enhanced using Image J software and then a macro program was written to extract the edge profile in x-z direction. Then a bespoke MatLab programme was used to obtain the values of the width and the height of the droplet as a function of time. We acknowledge Dr David Fairhurst for the MatLab program which was used to extract the droplet profiles and the width of the time dependent droplet.

The time dependent contact angle at 10V step from 140V to 270V is shown in figure 4.1. It shows the θ was reduced until it reaches to the equilibrium contact angle for limited voltage (for example below 200V).

Figure 4.2 shows the side view images of the evolution of the equilibrium droplet profiles at the higher voltages (200V to 270V in step of 10V) which were contrast enhanced to make the edge profile distinct. The symmetric and uniform shift of the three phase contact line was obtained with respect to the applied voltage. The fixed frame size, where the vertical scale was expanded by a factor

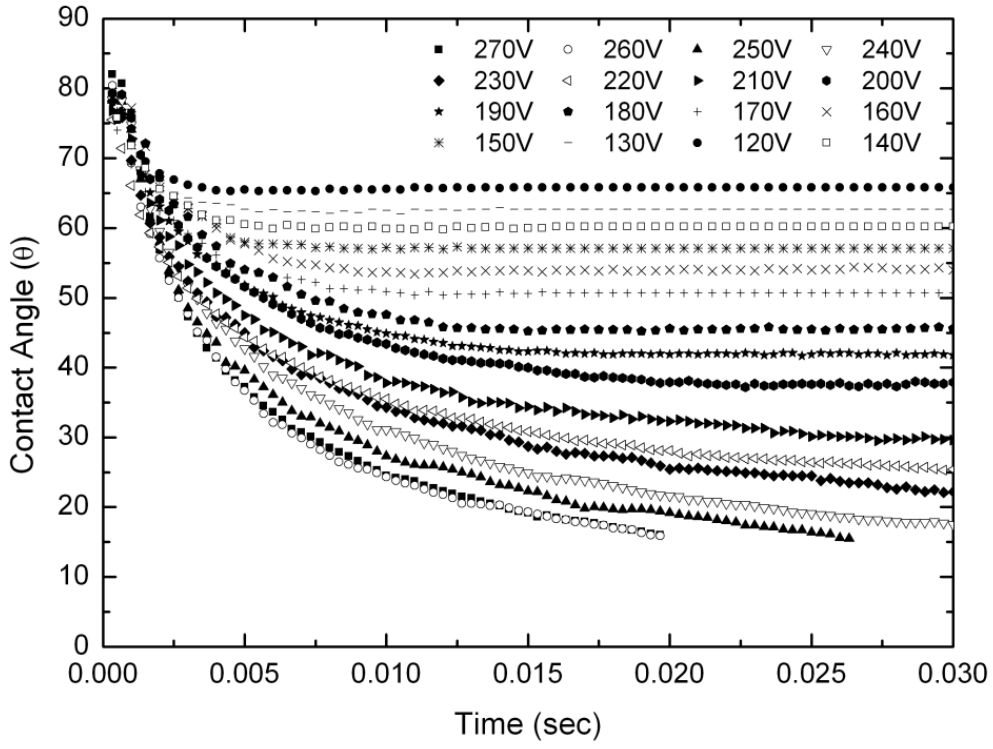

Figure 4.1: Graph showing the contact angle of the droplet as a function of time and applied voltage.

of 2 compared to the horizontal size, was used to distinguish the partial wetting and more complete wetting. A film spread can be seen clearly at 270V.

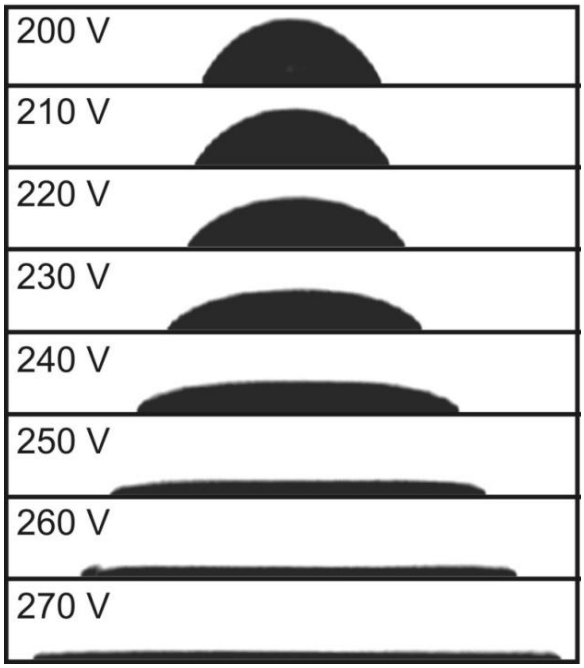

Figure 4.2: The 2D profiles of the droplet at the equilibrium state for each voltage.

Due to the periodic barrier energy presented by the electrode stripe the droplet was forced to move along the electrode array resulting in the droplet width in y-direction unchanged as shown figure 4.3. The x-y plane (top) and x-z plane (side view) of the droplet is shown in the figure 4.3 inset.

The equilibrium contact angles were measured using the circular fitting method in the DSA software for voltages between 40V and 210V. An exception applied to the equilibrium contact angle values were obtained for voltages between 210V to 245V due to the circular fitting was not well defined hence the angles were calculated manually from the gradient at the advancing edge of the droplet. At 250V to 270V, the equilibrium state of the oil droplet is complete wetting (thin film), therefore we have not measured the dynamic equilibrium contact angle.

The evolution of the equilibrium contact angle of the 1,2 propylene glycol droplet at different voltages (between 40 and 245V in steps of 10V) is shown in the figure 4.3 and the solid line is obtained by fitting the dielectrowetting equation

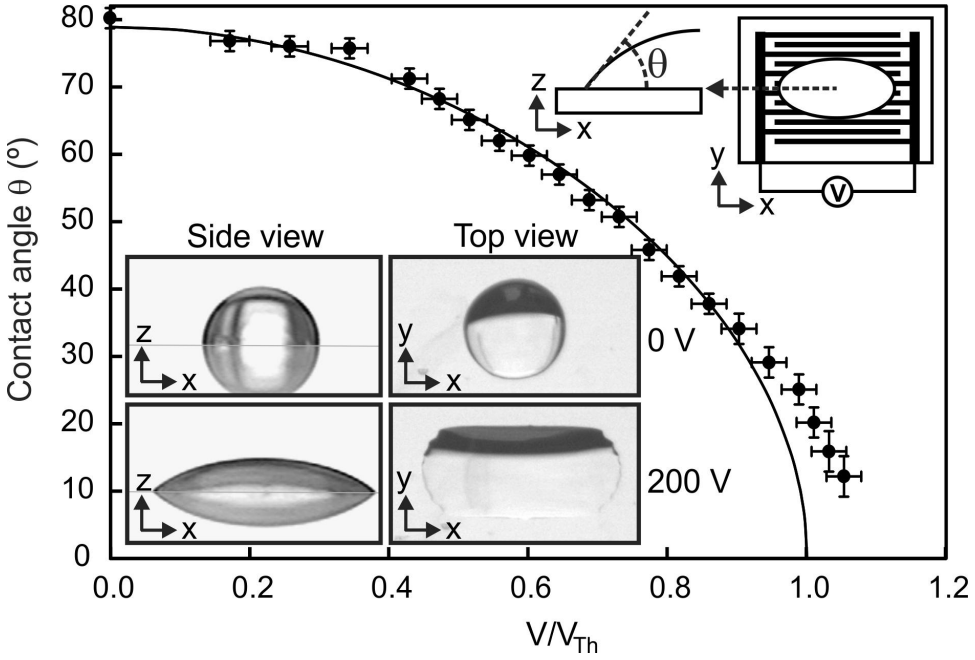

Figure 4.3: The graph shows the equilibrium contact angle of the 1, 2 propylene glycol droplet on the 40μm line width electrode array at different voltages and the solid line is obtained from fit to equation 4.1, modified dielectrowetting equation. The inset picture shows the droplet spreading along the electrode array.

4.1 [81] to the data below threshold voltage.

$$cos\theta_{eq} = cos\theta_y + \alpha V^2 \tag{4.1}$$

where θ_y is Young's equilibrium contact angle, θ_{eq} is an equilibrium contact angle when voltage was applied to the electrodes and $\alpha = \frac{\varepsilon_o(\varepsilon_r - 1)}{2\delta\gamma_{LV}}$. The complete wetting is predicted at the threshold voltage where cosθ_{eq} is 1 and V = V_{Th}. For this experiments V_{Th} is 230±2V.

The modified Hoffman-de-Gennes law is used to predict the three distinct spreading regimes

(i) when the applied voltage is below the threshold voltage (V < V_{Th}) i.e partial wetting. The contact angle exponentially approaches to the equilibrium.

(ii) when the applied voltage is equal to the threshold voltage (V = V_{Th}) i.e complete wetting. At completing the contact angle follows a Tanner's law type i.e. $\theta \propto (t + t_o)^{-2/7}$.

(iii) When the applied voltage is above the threshold voltage (V > V_{Th}) i.e super spreading. The contact angle follows a power law i.e. $\theta \propto (t + t_o)^{-2/3}$.

4.4 Model for spreading

4.4.1 Modified dielectrowetting equation

Figure 4.4 shows an oil droplet on the centre of the interdigitated electrode array which is coated with an insulating layer. When a voltage is applied across the electrode array, it creates a nonuniform electric field in the liquid. Dielectric force move the contacted line by distance Δx, giving an increase in contact area ΔA = $L_o \Delta x$. The solid-vapor interface is replaced by the solid-liquid interface with area ΔA, and in addition the surface area of the liquid-vapor interface is increased by ΔAcosθ resulting in a surface free energy increase of γ_{LV} ΔA $cos(\theta)$ [9, 81, 85].

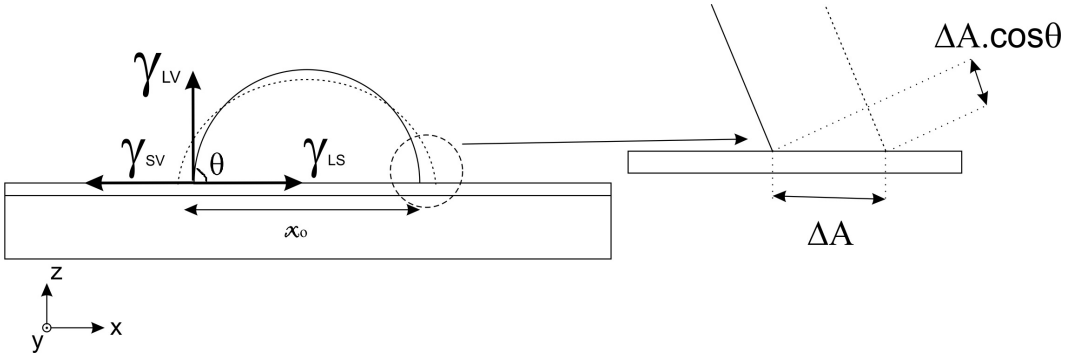

Figure 4.4: Schematic representation of the drop on the interdigitated electrodes (dielectrowetting).

$$\Delta F = \Delta A cos(\theta_{eq})\gamma_{LV} + \Delta A(\gamma_{LS} - \gamma_{SV}) - \alpha \Delta A V_o^2 \tag{4.2}$$

Where ΔF is the change in free energy, α is the dielectrowetting energy ($\frac{\varepsilon_o(\varepsilon_l - 1)}{2\delta\gamma_{LV}}$) from chapter 3.

$$\frac{\Delta F}{\Delta A} = cos(\theta_{eq})\gamma_{LV} + (\gamma_{LS} - \gamma_{SV}) - \alpha V_o^2 \tag{4.3}$$

At equilibrium, $\frac{\Delta F}{\Delta A} = 0$ and since $\cos\theta_y = \frac{\gamma_{LS} - \gamma_{SV}}{\gamma_{LV}}$ (Young's equation).

Therefore,

$$cos\theta_{eq} = cos\theta_y + \alpha V^2 \tag{4.4}$$

α can be replaced by an experimentally determined threshold voltage. At the threshold voltage, the droplet tends to complete forced wetting which includes a vanishing contact angle, cosθ_{eq}=1.

$$1 = cos\theta_y + \alpha V_{Th}^2 \tag{4.5}$$

$\Rightarrow$

$$\alpha = \frac{1 - cos\theta_y}{V_{Th}^2} \tag{4.6}$$

Thus the equation 4.4 (dielectrowetting equation) is rewritten in terms of threshold voltage.

$$cos\theta_{eq} = cos\theta_y + (1 - cos\theta_y)\left(\frac{V}{V_{Th}}\right)^2 \tag{4.7}$$

and the energy change accompanying a displacement of the contact line, replaces eq 4.7 to eq 4.2 we get.

$$\Delta F \approx -\Delta A \gamma_{LV}\left[(cos\theta_y - cos\theta_{eq}) + (1 - cos\theta_y)\left(\frac{V}{V_{Th}}\right)^2\right] \tag{4.8}$$

The rate of change of the energy per unit length of the contact line is due to the unbalanced interfacial tensions and the energy contribution from the electric field, since $\Delta A = y\Delta x$:

$$\frac{d(\Delta F)}{dt} \approx -\gamma_{LV} v_E(t)\left[(cos\theta_y - cos\theta_{eq}) + (1 - cos\theta_y)\left(\frac{V}{V_{Th}}\right)^2\right] \tag{4.9}$$

where, v_E(t) = $\Delta x/\Delta t$ is the velocity of the three phase contact line of the droplet and the time dependencies have been shown explicitly. The viscous dissipation of energy per unit length of the contact line is given in the de Gennes approach

[28, 82, 86–89]

$$D_{visc} \propto \eta v_E^2(t)/\theta \tag{4.10}$$

Where η is the viscosity of the liquid. Equating the rate of change in energy 4.9 to the viscous dissipation 4.10 gives,

$$v_E(t) \approx k \left(\frac{\gamma_{LV}}{\eta}\right) \theta(t) \left[(cos\theta_y - cos\theta) + (1 - cos\theta_y) \left(\frac{V}{V_{Th}}\right)^2\right] \tag{4.11}$$

Where, k is an overall constant. The equation 4.11 is the electric field extended Hoffman-de Gennes equation for the relationship between the contact angle and velocity of the three phase contact line.

Equation 4.11 predicts three distinct regimes according to the applied voltage; partial wetting at V $< V_{Th}$, complete wetting at V $= V_{Th}$ and super-spreading at V $> V_{Th}$.

Velocity of three phase contact line in partial wetting regime ($V \ll V_{Th}$)

In the partial wetting case, as the voltage increases the wetting increases by a small area and $\theta_{eq} > 0^o$.

The velocity of three phase contact line is rewritten as equation 4.12 by substituting the equation 4.7 in the equation 4.11.

$$v_E(t) \approx k \left(\frac{\gamma_{LV}}{\eta}\right) \theta(t)(cos\theta_{eq} - cos\theta) \tag{4.12}$$

$$\Delta\theta = \theta - \theta_{eq} \tag{4.13}$$

$$\theta = \Delta\theta + \theta_{eq} \tag{4.14}$$

Substituting the θ in equation 4.12.

$$v_E \approx k\left(\frac{\gamma_{LV}}{\eta}\right)(\Delta\theta + \theta_{eq})(cos\theta_{eq} - cos(\Delta\theta + \theta_{eq})) \tag{4.15}$$

Therefore,

$$v_E \approx k\left(\frac{\gamma_{LV}}{\eta}\right)(\Delta\theta + \theta_{eq})(cos\theta_{eq} - cos\Delta\theta.cos\theta_{eq} + sin\Delta\theta.sin\theta_{eq}) \tag{4.16}$$

and after expansion this gives,

$$v_E \approx k\left(\frac{\gamma_{LV}}{\eta}\right)(\Delta\theta + \theta_{eq})(\frac{\Delta\theta^2}{2} + \Delta\theta.\theta_{eq}) \tag{4.17}$$

The three phase contact line velocity (edge speed) of the droplet is,

$$v_E(t) \approx k\left(\frac{\gamma_{LV}}{\eta}\right)\theta_{eq}^2\Delta\theta(t) \tag{4.18}$$

where $\Delta\theta(t)$=$\theta(t) - \theta_{eq}$. This predicts an exponential approach to the equilibrium contact angle which is determined by voltage for a small stripe of liquid.

Velocity of three phase contact line in complete wetting regime ($V \sim V_{Th}$)

In the complete wetting regime ($V \sim V_{Th}$), the contact angle vanishes $\theta_{eq} \simeq 0$.

Therefore, the edge velocity of a droplet is,

$$v_E \approx k\left(\frac{\gamma_{LV}}{\eta}\right)\theta(1 - cos\theta) \tag{4.19}$$

and assuming the dynamic contact angle is small this gives,

$$v_E \approx k\left(\frac{\gamma_{LV}}{\eta}\right)\theta(1 - 1 + \frac{\theta^2}{2}) \tag{4.20}$$

$$v_E(t) \approx k \left(\frac{\gamma_{LV}}{\eta} \right) \theta^3(t) \tag{4.21}$$

For a complete wetting regime, the Hoffman law ($v_E \propto \theta^3$) is obtained.

Velocity of three phase contact line in complete wetting regime ($V \gg V_{Th}$)

In the above threshold voltage, super-spreading regime, the edge speed becomes directly proportional to the dynamic contact angle and is given by,

$$v_E(t) \approx k \left(\frac{\gamma_{LV}}{\eta} \right) \theta(t)(1 - cos\theta_y) \left(\frac{V}{V_{Th}} \right)^2 \tag{4.22}$$

4.4.2 Dynamics: Stripes of liquids

We consider a stripe of liquid with constant volume, Ω, length of the stripe, L_o, and circular arc cross-section to obtain the relationship of the contact angle variation in time. The assumption is that spreading modifies the contact angle of the drop, in other words the spreading alters the circular arc, and the contact width of the droplet on the substrate ($2x_o$). The width of the stripe on the substrate is given in [82] by;

$$x_o(t) = \left(\frac{\Omega}{L_o} \right)^{1/2} \frac{sin\theta}{(\theta - sin\theta cos\theta)^{1/2}} \tag{4.23}$$

The edge speed of the contact line is then,

$$v_E(t) = \frac{dx_o}{dt} = \left(\frac{\Omega}{L_o} \right)^{1/2} \frac{\theta cos\theta - sin\theta}{(\theta - sin\theta cos\theta)^{3/2}} \frac{d\theta}{dt} \tag{4.24}$$

$$v_E(t) = -\left(\frac{3\Omega}{8L_o} \right)^{1/2} \frac{1}{\theta^{3/2}} \frac{\theta cos\theta - sin\theta}{(\theta - sin\theta cos\theta)^{3/2}} \frac{d\theta}{dt} \tag{4.25}$$

Thus, the electric field extended form of the Hoffman-de Gennes law (equating equation 4.11 and equation 4.25) for a circular arc cross-section stripe of constant volume is,

$$\frac{d\theta}{dt} \approx -k\left(\frac{\gamma_{LV}}{\eta}\right)\left(\frac{8L_o}{3\Omega}\right)^{1/2}\theta^{5/2}\frac{\theta cos\theta - sin\theta}{(\theta - sin\theta cos\theta)^{3/2}}\left[(cos\theta_y - cos\theta) + (1 - cos\theta_y)\left(\frac{V}{V_{Th}}\right)^2\right] \tag{4.26}$$

and assuming the dynamic contact angle is small this gives,

$$\frac{d\theta}{dt} \approx -k\left(\frac{\gamma_{LV}}{\eta}\right)\left(\frac{8L_o}{3\Omega}\right)^{1/2}\theta^{5/2}\left[1 - \frac{\theta^2}{5} + \frac{\theta^4}{50} + ...\right]\left[(cos\theta_y - cos\theta) + (1 - cos\theta_y)\left(\frac{V}{V_{Th}}\right)^2\right] \tag{4.27}$$

or to first order in the pre-factor,

$$\frac{d\theta}{dt} \approx -\lambda\theta^{5/2}\left[(cos\theta_y - cos\theta) + (1 - cos\theta_y)\left(\frac{V}{V_{Th}}\right)^2\right] \tag{4.28}$$

where $\lambda = \left(\frac{\gamma_{LV}}{\eta}\right)\left(\frac{8L_o}{3\Omega}\right)^{1/2}$. The assumption that the pre-factor can be expanded is numerically reasonable for contact angles below around 60^o because the series only involves even powers.

4.5 Partial Wetting ($V < V_{TH}$)

As previously described the forced partial wetting of a 1, 2 propylene glycol was obtained when the applied voltage to the interdigitated electrode array is below the threshold voltage and in this case the equilibrium contact angle is much higher than the zero ($\theta \gg 0^o$). This type of liquid has been widely used in the dielectrowetting since it has high dielectric constant. Here the threshold voltage (V_{th}) is 230V ± 2V. The edge speed of the droplet can be controlled with voltage.

Figure 4.5.b shows the actual droplet from y-direction at times of 0sec, 1msec, 3 msec, 10msec, 30msec, 55msec, 80msec and 150msec after a constant a 10kHz

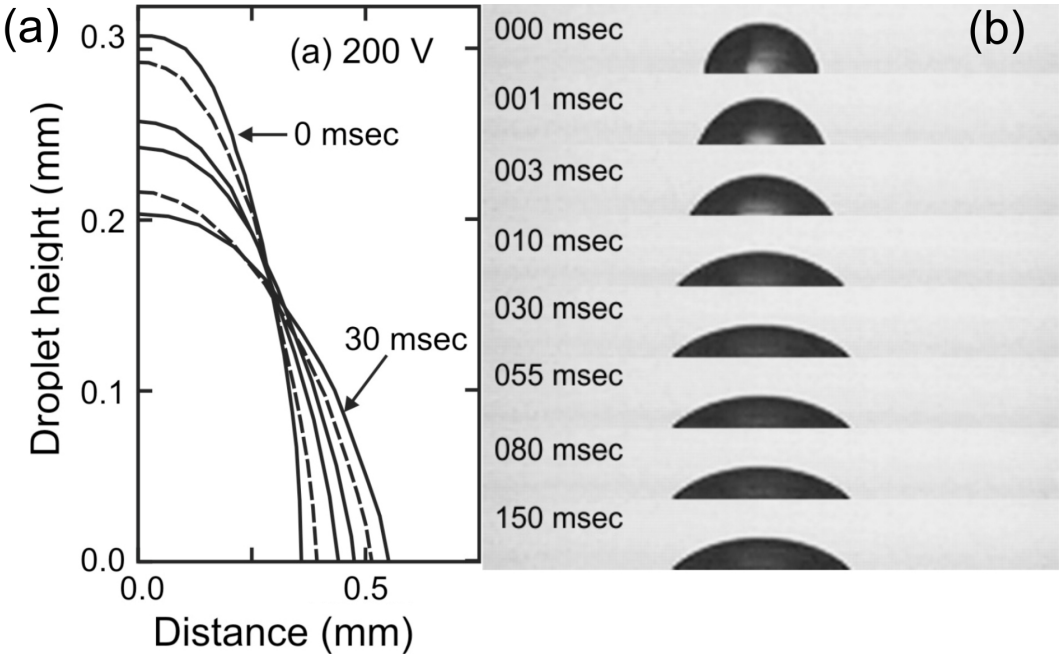

Figure 4.5: Figure (b) shows the 2D actual droplet spreading as a function of time in y-direction at 200V and figure (a) the digitised profiles of the droplet at times 0, 1ms, 3ms, 5ms 10ms and 30ms.

sine wave 200V (just below the threshold voltage, V/V_{Th}=0.87) is applied to the electrode array and figure 4.5.a shows digitised drop shape profile as a function of time at times of 0sec, 1msec, 3 msec, 10msec and 30msec. No further spreading along the electrode array was obtained after 30msec at a fixed voltage of 200V. The width of the deposited droplet was 0.72mm at 0V and spread to 1.1mm value over a period of typically 30msec at 200V and the contact angle was decreased from the 79.3^o to 37.7^o over a period of 30msec. The digitised profiles, contact angle and width of the droplet are extracted by image processing as described in section 4.3.

4.5.1 Exponential approach to equilibrium contact angle

The contact angle will tend to the constant value $\theta_{eq} > 0$ as time tends to infinity where:

$$cos\theta(t) \rightarrow cos\theta_{eq} = cos\theta_y + (1 - cos\theta_y)\left(\frac{V}{V_{Th}}\right)^2 \tag{4.29}$$

re-write equation 4.28 assuming that both θ and θ_e are both small, giving

$$\frac{d\theta}{dt} \approx -\frac{\lambda}{2}(\theta^2 - \theta_{eq}^2)\theta^{5/2} \tag{4.30}$$

The substitution $\Delta\theta = \theta - \theta_{eq}$ and assuming that $\Delta\theta$ is also small, gives,

$$\frac{d\Delta\theta}{dt} \approx -\lambda\Delta\theta.\theta_{eq}^{7/2} \tag{4.31}$$

This integrates to give an exponential approach to equilibrium,

$$\Delta\theta \approx \Delta\theta_o exp(-\lambda\Delta\theta.\theta_{eq}^{7/2}t) \tag{4.32}$$

Where $\Delta\theta_o = \theta(t = 0) - \theta_{eq}$ is the constant of integration.

Re-writing the above equation, the dynamic contact angle is predicted to be exponential to reach the equilibrium contact angle, i.e

$$\Delta\theta(t) = \Delta\theta_o exp[-t/\tau(V)] \tag{4.33}$$

Where $\tau^{-1} = k(\gamma_{LV}/\eta)(8L_o/3\Omega)^{1/2}\theta_{eq}^{7/2}(V)$

The contact angles of the droplet were measured as a function of time at fixed voltages using the automated DSA software (circular arc fits are well defined at each voltage). Data for the partial wetting with applied voltage at 10V interval between 100V and 200V are shown in figure 4.6 and thus voltages are below the threshold voltage (V_{Th}=230V). To test the exponential approach prediction we performed a best straight line fit on $ln(\Delta\theta)$ against time with applied voltage (between 100V to 200V) for each experimental data. The time dependencies given by this linear regression fits are shown in figure 4.6. For clarity we offset the data to pass through the origin by adjusting the equilibrium contact angle, i.e $ln[\theta_{eq} - \theta_y]$.

The linear regression fit to the experimental data's (solid lines) corresponds

to the functional form of $ln(\delta\theta) = (-1/\tau)t + ln(\delta\theta_o)$. From this linear fitting for each voltage the values of gradient (m=$1/\tau$) were extracted. A small difference between the actual data and fits could be seen during the late stage of spreading at each voltage. The time dependencies given by this linear regression fits are shown in figure 4.6. For clarity we offset the data to pass through the origin by adjusting the equilibrium contact angle, i.e $ln[\theta_{eq} - \theta(Vt = 0)]$.

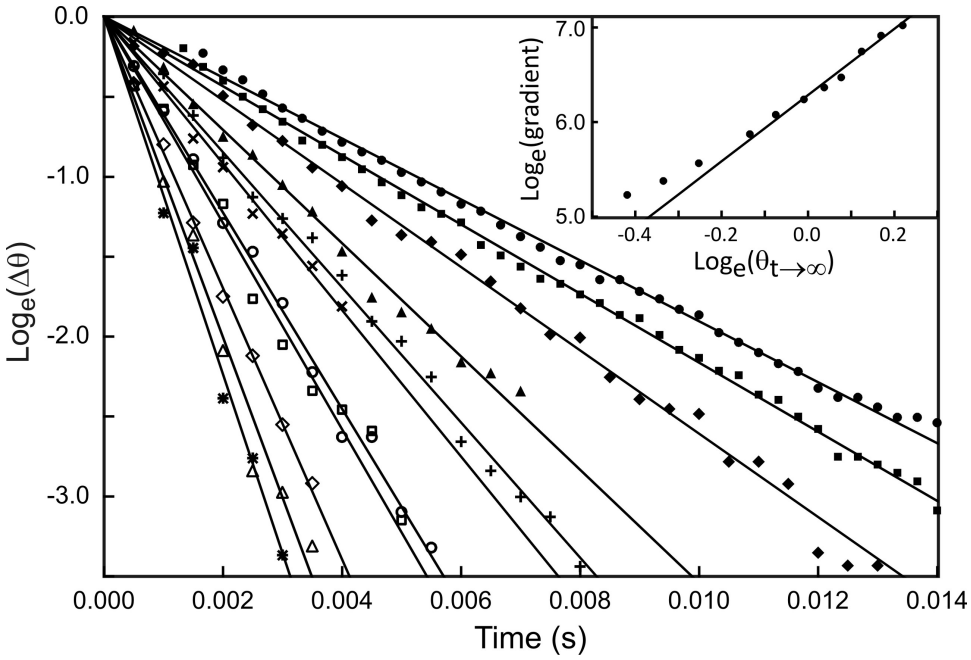

Figure 4.6: Data in the graph shows the exponential approach to equilibrium of spreading stripes for applied voltages as a function of time. Inset figure shows the predicted dependence for the time constant in the exponential approach to equilibrium.

According to the partial wetting prediction (equation 4.33), the slopes should be reduced as the applied voltage increases. The experimental data has shown the slope of the linear fit reduced as the voltage is increased and the wetting is increased with voltage. In figure 4.6 the linear fits between the $ln(\Delta\theta)$ and the time demonstrated that the contact angle is exponentially approaches the equilibrium contact angle as predicted by the equation 4.33.

To test whether the time constant follows a $\theta_{eq}^{-7/2}$ power law as predicted by equation 4.33, the natural logarithmic of the gradient of linear fits against the natural logarithmic equilibrium contact angle is plotted (shown in the inset figure

4.6). The solid line in the inset figure is the theoretical approximation ($\ln(1/\tau)$ vs $ln(\theta_e)$) and it has slope of 7/2. The initial three data points of 200V, 190V and 180V are away from the theoretical trend line because the wetting is becoming stronger as the voltage reaches to the threshold voltage. These experimental data has shown very good agreement with theoretical exponential approach prediction (4.32) for the partial wetting case ($V < V_{Th}$).

4.5.2 Exponential approach to equilibrium contact width

To lowest order in theta the approximation of the dynamics of the stripe width with time in equation 4.25, can be written

$$v_E(t) = -\left(\frac{3\Omega}{8L_o}\right)^{1/2} \frac{1}{\theta^{3/2}} \frac{d\theta}{dt} \tag{4.34}$$

Where v_E is the rate of change with time of the stripe half-width.

$$\frac{dx_o(t)}{dt} = -\left(\frac{3\Omega}{8L_o}\right)^{1/2} \frac{1}{\theta^{3/2}} \frac{d\theta}{dt} \tag{4.35}$$

Using equation 4.32, gives

$$\Delta x(t) = -\left(\frac{3\Omega}{8L_o}\right)^{1/2} \frac{\Delta\theta_o}{\theta^{3/2}} exp(-\lambda\theta_e^{7/2}t) \tag{4.36}$$

This approach shows the contact width exponentially approaches the equilibrium contact width as the contact angle also approaches equilibrium.

The time dependent contact width of the droplet was extracted using the bespoke Matlab programme for each fixed voltage from 110V to 200V with a step of 10V. A straight line fit (linear regression fit) was performed between the $ln(\Delta x)$ and time to extract the gradient of the fit. Figure 4.7 shows the time dependence given by the linear regression fits. For clarity we offset the data to pass through the origin by adjusting the equilibrium contact width.

The slope of the linear fit is reduced as the voltage is increased because wetting

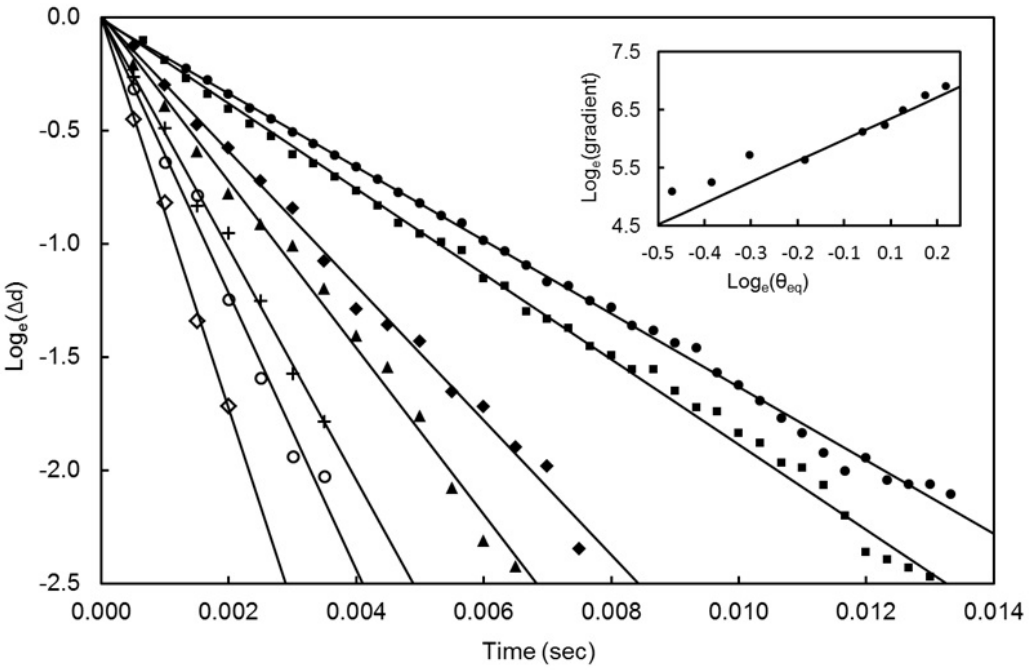

Figure 4.7: Graph showing the contact width of the droplet exponentially approach to equilibrium for applied voltage ($V \ll V_{Th}$).

becomes stronger with voltage. A deviation between the actual data and straight line fits could be seen during final stage of spreading at each voltage. These experimental data have shown good agreement with theoretical prediction (such as exponential approach) equation 4.36 for partial wetting case.

To test whether the time constant follows a $\theta_{eq}^{-7/2}$ power law as predicted by equation 4.36, the natural logarithmic of the gradient of linear fits against the natural logarithmic equilibrium contact angle is plotted (shown in the inset figure 4.7). The solid line in the inset figure is the theoretical approximation (ln(slope of the equation 4.36) vs $ln(\theta_e)$) and it has slope of 7/2. The initial three data points of 200V, 190V and 180V are away from the theoretical trend line because the wetting is becoming stronger as the voltage reaches to the threshold voltage. These experimental data has shown very good agreement with theoretical exponential approach prediction (4.36) for the partial wetting case ($V < V_{Th}$).

4.6 Complete Wetting and Super Spreading ($V \simeq V_{TH}$ and $V > V_{TH}$)

To test the spreading power law for complete wetting regime to super-spreading regime, the 1, 2 propylene glycol droplet is dispensed on the interdigitated electrode array line width of 40μm (which is coated with 0.85μm hydrophobic SU8 layer) and voltage is applied to the electrode array. By applying a voltage across the electrode array we can control the characteristic edge speed and thus adjust the time scale for spreading.

Figure 4.8.(a) and (b) show the actual 2D droplet in the y-direction at times of 0sec, 1msec, 3 msec, 10msec, 30msec, 55msec, 80msec and 150msec after a constant a 10kHz sine wave at 240V (just above the threshold voltage V/V_{Th}=1.04) and 270V (above the threshold voltage V/V_{Th}=1.17) respectively is applied to the electrode array. Figure 4.8.(c) and (d) show digitised drop shape profiles at times 0, 1 ms (dashed), 3 ms, 5 ms, 10 ms (dashed), 30 ms, 50 ms, 100 ms (dashed) and 300 ms..

The time dependent contact angle and width of the droplet were extracted by image processing as described in section 4.3. As the voltage is increased the wetting behaviour becomes stronger and the switching speed is increased. The circular arc method is used to measure the contact angle of the droplet but it was restricted to the time after the onset of spreading due to the switching speed increased at the high voltages. For example for times up to 26.3msec for 240V and for times up to 17.7msec for 270V where in both cases the contact angle is $\sim 20^o$. We observed a film type cross-section extending at the foot of the droplet profile (a Mexican cap). For example this shape is exhibited from 20msec to 80msec at 270V as shown in figure 4.8. The width of the droplet is 0.72mm at 0V and spread to 3.03mm value over a period of typically 300msec at 270V and the width of the droplet is 0.7mm at 0V and spreading to 1.9mm value over a period of typically 100msec at 240V.

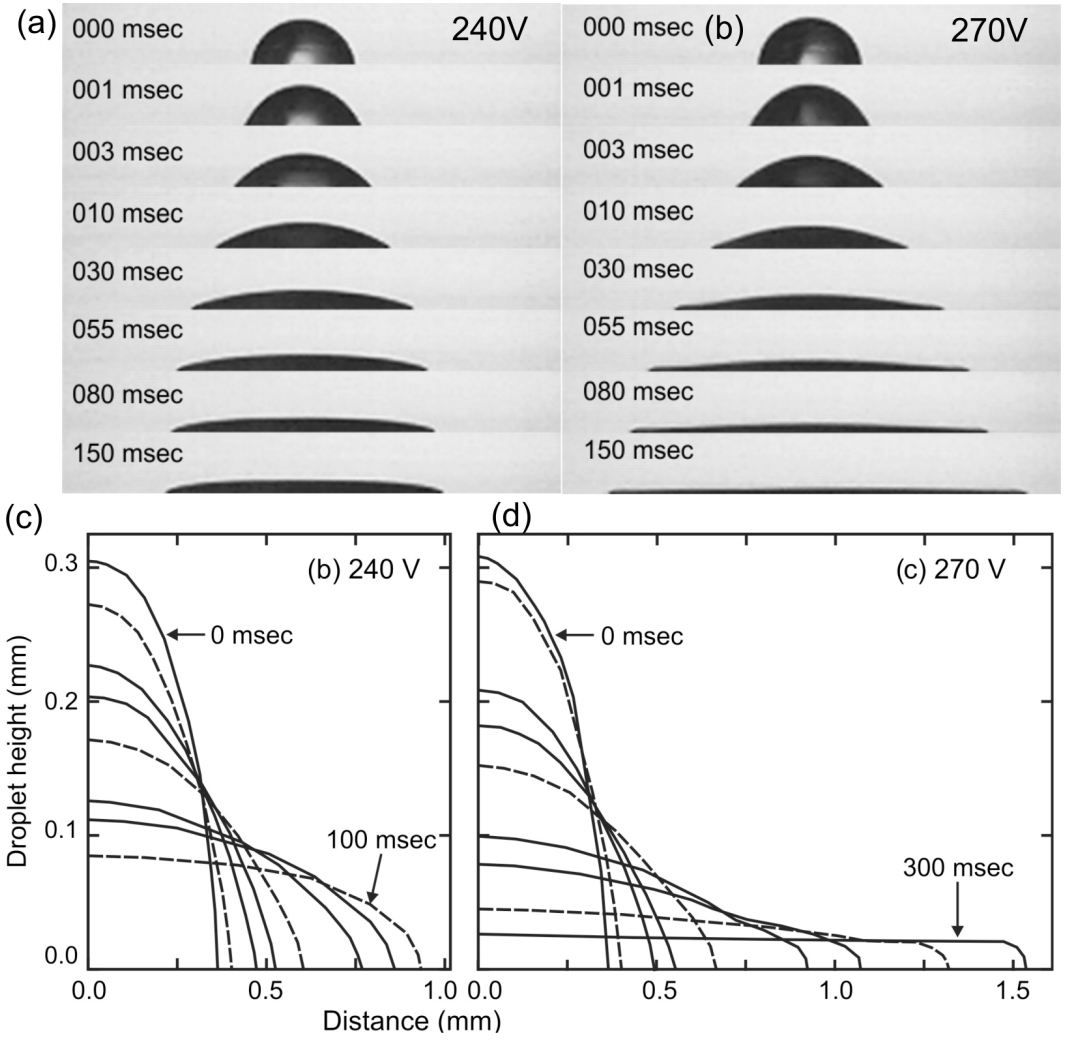

Figure 4.8: Figure (a) and (b) show the actual droplet spreading as a function of time from y-direction at 240V and 270V. Figure (c) and (d) show the digitised profiles of the droplet at times 0, 1 ms (dashed), 3 ms, 5 ms, 10 ms (dashed), 30 ms, 50 ms, 100 ms (dashed) and 300 ms.

4.6.1 Induced complete wetting and super-spreading for dynamic contact angle

Complete wetting

At the threshold voltage, V/V_{Th}=1. The dynamic contact angle tends to zero in the long time limit, hence the equation 4.28;

$$\frac{d\theta}{dt} \approx -\left(\frac{\lambda}{2}\right)\theta^{9/2} \tag{4.37}$$

By integrating the equation 4.37, becomes

$$\theta \approx \left(\frac{4}{7\lambda(t+t_o)}\right)^{2/7} \tag{4.38}$$

Where t_o is a constant of integration. Alternatively, we can write,

$$\frac{1}{\theta^{7/2}} - \frac{1}{\theta_o^{7/2}} \approx \frac{7\lambda t}{4} \tag{4.39}$$

Where θ_o is a constant. Equation 4.38 or 4.39 is the Tanners law [14] of the stripe form.

Super-spreading

When the applied voltage is above the threshold voltage, equation 4.28 rapidly becomes dominated by the voltage squared term then the equation 4.28 becomes,

$$\frac{d\theta}{dt} \approx -\lambda\left(\frac{V^2}{V_{Th}^2}\right)(1-cos\theta_y)\theta^{5/2} \tag{4.40}$$

By integrating the equation 4.40, becomes

$$\theta = \left[\frac{2}{3\lambda(1-cos\theta_y)\left(\frac{V}{V_o}\right)^2(t+t_o)}\right]^{2/3} \tag{4.41}$$

Where t_o is a constant of integration. Alternatively, we can write,

$$\frac{1}{\theta^{3/2}} - \frac{1}{\theta_o^{3/2}} \approx \frac{3\lambda(1 - cos\theta_y)}{2} \left[\frac{V}{V_{Th}}\right]^2 t \tag{4.42}$$

Where λ_o is a constant. Equation 4.41 or 4.42 is the voltage induced super-spreading for stripe form.

Previously McHale etal has reported that the exponent in time goes from $3/10^{th}$ power law to a $3/4^{th}$ for the super-spreading of a droplet induced by roughness [84]. In this approach the exponent in time goes from $2/7^{th}$ power law to a $2/3^{th}$ for the super-spreading of a droplet (in stripe form) induced by voltage.

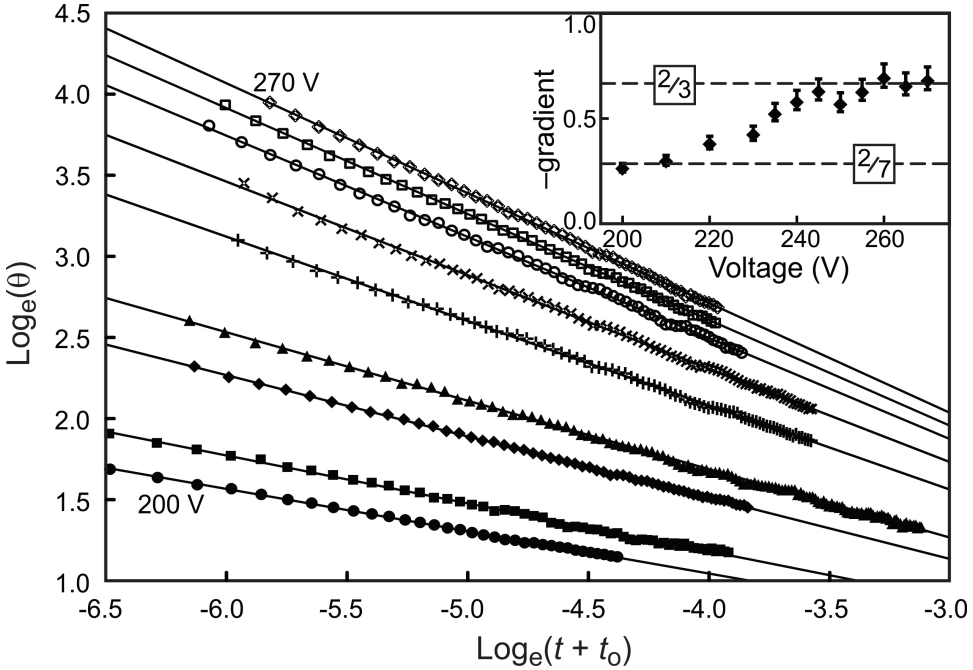

Figure 4.9: Data in the graph shows the power law spreading and super-spreading for applied voltage between 200V to 270V. Inset figure shows the exponent n from the complete wetting to super-spreading.

The theoretically expected $\theta \sim (t + t_o)^{-2/7}$ transitioning to $\theta \sim (t + t_o)^{-2/3}$ as the droplet going from complete wetting to super-spreading and this prediction is given by equation 4.38 and equation 4.41. The experimental data of the complete wetting to super-spreading with applied voltage between 200V and 270V are shown in figure 4.9. We performed a best straight line fit on lnθ against ln(t) with applied voltage (between 200V to 270V) for the experimental data to extract

the values of gradient, which gives "-n". The data were offset to pass through the origin for clarity.

The slope of the linear fit is reduced from the 200V to 270V as predicted by the complete wetting to the super-spreading which means the data shows that the switching speed becomes stronger as voltage increases. The gradient value is raised from close to -2/7 at 200V (just below the threshold voltage V_{Th}=230V) to -2/3 at 245V and it remains almost constant as the voltage increased as shown in inset figure 4.9. These experimental data has shown very good agreement with theoretical prediction for complete wetting to super-spreading law.

4.6.2 Induced complete wetting and super-spreading for dynamic contact widths

Complete wetting

At the threshold voltage, V/V_{Th}=1, it obeys power law equation 4.37, hence equation 4.34 becomes,

$$v_E(t) \approx \frac{\lambda}{2}\left(\frac{3\Omega}{8L_o}\right)^{1/2}\theta(t)^3 \tag{4.43}$$

and using equation 4.38 gives,

$$\frac{dx_o(t)}{dt} \approx \frac{\lambda^{1/7}}{2}\left(\frac{4}{7}\right)^{6/7}\frac{\lambda}{2}\left(\frac{3\Omega}{8L_o}\right)^{1/2}\frac{1}{(t+t_o)^{6/7}} \tag{4.44}$$

integrating this equation becomes,

$$x_o(t) \approx \frac{7\lambda^{1/7}}{2}\left(\frac{4}{7}\right)^{6/7}\frac{\lambda}{2}\left(\frac{3\Omega}{8L_o}\right)^{1/2}(t+t_o)^{1/7} \tag{4.45}$$

This approach obeys a $1/7^{th}$ power law in time.

Super-spreading

Above the threshold voltage, it obeys the super-spreading law (equation 4.40),

so the equation 4.34 becomes,

$$v_E(t) \approx \lambda \left(\frac{3\Omega}{8L_o}\right)^{1/2} \theta(t)(1 - cos\theta_y) \left(\frac{V}{V_{Th}}\right)^2 \tag{4.46}$$

and using equation 4.41, it becomes

$$\frac{dx_o(t)}{dt} \approx \lambda^{1/3} \left(\frac{3\Omega}{8L_o}\right)^{1/2} (1 - cos\theta_y)^{1/3} \left(\frac{V}{V_{Th}}\right)^{2/3} \frac{1}{(t + t_o)^{2/3}} \tag{4.47}$$

integrating this equation, becomes

$$x_o(t) \approx 3\lambda^{1/3} \left(\frac{3\Omega}{8L_o}\right)^{1/2} (1 - cos\theta_y)^{1/3} \left(\frac{V}{V_{Th}}\right)^{2/3} (t + t_o)^{1/3} \tag{4.48}$$

This approach obeys a $1/3^{th}$ power law in time.

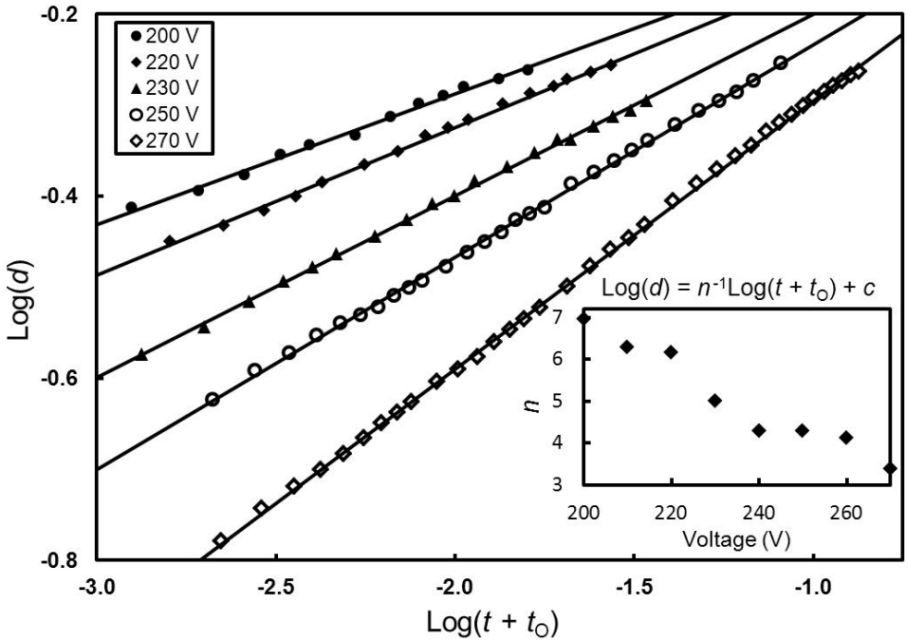

Figure 4.10: Graph shows the logarithm of the droplet width as a function of the logarithm of (t+t_o) for applied voltages of 200V, 220V, 230V, 250V and 270V. Inset figure shows the reciprocal exponent n from the complete wetting to super-spreading.

In order to test the prediction of the complete wetting $\theta \sim (t - t_o)^{1/7}$ transitioning to super-spreading $\theta \sim (t - t_o)^{1/3}$, the contact width of the droplet as a function of time was extracted using the image processing (previously discussed

in section 4.3) for a representative sample of voltage between 200V and 270V. The experimental data between 200V and 270V are plotted as logarithm of the droplet contact width vs the logarithm of (t+t_o) as shown in figure 4.10. We preformed a best straight line fit on log(d) against log(t+t_o) with applied voltage (between 200V to 270V) for the experimental data to extract the values of gradient to compare the theoretical approach, $d \sim (t + t_o)^n$, where the n value is given by the reciprocal of the gradient of the linear fit at each voltage. The data is offset to pass through the origin for clarity.

The slope of the linear fit is increased as voltage increases from the 200V to 270V as predicted by the complete wetting to the super-spreading. This data shows that the switching speed becomes stronger as voltage increases. The gradient value is raised from close to 1/7 at 200V (just below the threshold voltage V_{Th}=230V) to 1/3.39 at 270V as shown in inset figure 4.10 Which is consistent with the theoretically expected power law in equation 4.48 i.e $\theta \sim (t-t_o)^{1/3}$. This experimental data has shown a very good agreement with theoretical prediction for complete wetting to super-spreading power law.

4.7 Droplet dewetting

So far a forced wetting of a 1, 2 propylene glycol droplet induced by voltage was theoretically derived and also demonstrated experimentally. In this section, the dewetting of a 1, 2 propylene glycol will be discussed about how the contact angle behaves as a function of time in the condition of zero voltage (recovery of the droplet spherical shape). Briefly about the dewetting, when a droplet of 1, 2 propylene glycol is dispensed on the hydrophobised IDT device it creates a spherical cap with an angle of 85^o. A sine wave AC voltage is applied to the IDT electrode array creates a highly non-uniform electric field and this field is exponentially decayed with penetration depth. Due to the dielectrophoresis the droplet spreads along the electrode and when the voltage is removed the droplet

will be recovered close to its original shape in equilibrium time which means the contact angle is increased with time.

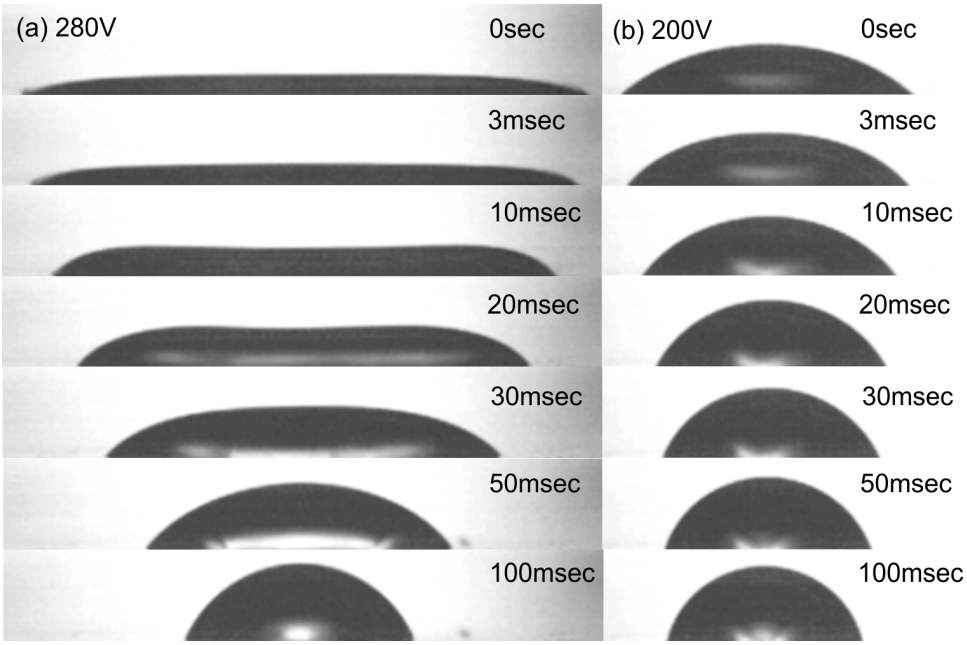

Figure 4.11: Figure showing the droplet dewetting along electrodes from a x-z plane view as a function of time after the voltage removed from 270V and 200V.

To understand how the contact angle and contact width evolves with time at no voltage from partial wetting, complete wetting and super-spreading regime, Initially a drop (volumes used in the range 0.98 $\pm$ 0.01 μL much larger than for wetting experiments) of 1, 2 propylene glycol is dispensed at the center of the IDT electrode array (line width = 40μm) which is coated with a hydrophobic SU8 layer having a thickness of 0.85μm and then the device was mounted in the experimental set-up. A 10kHz sine wave 280V is applied to the IDT electrode array. The contact angle of the drop was reduced as a function of time until to reach equilibrium contact angle. When the voltage is removed the contact angle of the droplet is increased as a function of time. The time dependent droplet images were recorded in y-direction during droplet dewetting for each 10V step from 40V to 290V. The time dependent contact angle of the droplet was obtained by analysing the time dependent droplet images using automated Drop Shape Analysis software.

Figure 4.11 shows the actual droplet dewetting along the electrode array from the y-direction as a function of time at times of 0sec, 5msec, 10msec, 20msec, 30msec, 50msec and 100msec after a 10kHz sine wave 280V and 200V is removed. At the 200V ($< V_{Th}$), the droplet appears as circular arc shape from the y-direction with angle of 36.5^o. When the voltage is switched off, the droplet de-wets the surface along the electrode array (shown in 4.12) whilst the width of the droplet is decreased. At the 280V ($> V_{Th}$), the droplet appears as a thin film from the y-direction. When the voltage is switched off, the three phase contact lines very strongly pull towards the center (shown in figure 4.12). Therefore initially the shape of the droplet was a thin film and as a function of time the height was increased whilst the contact width was decreased but the shape of the liquid remains unchanged for 10msec to 45msec. At 45msec the droplet is adopted the circular arc shape. After 200msec, the circular arc shape of the droplet was hardly changed for voltages including below and above the threshold voltage.

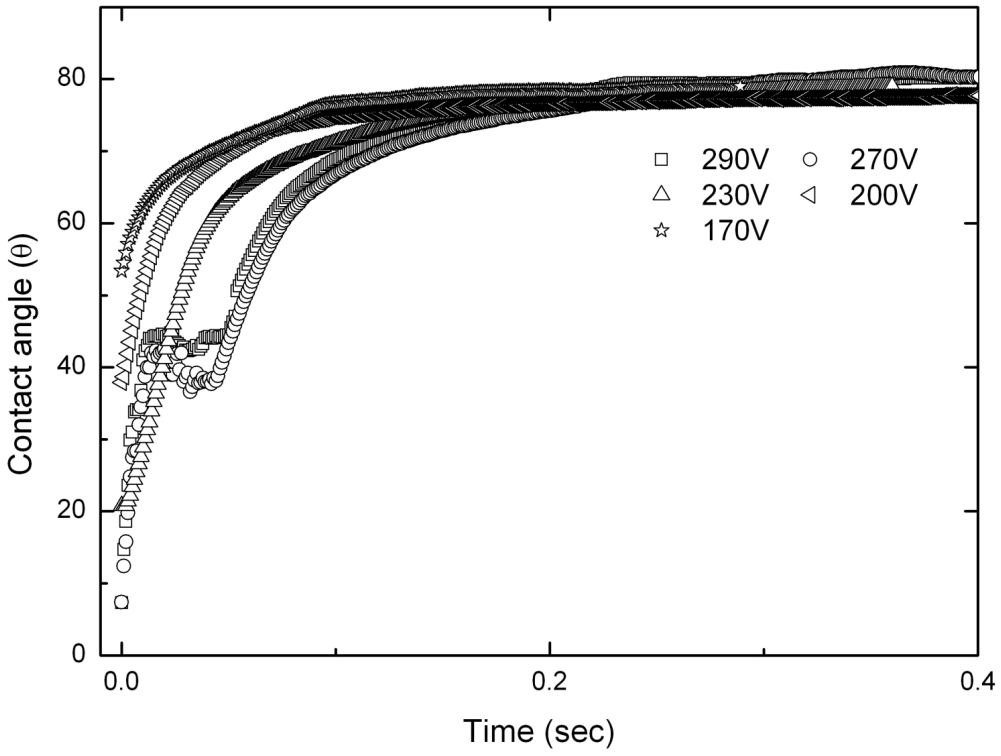

Figure 4.12: Graph shows the theta evolve as a function of time.

Figure 4.13 shows the time dependent de-wetting contact angle at 170V, 200V,

230V, 270V and 290V. The circular arc method has been used for the lower voltage (for example 170V, 200V and 230V) because the shape of the droplet was well defined by the circular method. The data have shown the theta is monotonically increased until it reaches to the $\sim 75^o$. After 200msec, there is a very little change in the contact angle for below threshold voltages. For 270V and 290V (above threshold voltage), the first few data points are measured using the manual method since the circular or tangent 2 method were not well described the shape. Initial the time dependent few data points (theta as a function time) of the 270V and 290V are abruptly increased until 10msec. From 10msec to 45msec the constant theta was obtained since droplet shape was unchanged but the contact width was increased. After 50msec, it is abruptly increased until reaches to the $\sim 75^o$. After 200msec, there was a very little change in the contact angle for above threshold voltages.

4.8 Conclusion

We have shown how the applied voltage to the interdigitated electrodes affects the wetting behaviour and this behaviour demonstrated with a 1, 2 propylene glycol on the IDT electrode array. Using a modified Hoffman de Gennes law, the wetting behaviour is divided into three regime according to applied voltage such as partial wetting at $V \ll V_{Th}$, complete wetting at $V \simeq V_{Th}$ and super-spreading $V \gg V_{Th}$. These effects has been summarized in terms of the theory regarding (modified Hoffman-de Gennes law) which explains behaviour of the dynamic contact angle and dynamic width at different voltages. The threshold voltage is 230V which is determined from the equilibrium contact angles of the droplet at applied voltages from 40V to 270V. The experimental results of the droplet spreading at the below threshold voltage have shown the contact angle or contact width of the droplet exponentially reaches to the equilibrium as predicted by theoretical approach (equation 4.33 and 4.36). We have achieved the super-

spreading without adding any external surfactant to the droplet. The power laws for the dynamic contact angle of the complete wetting to super-spreading has been derived and experimentally demonstrated. The exponent of the theta in time goes from $2/7^{th}$ power law to a $2/3^{th}$ for the super-spreading of a droplet, in stripe form, induced by voltage. These experimental data has shown very good agreement with theoretical prediction for complete wetting to super-spreading law. The super-spreading regime power law ($d \sim (t + t_o)^{1/3.39}$) has found at 270V which is consistent with the theoretically predicted power law ($d \sim (t + t_o)^{1/3}$).

Dewetting: At no voltage condition the droplet was recovered close to its original shape in equilibrium time which means the contact angle is increased with time. At higher voltage (230V to 290V) the data, contact angle vs time, has shown the offset because the droplet shape was not changed over this period. However for each voltage the equilibrium contact angle ($75^o \pm 3^o$) is obtained at 400msec.

Chapter 5

Solid gratings

5.1 Introduction

Electric field induced or assisted casting and patterning of polymer layers has previously been achieved by coating one plate of a capacitor structure with a thin film of polymer melt. The normal electric field creates electrohydrodynamic instabilities at the interface between a polymer film and an air layer within the capacitor which evolve to give regular self-organized structures [19–21]. This effect has been used to create polymer surface patterns with sub-micrometer feature sizes, to assist in the creation of accurate moulds [90], and has also been exploited to fabricate novel optical devices [91, 92]. Normal electric fields have also been used prior to and during UV curing of resin droplets deposited by ink-jet printing to modify the shapes of millimetre scale lenses and to create aspheric lenses [93, 94]. In-plane electric field geometries have been used to achieve pattern formation on polymers and phase separation of polymer mixtures [95–97]. In optical devices this effect has been exploited to create polymer walls around pixels of a display [98, 99] since the phase separation of liquid crystal material and UV curable polymer occurs predominantly in the vicinity of the strongest non-uniform fringing electric fields in the gaps between in-plane electrodes [100]. Previously our group has shown that an insulating fluid can be spread into a thin film by the action of dielectrophoresis forces [43] created by applying an A.C voltage. The voltage is applied between the fingers of an interdigital striped electrode array on which the sessile oil droplet rests [18]. Further increase of the magnitude of the voltage results in the appearance of periodic wrinkle at the oil/air interface of the spread film. The wrinkle amplitude depends on the film thickness and the applied voltage, and is also predicted to depend on the dielectric constant and surface tension of the oil [17, 18]. This chapter demonstrates how non uniform electric fields and the accompanying dielectrophoresis forces can be used to create a periodic phase grating of desired amplitude and desired optical properties in a liquid UV curable material which can be set to a solid using UV

light to create a permanent diffraction grating. This chapter also demonstrates how the monochromatic light is diffracted in to the higher orders and how the 0^o order is minimised while the UV epoxy curing.

5.2 Experimental methods

5.2.1 Principle of wrinkling effect

An interdigitated (IDT) electrode array pattern is used in these experiments to characterize the dynamics of the three phase contact line movement of the droplet. The interdigitated electrode array, with an area of 5mm $\times$ 5mm, was fabricated using standard photolithography techniques (indium tin oxide (ITO) thickness of 25nm) on borosilicate glass.

When a voltage is applied to the each alternative electrode finger with the interposed electrodes at earth potential in a interdigital striped array (IDT) of electrodes, it creates a highly non-uniform electric field. In this non-uniform electric field a dielectric material experiences a dielectrophoretic force (explained in section 1.6) in the direction of the increase in the magnitude of electric field gradient. Dielectrophoresis induced flow force is proportional to the gradient of square of the electric field gradient and is independent on the polarity of the electric field. The electric field gradient is high in between the electrodes so the dielectrophoretic forces in these regions cause the dielectric liquid to collect there preferentially and in turn liquid from the region above of the electrodes are removed as shown in figure 5.1 and resulting of an undulation at the liquid/air interface. The electrode pitch (is double of the electrode line width) is equal to the grating pitch and the electrical pitch is equal to the double of the electrode pitch. The wrinkles are reproducible, stable and static at a fixed voltage. The peaks and troughs of the grating are parallel to the electrode line along the x-direction.

The amplitude of the wrinkle dependence on the applied voltage and liquid

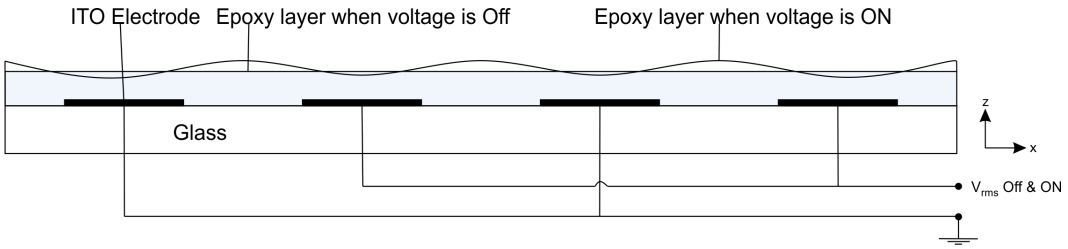

Figure 5.1: Schematic representation of the wrinkle forming at the oil and air interface

properties including surface tension and dielectric constant. The amplitude is proportional to the applied voltage square [17, 18].

It acts as a phase grating since it has a periodic variation in the optical path length. When a beam is transmitted through the periodic undulation of a transparent epoxy layer it diffracts into the higher orders (shown in inner figure 5.2). The intensities of the individual diffraction spots depend on the amplitude of the wrinkles (which is related to the optical path length).

5.2.2 Experimental setup

The experimental set-up consists of a voltage addressing unit, a He-Ne laser of wavelength 633nm, two mirrors and a photo diode (DET36A, Thorlabs, UK) which is attached to the arm swing motor and a UV lamp (T5 UV fluorescent tube, Philips lighting, Netherlands). A 10 kHz square wave voltage applied to the each alternative electrode finger with the interposed electrodes at earth potential. The AC voltage was provided by a TTi TGA1244 arbitrary wave form generator (Thurlby Thander Instruments Limited, Cambs, UK) with each Signal being amplified 100 times with a PDZ350 amplifier (Trek Inc., Medina, New York, USA). An oscilloscope and a multi meter were connected to the amplifier to monitor the wave form and to measure the V_{rms} voltage.

To monitor the intensities of the diffraction orders as the wrinkle amplitude evolves, a He-Ne laser (1.5mW, 632nm wavelength, monochromatic beam), per-

pendicularly polarised to the electrode array, and was illuminated in transmission through the centre of the electrode array. Initially the beam was reflected at the mirror which is tilted in 45^o and transmitted through the sample resulting of a series of diffraction pattern. The diffraction patterns are reflected from second mirror to photodiode detector (DET36A, Thorlabs, UK). A resistance of 5kΩ is added between the detector and oscilloscope to compromise the signal speed. Detector is attached to the arm swing motor which can able to rotate from 6^o to -6^o to monitor the individual intensities of the diffraction pattern, and to capture the angular scans from 3^o to -3^o as shown in figure 5.2. The speed and angle of the rotation was controlled using the Lab view program which was designed by Dr Gary Wells.

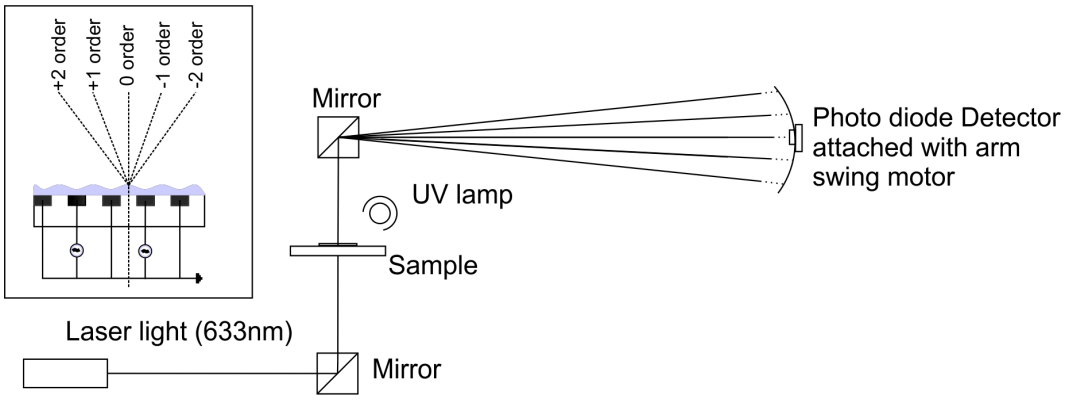

Figure 5.2: Schematic representation of the experimental setup for fabrication of the solid grating, an inner picture shows the creation of the diffraction pattern

For curing a UV curable resin (epoxy), a 8 watt ultra violet light source was used which have the peak wave length of 375nm with spectral width of 20nm at half maximum (T5 UV fluorescent tube, Philips lighting, Netherlands). It was placed in 45^o to the sample with distance of 60mm away.

5.3 Fabrication of the solid phase grating

5.3.1 UV curable resin deposition

A UV curable resin (NOA65, NJ, USA) is used for solid grating fabrication studies. Initially it is diluted in acetone with 10% by weight to allow deposition as a thin film. A volume-calibrated Gilson Pipetman 0.1 to 10 μL micro-pipette was used to dispense a 10$\pm$1 μL droplet of UV curable resin over the 5mm $\times$ 5mm interdigitated electrodes to facilitate the drop of epoxy with constant of volume for every experiment. The epoxy was obtained an isotropic spreading on the glass substrate. It was left in the fume cupboard for 60sec to evaporate the solvent. A drying ring shape was formed on the IDT device with typical diameter of the ring is between 14 to 16 mm and central thickness is 2 to 3μm with variation less than the $\pm$0.5μm and an annular lip around the edge of typical width of 2mm and maximum height of 5μm (shown in figure 5.3).

R Deegan has explained a phenomenon of forming a drying ring shape of a coffee drop or a polymer on the glass substrate [101, 102]. According to Deegan, when a polymer is spreading on the glass substrate the bottom molecules are pinned to the glass substrate and rest of the molecules are flown outward while the solvent is evaporating resulting a ring shape [101, 102]. We believe the drying ring pattern is appeared due to the edge pinning effect.

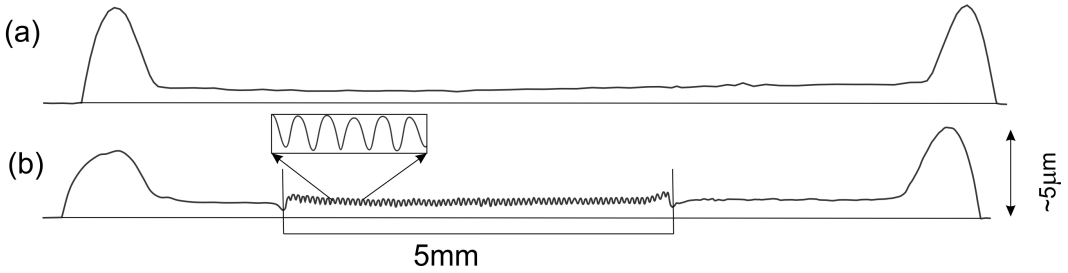

Figure 5.3: (a) 2D view of the epoxy shape after acetone evaporated from the epoxy solution, (b) wrinkle were created in the region of the electrodes under the influence of the L-DEP

In order to investigate the evaporation of the acetone present in epoxy solution, an experiment was performed using a sensitive mass balance (kern ALJ160-4NM). In this experiment, a 40±1μl of the epoxy solution was deposited on the glass substrate and the mass of the solution was measured as a function of time. The figure 5.4 explains the mass of the three distinct droplets of epoxy solution as a function of time. A larger droplet was used here than during the subsequent grating fabrication experiments to make use of the sensitivity of the mass balance (Kern ALJ160-4NM). The dispensing of the droplet onto the substrate commenced at time t = 0 s. A sharp peak was observed at first 3 seconds corresponds to the time period was occurred due to the dispensing the drop. The mass of the epoxy solution is monotonically decreased for 30sec after the sharp peak, and at 30 to 40 seconds the mass of the epoxy is settled with a constant value of the 0.0034 ± 0.0002g. The mass of the film asymptotes close to this value between 30 and 40 s after the dispensing commences. The acetone evaporates to leave a film of NOA65 shaped as a roughly circular drying ring.

After acetone evaporated from the epoxy solution, the device was mounted in the sample holder which was connected to the voltage addressing unit. A 10kHz square wave with voltage of peak amplitude V_o was applied to the each alternative electrode in the array (interposed electrodes were connected to the earth) with resulting of a non-uniform electric field. The wrinkles, a periodic corrugation, were created at the epoxy and air interface due to the dielectrophoresis force as previously explained in section 1.5. The amplitude of the wrinkles can be modified by adjusting the applied voltage. When a beam is illuminated in transmission through the periodic undulation of the epoxy it was created the series of diffraction because of the period variation in the optical path length of the laser light transmitted through it.

The amplitude of the wrinkle was monotonically increased as voltage was increased; therefore, the optical path length changes for the beam. The intensities of the diffracted orders were varied between the maximum and minimum because

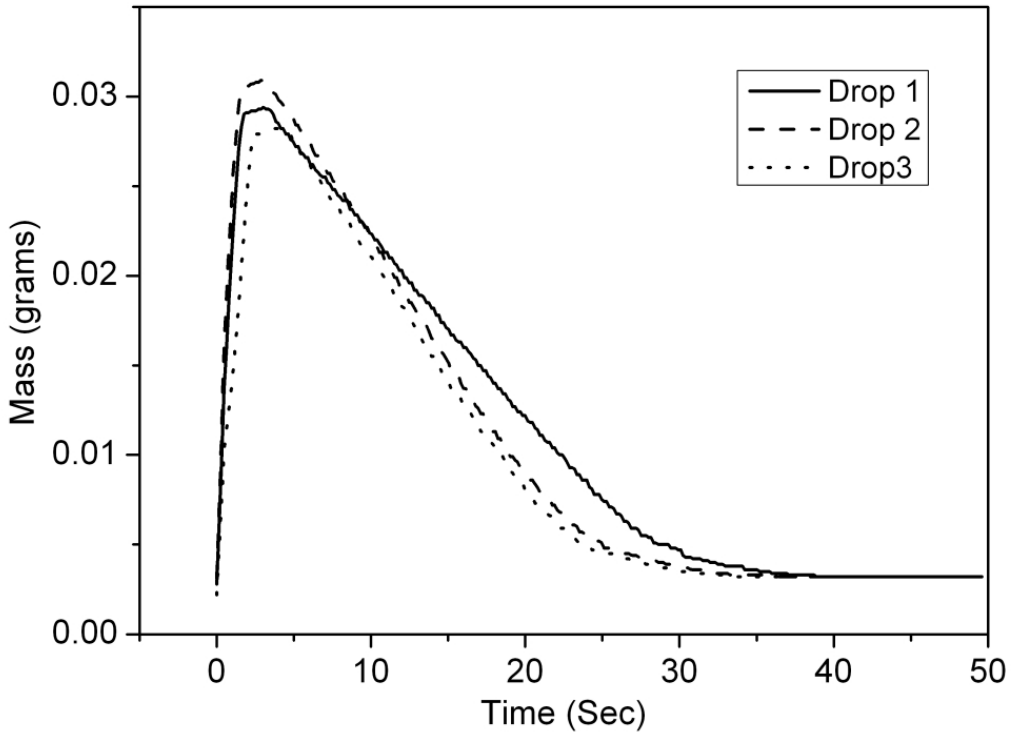

Figure 5.4: The mass of four distinct 40±2 μl initial volume droplets of resin/acetone solution as a function of time.

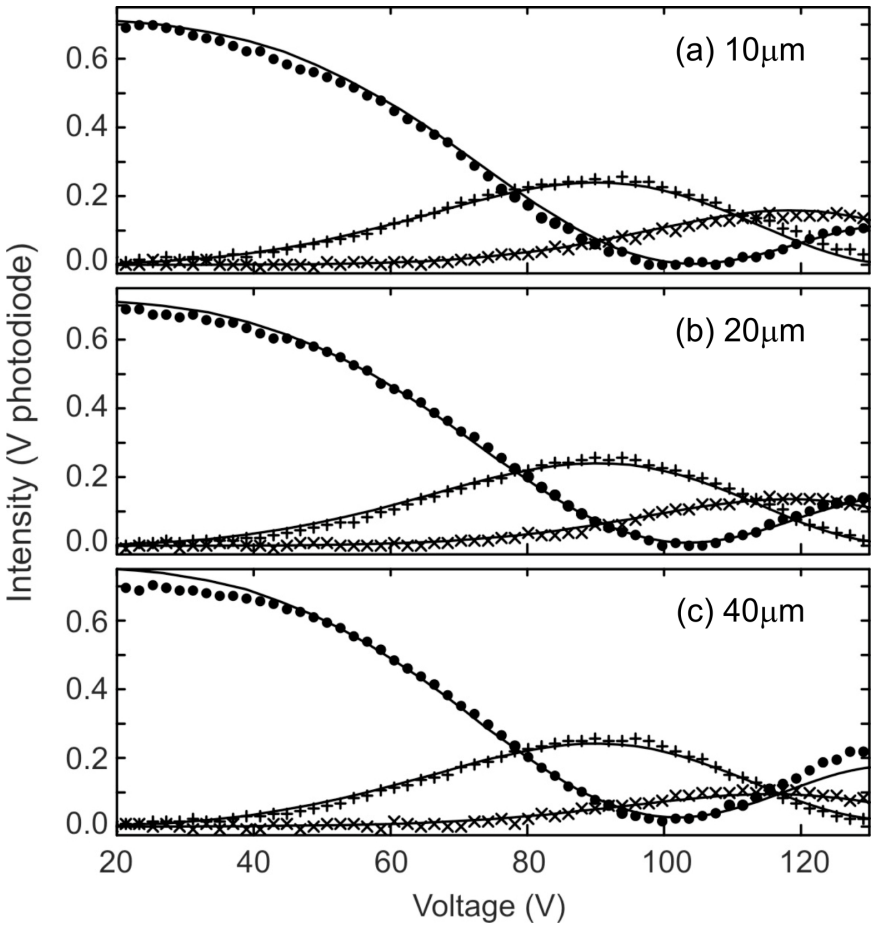

Figure 5.5: Intensity of the 0th, 1st and 2nd order as a function of applied voltage for the 80μm, 40μm, 20μm electrode pitch devices. The solid lines are the theoretical predictions using the FDTD method.

of the oscillating phase difference between a ray travelling through the trough of the wrinkle and a ray travelling through an adjacent peak of the wrinkle which creates the constructive and destructive interferences.

In order to determine the required voltage to achieve the minimum intensity of the 0^{th} order, a 10kHz square wave which is modulated by another a slow triangular wave (period of 120sec) was applied to the interdigitated electrodes having a line width of 40μm. The voltage was slowly ramped from 17V to 128V and the amplitude of the wrinkle at the interface of the epoxy and air was monotonically increased. In the meanwhile a 633nm laser was illuminated in transmission through the wrinkle surface, and the intensities of the diffracted orders were varied as a function of the optical path length. The intensities of the diffraction orders were recorded using the photo diodes. This experiment was repeated with other line width interdigitated electrode devices such as 10μm and 20μm.

The intensities of the zero, first and second order for 20μm, 40μm and 80μm electrode pitch were shown in figure 5.5. In the figure 5.5 the solid lines were shown the fits to the diffracted order for each electrode width by the square of a Bessel function of the first kind, $J_q^2(\alpha V^2)$ where α represents single fitting parameter and q represents the diffracted order. This assumes that the wrinkle profile was sinusoidal during the amplitude evolved. It also shows that the intensity verses voltage squared relationship tends more towards the ideal Bessel case as the pitch of the electrodes is reduced. The minimum intensity of the zeroth order was obtained at the 105 $\pm$ 5V for all three different electrode pitches.

At voltage of 105V a laser beam was illuminated through the grating and an angular scan was performed at 0.05 radians per second across the diffraction pattern from +3 to -3 orders as previously described in section 5.2.4. The angle scan versus the diffraction spot intensities from has shown in figure 5.6. In figure 5.6, the peaks represent the intensities of the diffracted spots (such as -3, -2, -1, 0, +1, +2, +3 respectively) and 0^{th} order is centre in the angular scan (0^o). The 0^{th} order intensity is achieved minimum at 104V for the 40μm line width device.

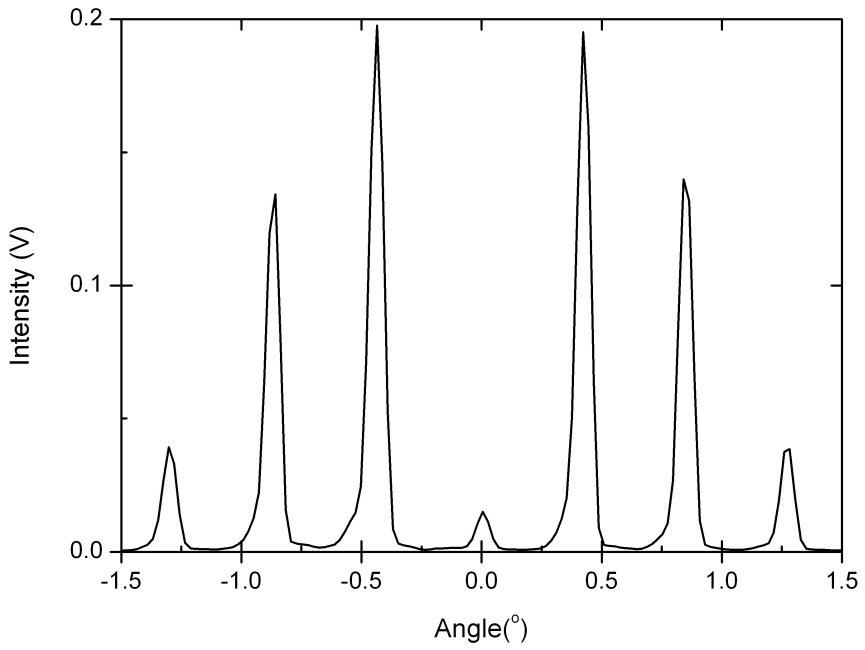

Figure 5.6: Graph showing the angle scans of the diffraction spot intensities for 40μm line width electrode geometry where the epoxy in liquid state.

5.3.2 Characterisation of the UV curing resin

The next stage of the solid grating fabrication was UV curing in situ, while the voltage is applied, to create a permanent solid grating. In order to characterise the change in responsive with time of the epoxy as a function of the UV curing, initially a 10μl drop of epoxy/acetone solution was dispensed on the interdigitated electrode device and left in fume cupboard for 5min to evaporate the acetone. A 10 kHz square wave which is modulated with another a 1/60 Hz slow square wave was applied to the interdigitated electrodes array. The amplitude of the voltage was discontinuously changed from 10V to 90V every 30sec, as shown in the figure 5.7 (top) since the high intensity of the first order was obtained at 90 $\pm$ 5V, according to the previous section (section 5.3.1). At this voltage interval, the first diffracted order switches from its minimum to its first maximum in intensity. Simultaneously an 8W UV lamp (T5 UV fluorescent tube, Philips Lighting, Netherlands) was continuously illuminated from 60mm away at 45^o to the epoxy

layer.

After t=0 sec of the voltage applied to the electrodes, wrinkles were created

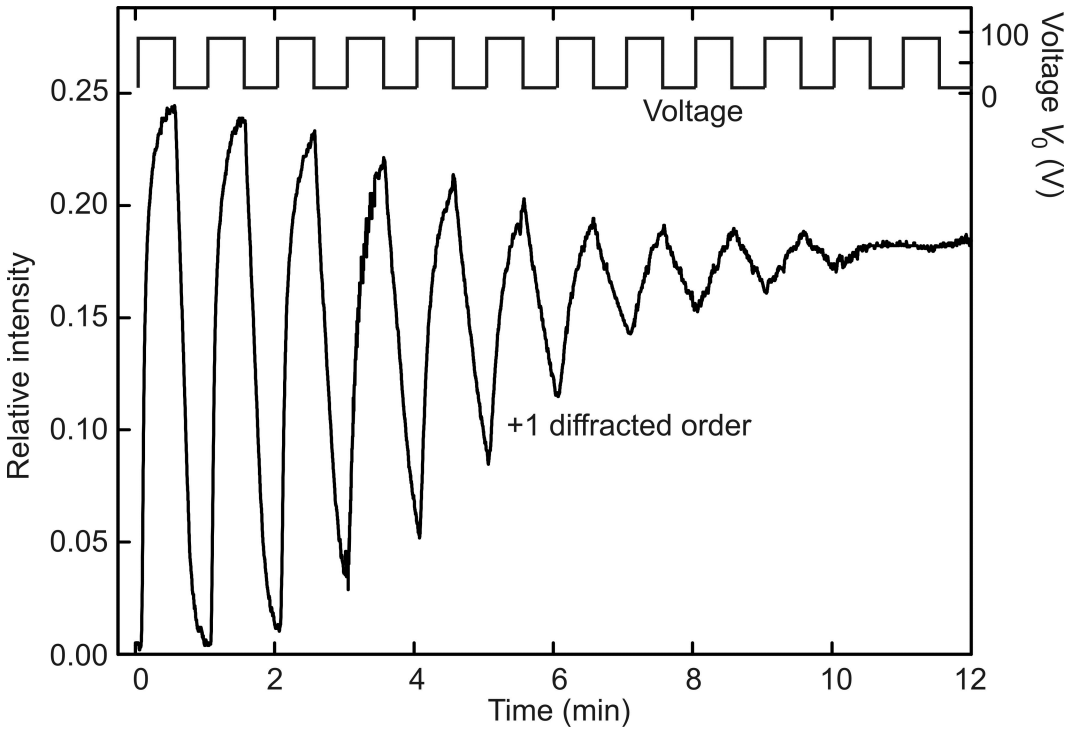

Figure 5.7: While curing the epoxy, the intensity of the 1st diffracted order was monitored in response to a 10 kHz square wave which is modulated with another square wave with a period of 60 seconds.

at the interface of the epoxy/air interface, and resulting of the intensity of the first diffracted order were sharply raised from minimum to maximum. At 30 sec the intensity of the first order was abruptly reduced, because the amplitude of the wrinkle was decaying (relaxing) back toward zero. In subsequent cycles, the gradient of the first order response was significantly reduced after each sudden change in the applied voltage. The amplitude of the peak to peak intensity response was decreased as shown in figure 5.7. The viscosity of the epoxy was increased as curing progresses under the UV light, which means the wrinkles amplitude became less responsive to change in the voltage. Little change in the response of the first diffracted order was observed after 720sec of curing as shown in figure 5.7, which due to the wrinkles amplitude becoming fixed.

Figure 5.8 shows the hysteresis response of the first diffracted order as a func-

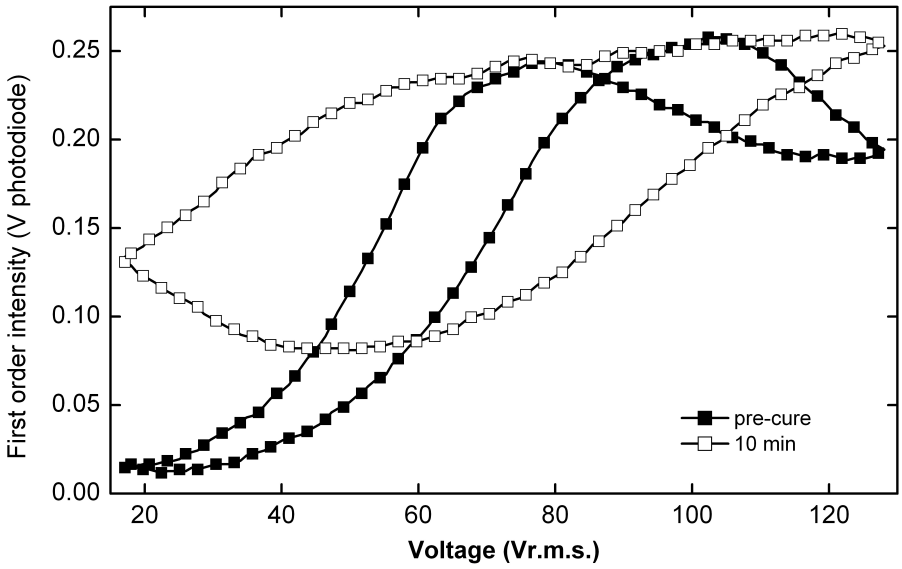

Figure 5.8: Hysteresis curves of the 1st diffracted order for one complete cycle of increasing and decreasing voltage, which is modulated with triangle signal. After a curing time of the 0min (filled squares) and 10min (open squares).

tion of linear voltage ramp before curing and after 10min curing (UV illumination was removed while the diffraction pattern intensity recording). A drop of epoxy/acetone solution was dispensed on the interdigitated electrodes array having line width of 20 μm and left in the fume cupboard for 5min. After 5 min a 10 kHz square wave was applied to the electrode array which was modulated using a triangular wave with a period of 120 seconds. The minimum voltage was 15V and the maximum voltage was 120V. The intensity of the first diffracted order was recorded using a DET36A Photo diode with a 5kΩ series resistance while voltage was gradually increased and decreased from 15V to 120V. After the initial cycle of first order intensities were captured, the sample was exposed to a UV lamp at a distance of 6cm and an angle of 45^o. After 10min of flood exposing the intensity of the first order was recorded while voltage was increased and decreased from 15V to 120V. Hysteresis curves are shown for one complete cycle of increasing and decreasing voltage for cure times of 0 and 10 minutes.

Well, by considering the previous experimental results (such as required voltage and exposing time), we fabricated a solid grating with suppressed 0^{th} order. Initially a drop of the resin/acetone solution was dispensed on the interdigitated electrodes (line width of 10μm, 20μm and 40μm) and left in fume cupboard for 10 min. Then a thin layer, having diameter of the 14 mm, was created on the electrode array with central thickness of 2.45μm. A voltage of $V_o = 100$ V, 10 kHz sine wave, was applied to the electrode device simultaneously a 633 nm laser light is illuminated in transmission through the wrinkle surface to monitor the zeroth order of the diffraction series. The voltage was then gradually increased until the output of the zero order was minimised. The voltages at which this minimum occurred were 106 V, 105 V and 104 V for the 10μm, 20μm and 40μm line width electrode devices respectively. When zero diffracted order had been minimised, UV curing was initiated in the same way as previously described. The intensity of the 0^{th} order was monitored using photo diode as the curing progressed and the voltage was continuously adjusted to minimise the 0^{th} order intensity. In practice the voltage was increased by 15V for first 10 minutes of curing for three different pitch electrodes. This was carried out for thirty minutes until the sample was fully cured and solidified.

After being fully cured, the angular scans were performed, for each electrode line width devices, at 0.05 radians per second across the diffraction pattern in the same way as previously described in section 5.2.4. An angle scan of the diffraction patterns of the 20μm, 40μm, 80μm electrode pitch were shown in the figure 5.9. A 2D profile of the solid grating was measured across the gratings using the stylus profilometer as described in section 2.3. The thickness of the layer was measured by scraping away part of the layer at the edge to create a step, and scanned. The average of the layer thickness were h= 2.25μm, 2.82μm and 2.71μm for electrode pitch of 20μm, 40μm and 80μm respectively. For three different pitches, scans were also performed across the entirety of the electrode region and showed good uniformity in the layer thickness above the electrodes.The scans were performed

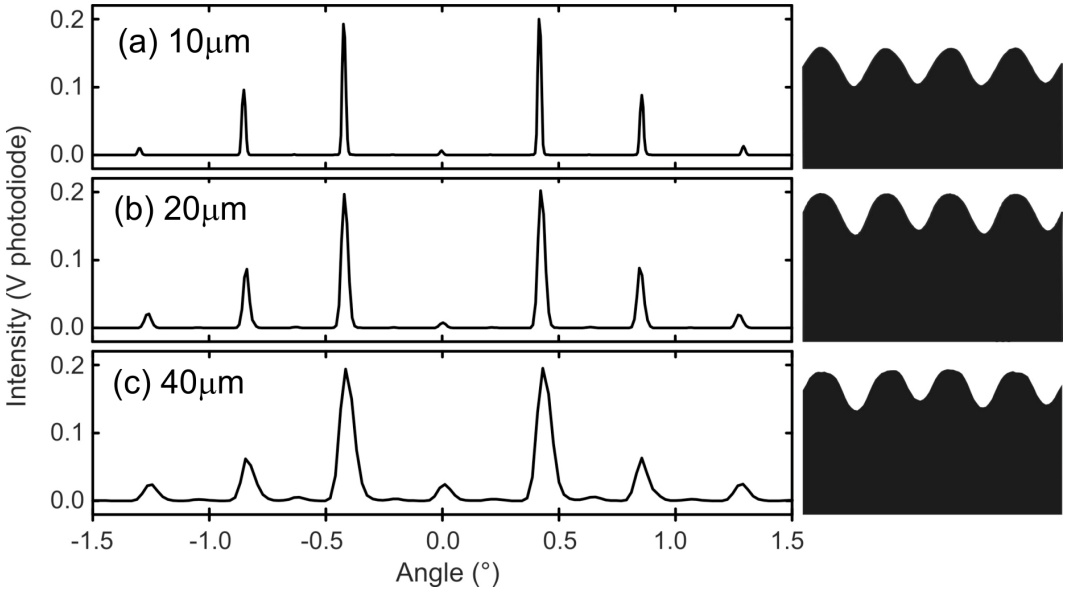

Figure 5.9: illustrates the diffracted intensity versus angle scans for samples with electrodes line width of (a) 10μm, (b) 20μm and (c) 40μm, 2D profile of the fully cured solid gratings measured using a stylus contact profiler.

in the same region as the incident laser which created the intensity scans. The average peak to peak amplitude of the wrinkle for three different line width was A = 0.81μm, 0.84μm and 0.80μm for 10μm, 20μm and 40μm respectively. The actual 2D profiles are shown in the figure 5.9. [103]

The scans of the gratings demonstrated that the intensities of the diffraction patterns were not determined by only the depth of the optical path, and also depend on the shape of the wrinkle. A lowest intensity of the 0^{th} order was achieved with 10μm line width electrode device and shown in the figure 5.9 with a 2D profile that was the closest to a simple sinusoidal shape.

5.3.3 Investigation of the polarisation effect and uniformity of the sample

In order to characterise the polarisation sensitivity of the device, a fully cured solid grating device having an electrode line width of 10μm was placed in the sample holder whilst a 633nm laser was illuminated transmission through the centre of the grating. Intensities of the +1, 0 and -1 order were recorded using

the photo diodes as a function of polarisation angle (where the polarised laser light was rotated with an angle of 45^o).

Diffraction efficiency $\eta(q)$ of the qth order is determined from the $100 \times \mathrm{I}(q)/I_o$,

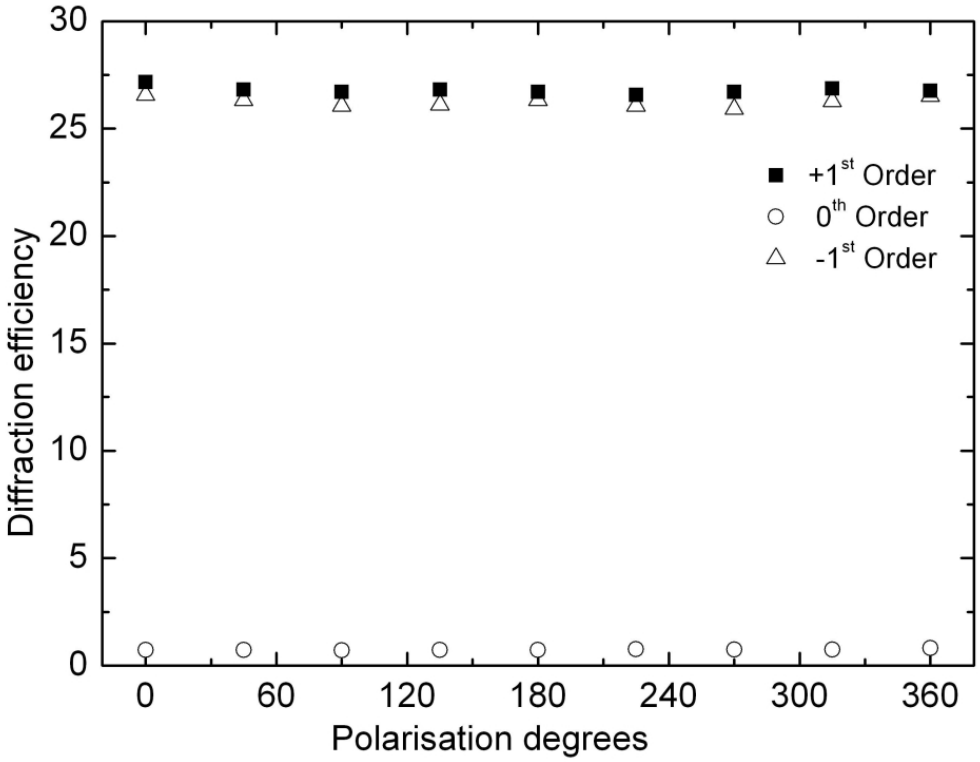

Figure 5.10: shows that diffraction efficiencies of the +1, 0 -1 order with respect to different polarisation angle of the laser relative to the stripes (y-direction).

where I_o represents the intensity of the incident laser light and I(q) is the intensity of the q^{th} order. The efficiency of the first order $q(+1)$ was 27.2±0.1%, 26.7±0.1%, 26.7±0.1% and 26.8±0.1% for the laser polarised in an angle of 0^o, 90^o, 180^o and 270^o respectively to the wrinkles as shown in figure 5.10. It has shown low polarisation sensitivity (closed to estimated experimental uncertainty). A slight asymmetries between the +1 and -1 diffraction efficiency occurred due to the small asymmetries observed between the neighbouring periods in the surface profile.

In order to define the uniformity of the solid gratings, the diffraction efficiencies of the +1, 0 and -1 orders were measured by illuminating the 633nm laser light

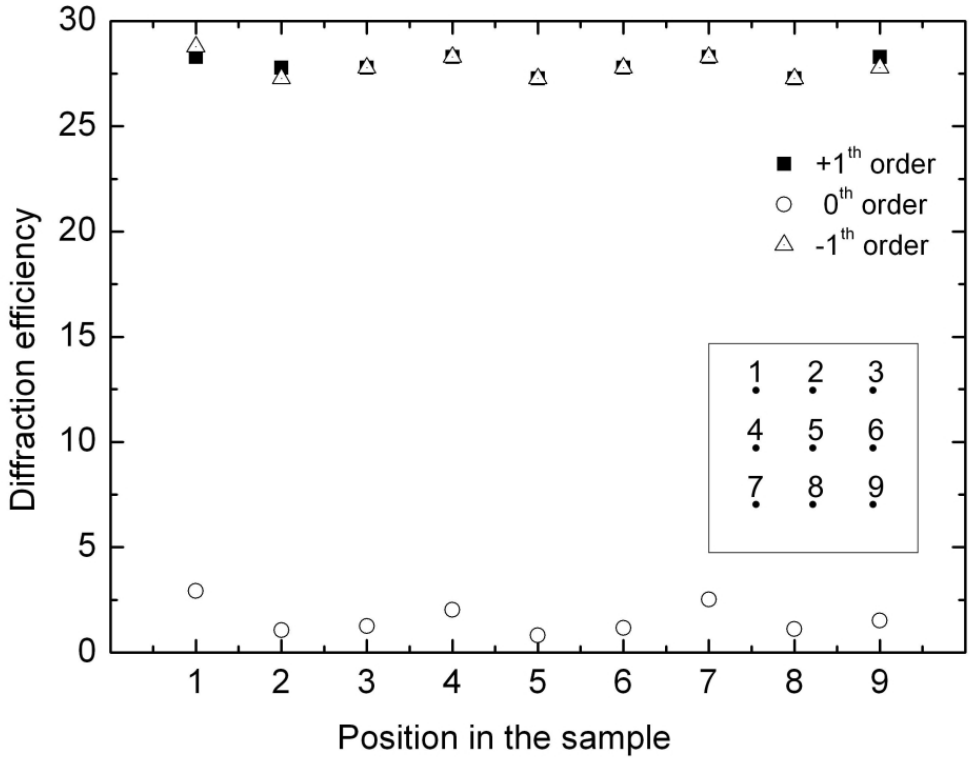

Figure 5.11: Graph shows the diffraction efficiency of the +1, 0 and -1 orders as a fraction of total incident intensity of laser light at 633 nm transmitted through at 8 positions symmetrically around the center of the 10μm line width electrode array. The inner picture is a schematic representation of a 5mm×5mm electrode area and dots represent the positions where a laser light is illuminated.

transmission through the sample at 8 symmetrical positions around the centre and 2mm away from the edges of the electrode area. The diffraction efficiencies were in the range of $\eta_q(+1) = 27.2\%$ to 28.2% and $\eta_q(0) = 0.8\%$ to 2.2% as shown in figure 5.11, which is due to the variation in the thickness across the liquid resin.

5.4 Conclusion

This new electric-field-assisted approach has shown to produce the solid optical device in micrometer-scale features where the optical properties of the device were voltage preselected when the optical device in liquid state [103]. The simple fabrication process has shown how the voltage was continuously modified to produce a solid grating with suppressed 0th order whilst the UV curing. 0th order of the diffraction pattern was minimum in the 10μm electrode width device which was the closest to a simple sinusoidal shape. The devices were low sensitive to polarization. The grating is consisted of 250 periods covering an area of 5mm.

Chapter 6

Wrinkle Dynamics

6.1 Introduction

Brown et al. reported a novel approach to produce a static wrinkle at air/oil interface using a dielectrophoretic force and this force was produced by applying a constant voltage to the interdigitated electrode array, of coplanar strip electrodes, [17, 18, 104]. The wrinkles are stable, static and reproducible. The amplitude of the wrinkle is directly proportional to the applied voltage square (A $\propto V^2$) and an exponential function of the ratio of the thickness of the oil layer and pitch of the electrode array (h/p) for a range of oil layer thickness and line width of electrodes [17]. The amplitude was controlled by the applied voltage and determined by the liquid properties such as surface tension and permittivity. A non-sinusoidal profile (higher Fourier components) can be achieved at the longer electrode line width with a lower permittivity liquid and these components are most prominent at a lower film thickness [18]. These wrinkles act as a thin sinusoidal phase grating which means when a monochromatic light is illuminated through the liquid gratings it creates a series of diffraction spots whose intensities depend on the amplitude of the wrinkles.

In this chapter we discuss about the dynamics of the wrinkles, primarily how the wrinkles switch and relax for a range of oil film thickness (12.6μm to 26.1μm) and electrode line width (20μm, 40μm and 80μm). We have constructed an experimental set-up where the intensities of the diffraction patterns are recorded and the thickness of the oil layer is measured using a Mach-Zehnder interferometer. A linear relation between the phase delay (m) and the voltage square is experimentally demonstrated which is consistent with the Brown et al work [17]. The theoretical relationship between the relaxation time and p^4/h^3 is derived and also experimentally tested.

6.2 Device operation

An interdigitated (IDT) electrode array pattern is used in these experiments to characterize the dynamics of the three phase contact line movement of the droplet. The interdigitated electrode array, with an area of 5mm $\times$ 5mm, was fabricated using standard photolithography techniques (indium tin oxide (ITO) thickness of 25nm) on borosilicate glass. A layer of SU8 having thickness of $\simeq 2\mu$m is fabricated on the IDT array to prevent dielectric breakdown. The thickness of the SU8 was measured using the stylus profilometer as described in section 2.3.

An interdigitated electrode array device which is capped with a SU8 layer was horizontally mounted in a sample holder in the optical set-up. It was connected with a voltage addressing unit as previously described in the section 2.2.1. A drop of 1-decanol (surface tension 28.4 mNm^{-1}, Dielectric constant 8.1, viscosity 0.113Nsm^{-2}) [105] was dispensed at the centre of the IDT array using the Gilsen 0.1-2μl micro pipette. It formed a spherical cap shape with a low contact angle of $5^o \pm 1^o$. It helps the oil droplet to spread at low voltage to a uniform film on which wrinkles were created. The contact angle is measured manually using Image J software by fitting the gradient at the three phase contact line. Schematic illustration of the 1-decanol droplet looking from y-direction and z-direction is shown in the figure 6.1, a and b at no voltage and voltage.

A 10 kHz square wave voltage was applied to each alternative electrode fringes in the coplanar strip electrode array and interposed electrodes were earthed hence a non-uniform electric field was created. In this non-uniform electric field a dielectric material, 1-decanol, experiences a dielectrophoretic force (explained in section 1.5) in the direction of high magnitude of electric field gradient. The electric field gradient is high in between the electrodes so the dielectrophoretic forces in these regions cause the oil to collect there preferentially, and in turn liquid from the region above of the electrodes are removed as shown in figure 6.1.C.

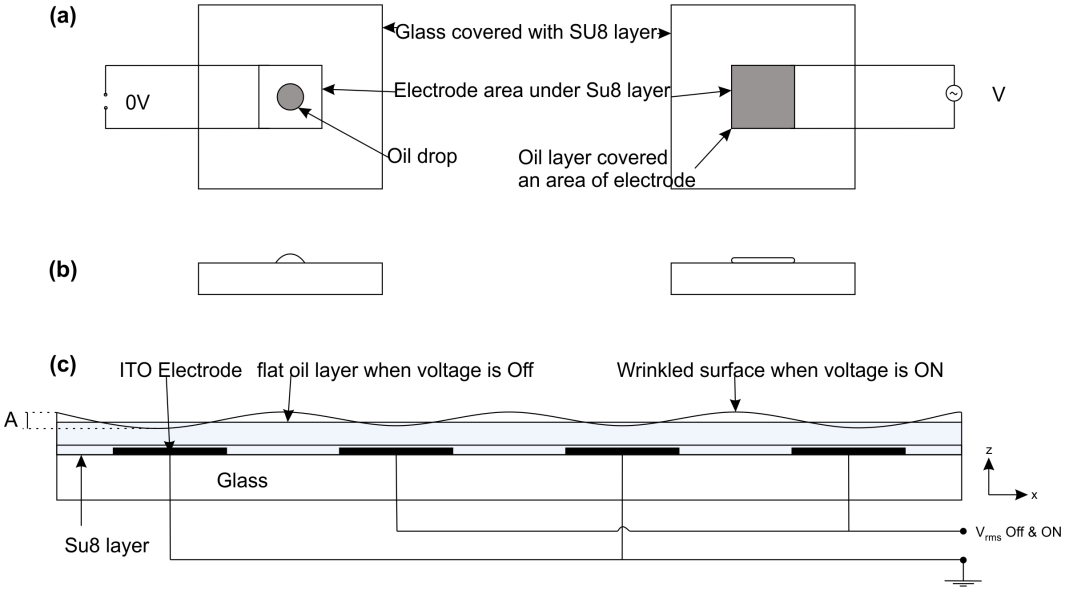

Figure 6.1: Schematic illustration of the device operation (a) top view of the oil droplet before voltage was applied to IDT array and oil covering an area of electrode array after voltage was applied, (b) side view of the droplet, (c) wrinkle formation at the oil and air interface.

Initially a drop of 1-decanol oil was dispensed on the IDT array, the 300V was applied to the IDT. Due to the dielectrophoresis, the droplet spreads and forms a thin layer. Therefore the oil was fully spread at 300V and then maintained by never going below 40V. The thickness is independent of the voltage but it was controlled by the initial volume using the Gilsen 0.1-2μl micro pipette. On the application of higher voltages an undulation was created at oil/air interface. The amplitude of the undulation depends on the voltage and liquid properties.

Laser light at a wavelength of 543nm illuminated the device in transmission and a series of diffraction spots resulted from the periodic variation in the thickness of the oil layer. 0^{th}, $1^{st}$and 2^{nd} order spots were recorded using three photo diodes as described in the section 2.6 and as shown in figure 6.2. The rest of the diffracted spots were ignored since the symmetry is exhibited between the $+1^{st}$ and -1^{st} diffracted orders. The intensities were recorded as a function of voltage and time.

The thickness of the oil layer was measured using a Mach - Zehnder interferometer. This comprises a He-Ne laser (633nm) divided into two beams at

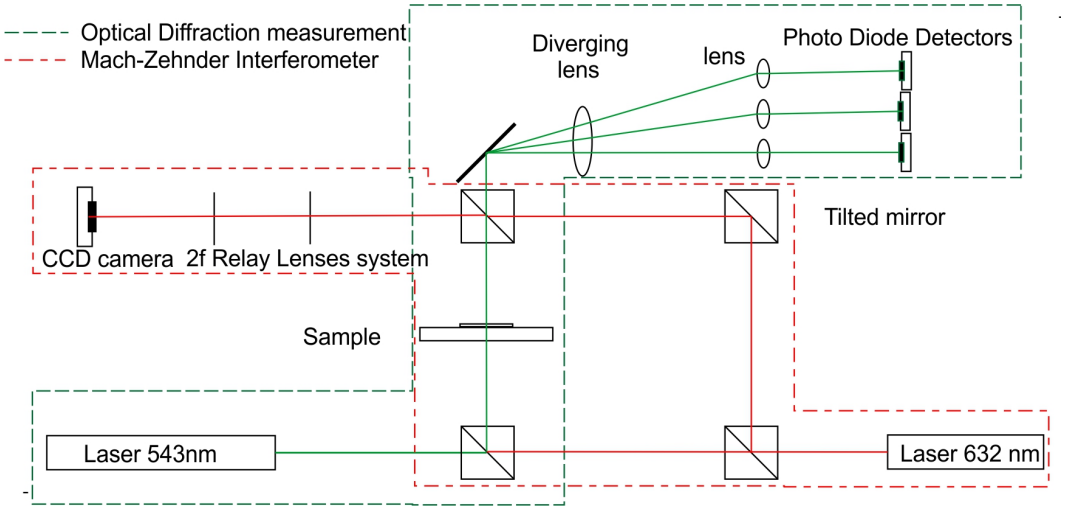

Figure 6.2: Schematic of the experimental salary for wrinkle dynamic measurement where optical diffraction measurement is carried out insitu in Mach-Zehnder interferometer.

first beam splitter and one beam is illuminated in transmission through the sample and other beam is reference beam. The two beams are recombined at the second beam splitter. One of the mirrors is tilted to produce parallel intensity interference fringes localized at the device. Due to the thin transparent oil layer the fringes are shifted in position. The thickness is measured by considering the periodic shift of the fringe as described in section 6.4.

6.3 Measuring the thickness of the oil layer

Figure 6.3 illustrates the principle to derive the surface height change in a model system by considering the different regions where a glass material has a thickness of h+d on the left side (region 1), and has a thickness of h on the right hand side (region 2). The image of the glass such as the fringe pattern of the glass is obtained from the Mach-Zehnder interferometer and referred as interferogram.

The optical path length (OPL) of the light is given in equation 6.1.

$$OPL = n.d \tag{6.1}$$

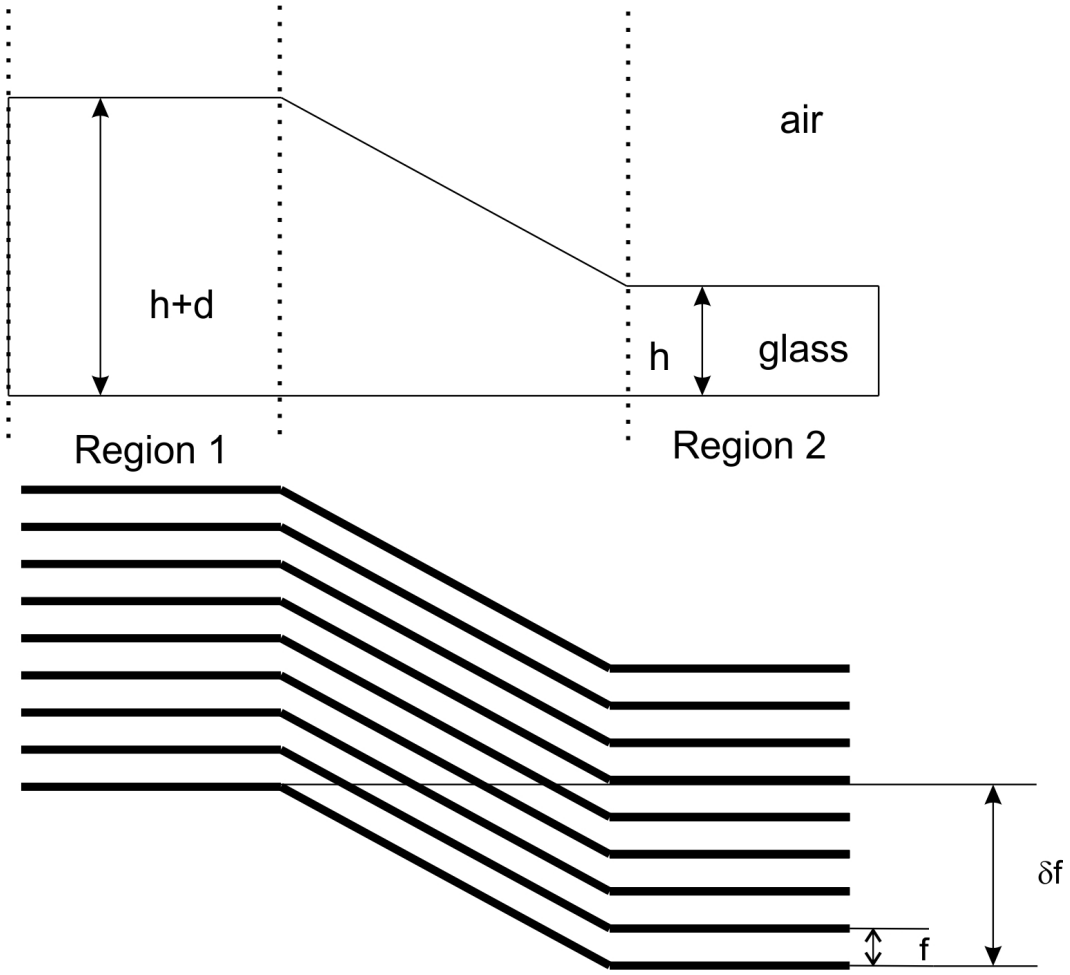

Figure 6.3: Schematic illustration of a glass with two different optical path lengths separated by a linear region and the resultant fringe pattern that would be obtained

where, n is the refractive index, d is the distance travelled through the material.

In region 1 in the figure 6.3, the light travels through the glass having distance of h+d is giving the optical path length (OPL1) in equation 6.2.

$$OPL1 = n_{glass}.(h + d) \tag{6.2}$$

where OPL1 is optical path length in region 1. In region 2 in the figure 6.3, the light travels through the glass having the distance of h and through the air having a distance of d is giving the optical path length (OPL2) in equation 6.3.

$$OPL2 = (n_{glass}h + n_{air}d) \tag{6.3}$$

The optical path difference (OPD) causes the fringe displacement of δf in the interferogram as shown in the figure 6.3.b.

$$d(n_{glass} - n_{air}) = m\lambda \tag{6.4}$$

Where, m is the phase shift (m=$\frac{\delta f}{f}$), f is the width of the fringe and δf is the fringe displacement.

Therefore;

$$d = \frac{\delta f}{f}\frac{\lambda_{air}}{(n_{glass} - n_{air})} \tag{6.5}$$

Hence it is possible to measure the corresponding change in thickness of the material, the additional thickness in the region 1, by considering the fringe displacement in the interferogram and refractive index of the material.

The thickness of the transparent oil layer, 1 decanol oil, on the interdigitated electrodes was obtained by analysing the interferograms which were taken in a position at the edge of the electrodes. Figure 6.4 shows an interferogram of a 1

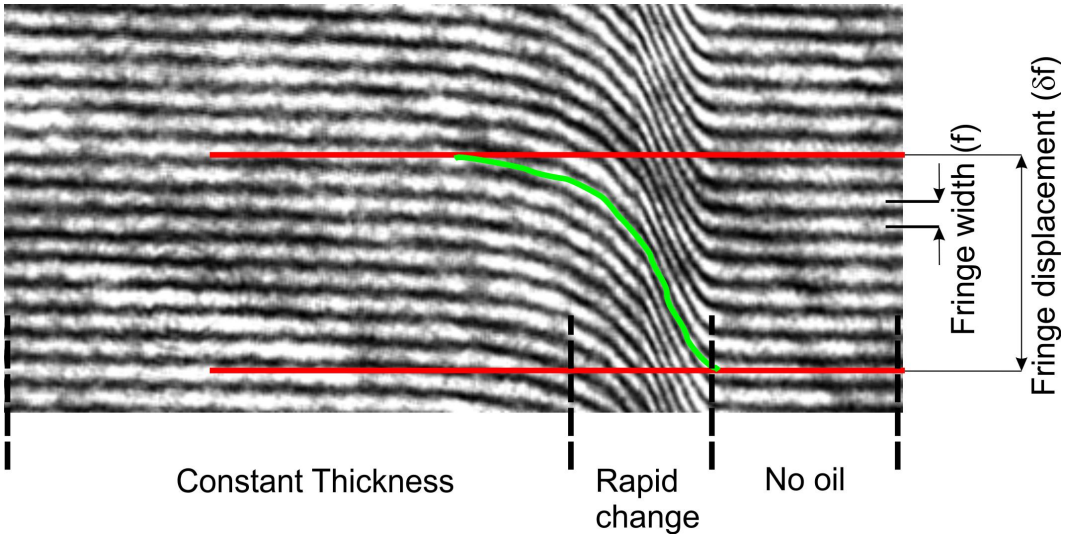

Figure 6.4: Image, interferogram, illustrates the edge profile of a 1-decanol layer on the interdigitated electrodes which was covered with a 2μm and a 100V were applied to the IDT array.

decanol oil layer having a thickness of h on the IDT electrode where a 100V is applied to the electrodes. On the right hand side of the figure 6.4, it does not contain the oil (just plain SU8 surface) and it is just next to the last electrode in the electrode array. A rapid change area where the oil is rapidly increasing in the thickness and it is between the no oil area and with a constant oil thickness area. The fringes in the rapid change area are seen to bend uptowards of the picture. After rapid change area, the oil obtains a constant thickness as shown in figure 6.4.

The width of the fringe and fringe displacement were obtained by image processing. The fringe displacement was measured by following a single fringe from no oil region to the constant thickness region. The transition must be narrow enough to follow a single fringe. Results of this analysis for figure 6.4, fringe width is f=14.3 pixels and fringe displacement is δf=386.2 pixels. Therefore the thickness of the 1-decanol layer is 24.6μm with knowledge of λ=632.8nm and $n_{1-decanol}$=1.438.

6.4 Quasi-static measurement

To investigate the wrinkle evolution as a function of applied voltage, initially a droplet of 1-Decanol (Dielectric constant 8.1, viscosity 0.113 NsM^{-2} and surface tension 28.4 mNm^{-1}) [105] was dispensed on the center of 40μm line width IDT electrode array which was coated with a 2μm SU8 layer. The device was mounted in sample holder and then a 10 kHz square wave (300V) was applied to the device as previously described. The edge profile of the layer was captured using Mach-Zehnder interferometer and then the uniform oil layer thickness was obtained by image processing as previously described.

A 10 kHz square wave, which is modulated with another 1Hz triangle wave, was applied to the IDT array therefore the voltage was linearly increased and decreased. The minimum voltage was 42V and the maximum voltages (304V, 278V, 257V, 230V, 212V, 193V, 160V and 127V). A low voltage (42V) was applied to keep the oil spread as a thin uniform film and high voltage was applied to achieve the high amplitude. The voltage modulation causes the amplitude of the wrinkle to increase and decrease gradually and monotonically. Whilst a laser, 543nm wave length, was illuminated in transmission through the centre of the IDT array it created a series of the diffraction patterns. Zero, first and second order spots of the diffraction pattern were recorded (and the rest of the spots are blocked) as a function of voltage.

The intensities of the 0^{th}, 1^{st} and 2^{nd} order is shown in the figure 6.5 where the voltage is linearly increased from 42V to 305V and the thickness of the oil layer is 19.5μm. The zero order spot decreases with increasing the voltage whilst the first and second order spots increase to a maximum as shown in figure 6.5. Figure 6.5 shows the intensities of the zero, first and second diffracted orders as a function of voltage. The solid lines are the theoretical prediction by the square of a 1^{st} kind of the Bessel function, the Fraunhofer diffraction pattern for a thin sinusoidal phase grating, $J_q^2(\alpha V^2)$ where q represents the diffracted order [71].

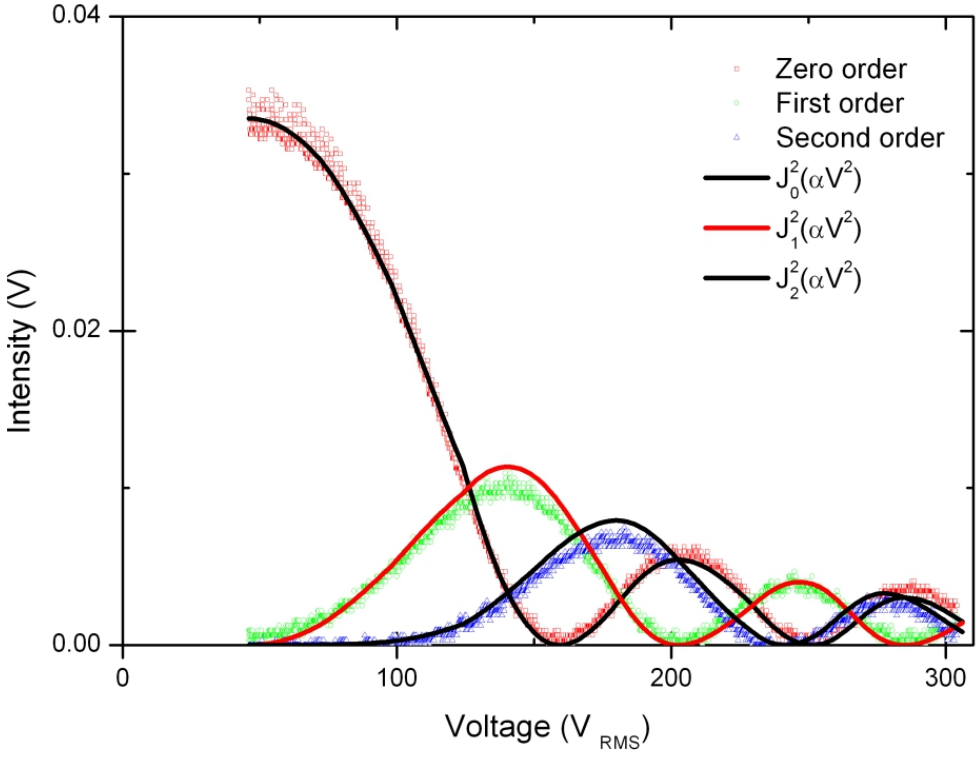

Figure 6.5: Graph showing the fitting of the square of the Bessel function (as predicted by Fraunhofer thin sinusoidal grating theory) to the intensities of the zero, first and second transmitted orders which were recorded while the voltage was increased from 42V to 305V.

The data has shown that the ratio of the intensity of the first order first peak to the zero order first peak is 31% which is similar to the Fraunhofer approximation for a thin sinusoidal phase grating of 38%. This fitting has been done by manual method using interpolation in MS excel and then m (phase delay) value and voltage are extracted at regular intervals where m is directly proportional to the wrinkle amplitude [18, 49] .

This experiment was repeated with the same liquid layer at different maximum

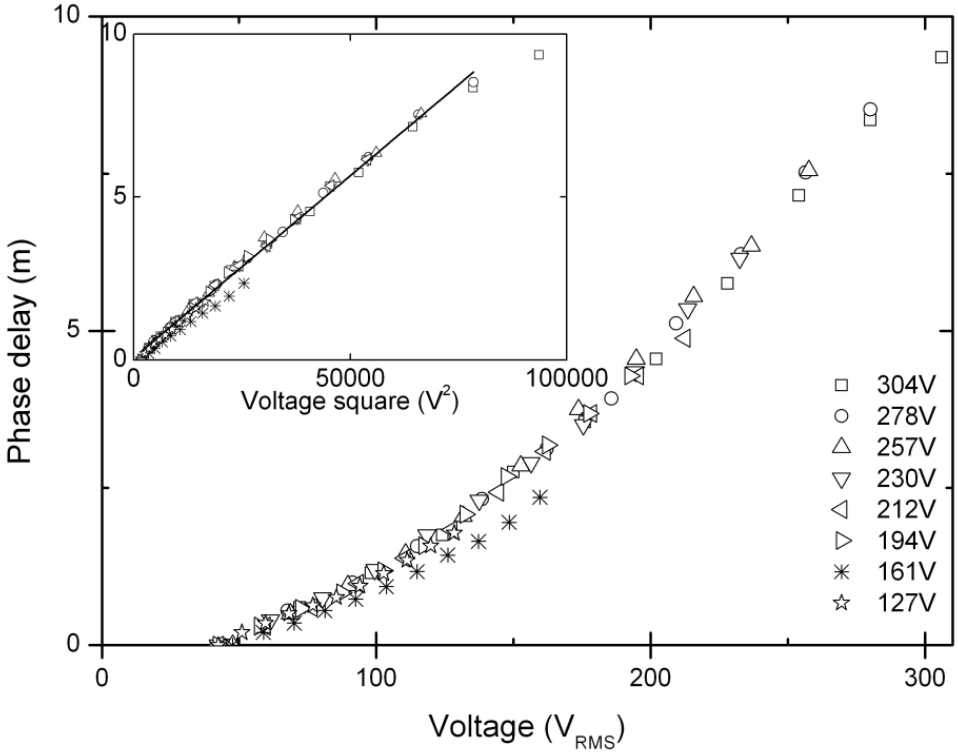

Figure 6.6: Graph showing phase delay m radians as a function of applied voltage for 8 maximum voltages (in the figure the maximum voltage represents the voltage increased from 42V to maximum voltage and x-axis represents the ramping of the voltage from minimum to maximum) and inset picture shows the linear relation between the phase delay and voltage square for an initial thickness of the oil layer is 24.2μm.

voltage (for example 280V, 258V, 232V, 212V, 198V, 160V and 128V) and minimum voltage is maintained at 42V to keep liquid within the electrode area. The m value as a function of voltage was extracted for each voltage and shown in figure 6.6. In the figure 6.6, the voltage represents the RMS voltage in the exper-

iment.

It has been shown has shown in literature that the amplitude should be high at the higher voltages [17, 18]. Our data has shown similar behaviour for example at 304V the m is 9.4 radians and at 127V the m is 1.9. As expected the m values of the each voltage is laid on each other (shown in the figure 6.6) because of the optical path length is increased with respect to the voltage. Therefore the data concluded that the amplitude depends on the applied voltage. Inset picture of the figure 6.6 shows the phase delay (m) is proportional to the voltage square, $m = (11.3 \times 10^{-5})V^2 + 0.112$, which is consistent with the linear relationship between amplitude (A) and voltage squared (V^2) [17, 18]. We were not intended to repeat but different method to measure the phase delay which should be proportional to the amplitude of the wrinkle.

6.5 Dynamics of Relaxing and Switching

6.5.1 Experimental details

The same experimental set-up, as previously described in section 6.5, was used to investigate the switching and relaxation time of the wrinkles. A discontinuous square wave modulation voltage instead of the triangular modulation wave was applied to the IDT electrode array therefore when a liquid is subjected to this field the wrinkles are evolved and decayed. A schematic illustration of the wrinkle evolves and decays with respects to time as the voltage switched between maximum and minimum is shown in figure 6.7.

After the uniform layer of a 1-decanol oil created by applying a 300V to the IDT electrode array, a AC square wave having a frequency of 2.5 kHz which was modulated with another 100Hz square wave was applied to each alternative electrode and interposed electrodes are earthed hence the voltage was discontinuously switched between the maximum and minimum amplitude of the voltage for every

Electrode geometry (width of the electrodes)	Thickness of the oil
20μm	12.6μm
40μm	13.4μm, 17.2μm, 21.1μm, 24.6μm
80μm	22.3μm, 26.1μm

Table 6.1: Table shows that experiments were performed on Different electrode geometry with different thickness of the oil

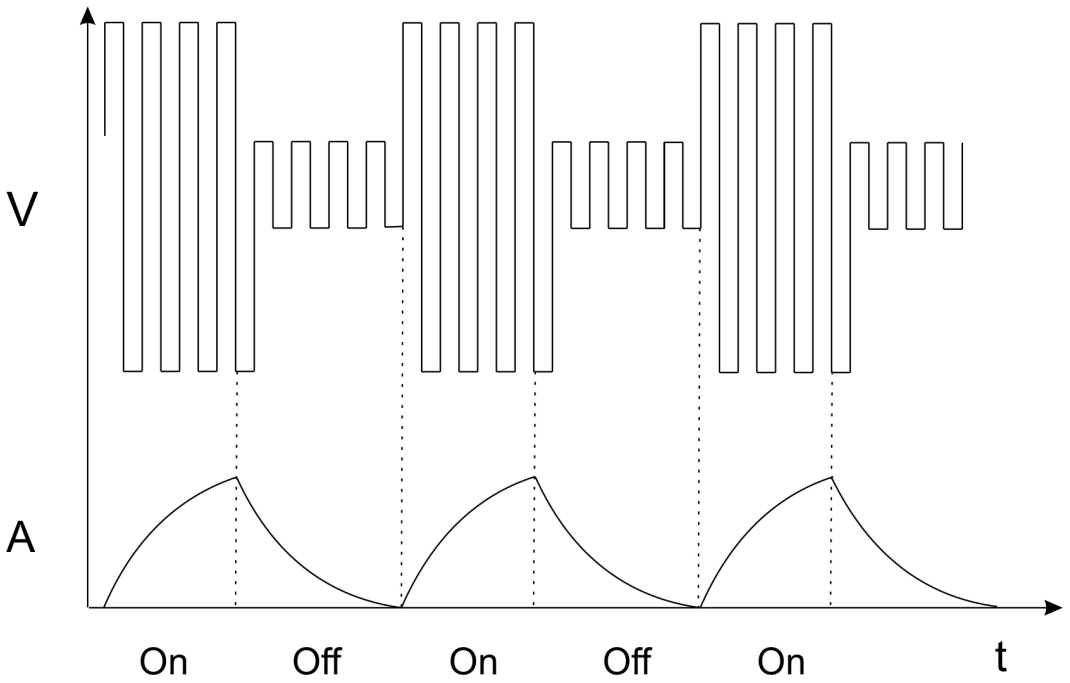

Figure 6.7: Figure showing the schematic illustration of the switching and relaxation of the wrinkle by applying a square wave (2.5 kHz square wave is modulated with an another 100 Hz square wave) voltage.

10msec. In this case the minimum voltage is 42V and maximum voltages are 305V, 280V, 258V, 232V, 212V, 198V, 160V and 128V. A minimum voltage is applied to keep the oil spread as a thin film and the maximum voltage is applied to achieve the wrinkles.

The thickness of the 1-decanol layer was obtained using the Mach-Zehnder interferometer. The intensities of the 0^{th}, 1^{st} and 2^{nd} diffracted spots as a function of time for switch on and switch off condition were captured. The switching On and Off experiments were performed on the same liquid layer. The thickness of the oil was measured at 304V, 232V and 160V respectively for each liquid volume used and it reduced from one voltage experiment to another due to the oil evaporation. The initial thickness of the oil layer are given in the table 6.1.

6.5.2 Modelling the undulation relaxation

Figure 6.8 shows a schematic diagram of static wrinkles at the oil/air interface with the pitch of the wrinkle which is double of the electrode width (p=2d). The wrinkles are static and stable at constant voltage.

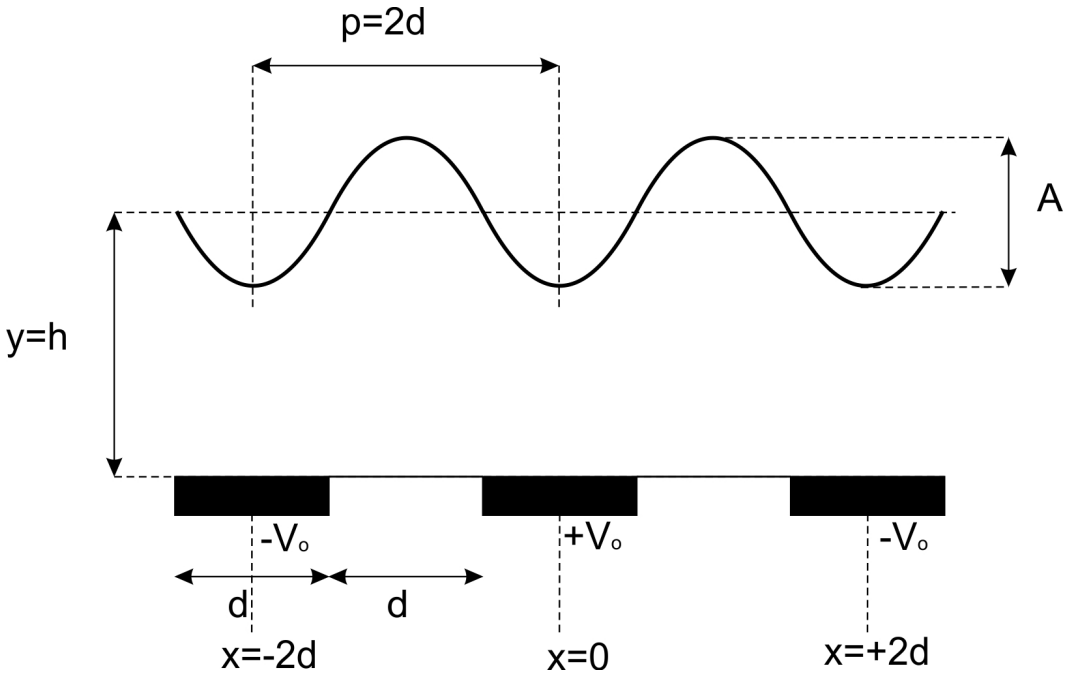

Figure 6.8: Schematic illustration of the static wrinkle array at oil/interface.

An overall pressure distributed [19] at the film surface is given in,

$$p = p_o - \gamma \frac{\partial^2 y}{\partial x^2} + p_{el} \tag{6.6}$$

Where, p_o is an atmospheric pressure, $\gamma \frac{\partial^2 y}{\partial x^2}$ is the Laplace pressure from the surface tension of the oil and p_{el} is the electrostatic pressure for a given electric field.

The modulation of y gives rise to a lateral pressure gradient inside the film including a Poiseuille flow j given by:

$$j = \frac{y^3}{3\eta} \left(\frac{\partial p}{\partial x} \right) \tag{6.7}$$

Where η is the viscosity of the liquid. A continuity equation enforces mass

conservation of the incompressible liquid [19].

$$\frac{\partial j}{\partial x} = -\frac{\partial y}{\partial t} \tag{6.8}$$

In switch off condition, the voltage is suddenly removed hence the surface wrinkle amplitude decays exponentially with time. A functional form which satisfies the equations with ρ_{el}=0 (and the assumption is discussed below) 6.6 to 6.8 is

$$y = h - \frac{1}{2}Acos(2k_1x)exp(-t/\tau) \tag{6.9}$$

Where A is the amplitude of the wrinkle and k_1 is the wave number (k_1=π/p). Since the voltage has been removed the only contribution to the pressure is the Laplace pressure from the surface tension and the effect of the gravity and atmospheric pressure is ignored.

$$p = -\gamma\frac{\partial^2 y}{\partial x^2} \tag{6.10}$$

The pressure equation is substituted in the Poiseuille flow equation, and resulting of equation 6.11.

$$j = \frac{y^3}{3\eta}\left[-\frac{\partial}{\partial x}\left(-\gamma\frac{\partial^2 y}{\partial x^2}\right)\right] = \frac{y^3}{3\eta}\left[\gamma\frac{\partial^3 y}{\partial x^3}\right] \tag{6.11}$$

Substituting the Poiseuille flow equation in the continuity equation and make the assumption that A $\ll$ h and so y $\approx$ h for the continuity equation:

$$\frac{\partial j}{\partial t} = \frac{y^3}{3\eta}\left[\gamma\frac{\partial^4 y}{\partial x^4}\right] \tag{6.12}$$

Substitute the differential terms in the equation 6.12 which results in equation 6.13

$$\frac{A}{2\tau}exp(-t/\tau)cos(2k_1x) = \frac{\gamma h^3}{6\eta}A(2k_1)^4exp(-t/\tau)cos(2k_1x) \tag{6.13}$$

Therefore;

$$\tau = \frac{3\eta p^4}{16\gamma h^3 \pi^4} \tag{6.14}$$

Equation 6.14 shows that switch off is faster by selecting an oil with a higher surface tension or a lower viscosity and thinner electrodes and gaps. This equation also shows a linear relationship between the τ and $\left(\frac{p^4}{h^3}\right)$.

6.5.3 Dynamics of relaxation

Figure 6.9 shows the intensities of the 0^{th}, 1^{st} and 2^{nd} diffracted order spots as a function of time, where the voltage is dropped from a maximum of 304V to a minimum of 42V and the thickness of the oil layer is 17.2μm. The intensities of the diffracted orders were varied between maxima and minima as the amplitude is reduced. As previously described the actual data was fitted with a theoretical prediction, square of the Bessel function of the first kind, to show amplitude of the wrinkle consistent with thin sinusoidal phase grating theory. This assumes that the wrinkle profile was a pure sinusoidal during the relaxation process. The m values of the peaks and troughs of the 0^{th}, 1^{st} and 2^{nd} orders of the Bessel function are given in the table 6.2. The times of the peaks and troughs of the 0^{th}, 1^{st} and 2^{nd} orders were obtained from the actual data (figure 6.9) and the m (phase delay) values of the peaks and trough for J_0, J_1 and J_2 were obtained from the table 6.2.

This experiment was also repeated with different maximum voltages such as 278V, 257V, 230V, 212V, 194V, 161V and 127V where the minimum voltage was 42V for each experiment. For each voltage experiment, the m value and time were obtained as described above. The thickness was measured at 304V, 230V and 160V and they are 17.2μm, 16.4μm and 15.2μm respectively. The thickness was not constant in these experiments which led the change in wrinkle amplitude. The wrinkle on the surface of the oil decays with time dependence that was fitted by the functional form $m = m_o e^{(t/\tau)}$ where t is the actual time and τ is the switch

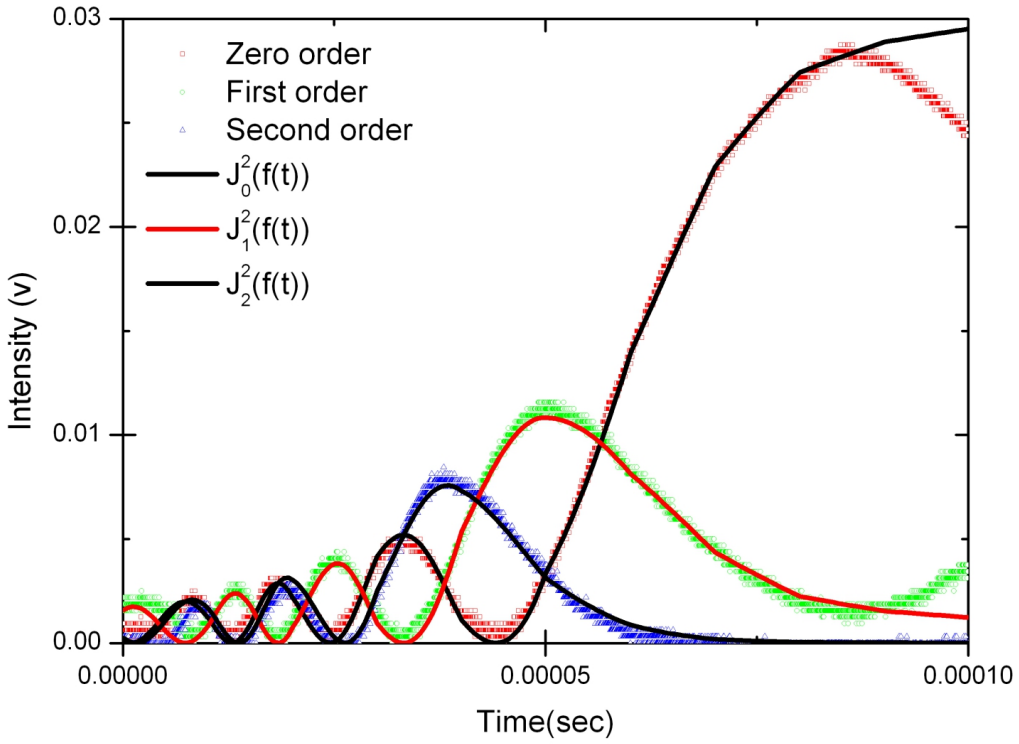

Figure 6.9: Graph shows the intensities of the zero, first and second order of the diffracted patterns as the amplitude of the wrinkles was suddenly reduced due to the voltage switching off. The solid lines are fits to square of the Bessel function of the 1st kind of order 0^{th}, 1^{st} and 2^{nd}.

	J_0	J_1	J_2
1^{st} peak		1.84	3.05
1^{st} trough	2.41	3.83	5.14
2^{nd} peak	3.83	5.33	6.71
2^{nd} trough	5.52	7.02	8.42
3^{rd} peak	7.02	8.54	9.97
3^{rd} trough	8.65	10.17	11.62
4^{th} peak	10.17	11.71	13.17
4^{th} trough	11.79	13.32	14.8
5^{th} peak	13.32	14.86	16.35
5^{th} trough	14.93	16.47	17.96

Table 6.2: Table shows m values of the peaks and troughs of the Bessel function.

off time. Therefore, in order to obtain the m_o and τ, the exponential form was simplified to a linear equation and given in equation 6.15.

$$ln(m) = -t/\tau + ln(m_o) \tag{6.15}$$

Then τ was determined from the linear fit between the natural logarithm of the phase delay and time for each voltage.

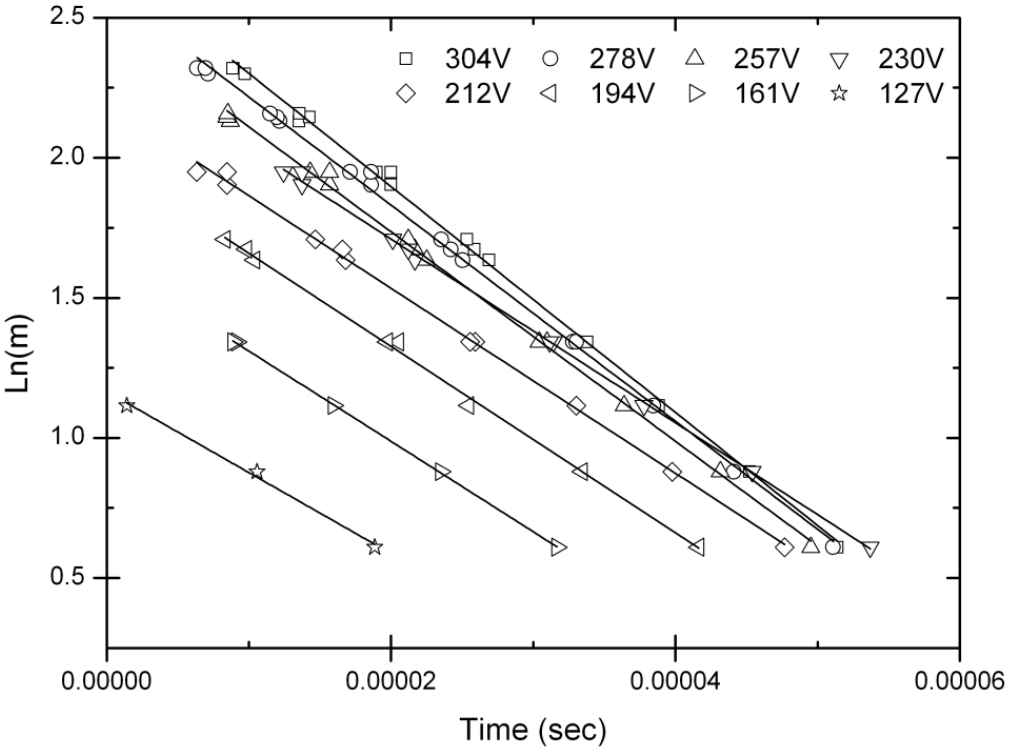

Figure 6.10: The natural logarithm of the phase delay (m) as a function of time which were obtained from the times of the peaks and troughs in the 0^{th}, 1^{st} and 2^{nd} orders using table 6.2. The maximum voltage represents the voltage was stepping off from maximum voltage (127V, 161V, 194V, 212V, 230V, 257V, 278V and 304V) to minimum voltage (40V).

Figure 6.10 shows the natural logarithm of m value as a function of time for each voltage. In the linear equation, the intercept is ln(m_o) and the gradient is $1/\tau$. Linear curves have yielded an average standard error of 2% in the switch off time. The relaxing time, switch off, of different voltages (304V, 278V, 257V, 230V, 212V, 193V, 160V and 127V) on the 40μm line width are 24.8μsec, 25.9μsec,

26.7μsec, 30.5μsec, 30.3μsec, 30.1μsec, 31.0μsec and 34.6μsec respectively for the initial thickness of 17.2μm.

The switch Off experiments with 1-decanol oil layer were repeated on 20μm,

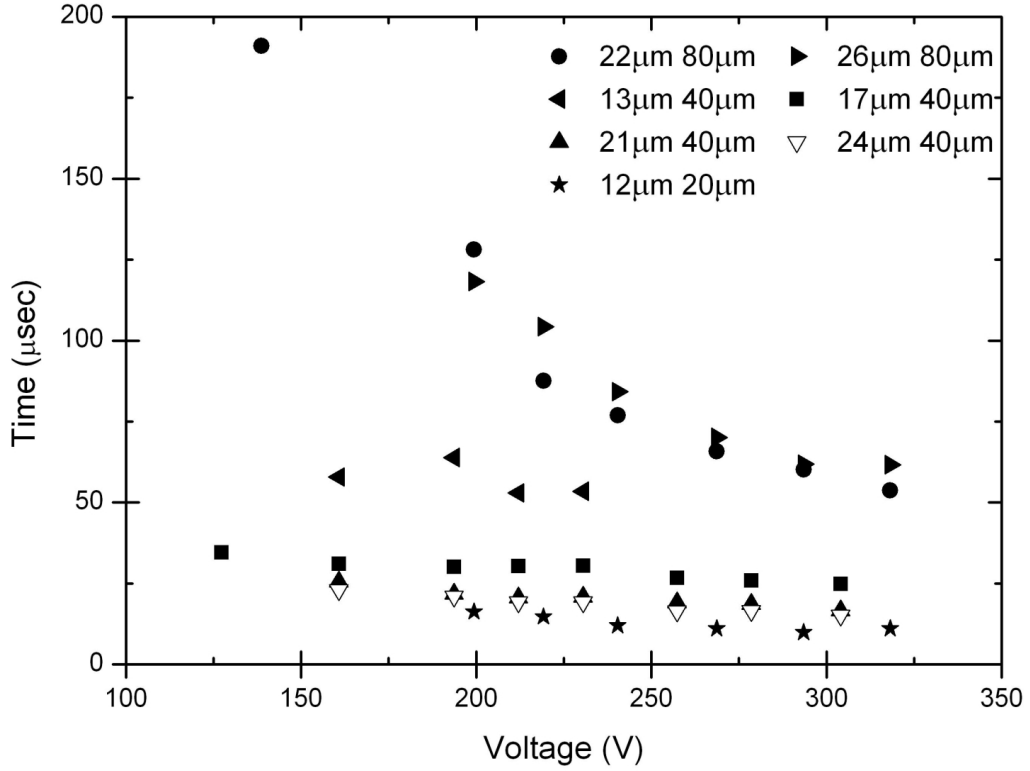

Figure 6.11: The switch off time (which were obtained from the gradients of the Ln(m) and time) of the wrinkles as a function of the applied voltage, thickness of the oil layer and width of the electrode line.

40μm and the 80μm line width of the IDT electrode arrays for a range of initial volumes/thicknesses. The initial thickness of the oil layer was controlled using the Gilsen 0.1 - 2μm micro pipette. The switch off time was measured for each experiment using the procedure described above. Figure 6.11 shows the Switch off time for 20μm, 40μm and 80μm electrode width and different oil layer thickness as a function of voltage.

The τ for the each voltage would be constant only if the layer thickness was unchanged during the experiments since it depends on the restorative force which is limited by the surface tension and viscosity of the oil. The oil was evaporated as the experiments were performed and the voltage was reduced. The only thickness

Line width	Thickness (Run1 to Run8)	Switch off time (Run1 to Run8)
80μm	22.5μm to 20.1μm	53.7μsec to 191.1μsec
40μm	17.2μm to 15.2μm	24.8μsec to 34.6μsec
20μm	12.5μm to 9.5μm	11μsec to 16.2μsec (run6)

Table 6.3: Data for the figure 6.11

measurements were taken at 304V, 239V and 160V and the rest of the thickness were estimated at each voltage using linear interpolation to produce figure 6.12. Due to the oil evaporation, the τ is increased as the voltage is reduced and they are given in the table 6.3.

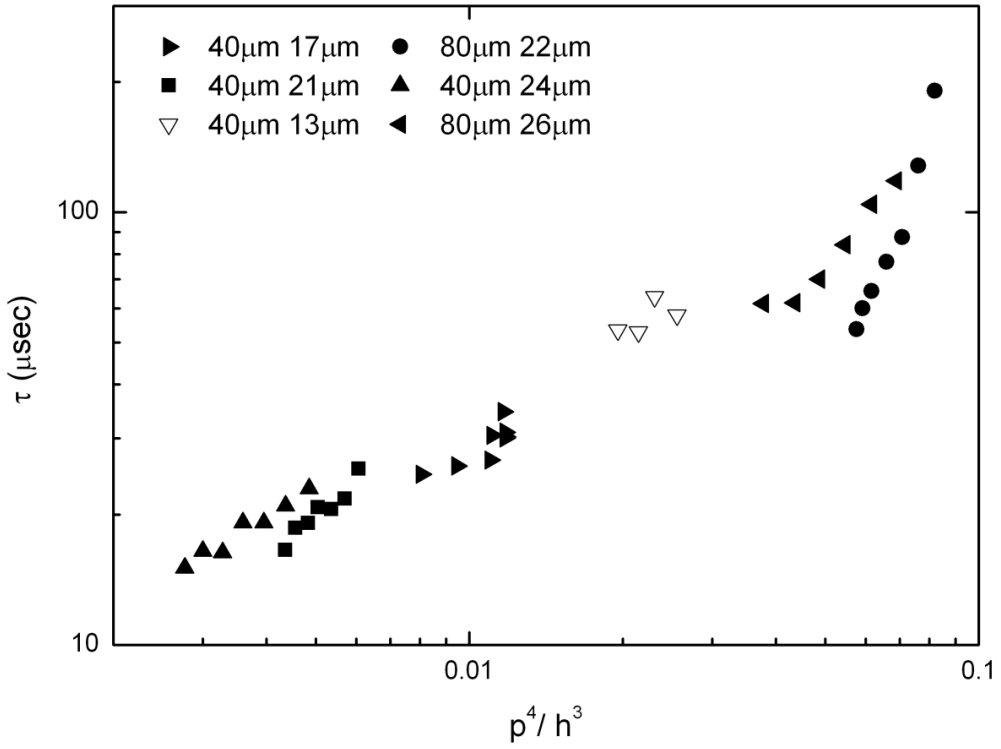

Figure 6.12: Indicative plot of τ versus p^4/h^3 for all the data on 1-decanol oil.

The data is gathered from the dynamic switch off measurement of 1-decanol for each oil thickness and line width of the electrode array are plotted in the figure 6.13 where the data are plotted as τ versus p^4/h^3. It shows that as the thickness of the oil layer reduces the τ increases. However the scaling relationship for 1-decanol oil have been shown the τ dependencies on the particular parameters such as thickness of the oil layer and line width of the electrodes.

There is a correlation between the τ and p^4/t^3. This preliminary work needs repeating with more careful monitoring/control of thickness.

6.5.4 Dynamics of switching

The dynamic switching experiments were performed as previously described in section 6.7.1. In switching experiments the applied voltage was switched from minimum voltage (42V) to maximum voltage (305V) and wrinkles are evolved at oil/air interface. The amplitude of the wrinkle depends on the applied voltage. Figure 6.13 shows the intensities of the 0^{th}, 1^{st} and 2^{nd} order spots as a function of time where the voltage is switched from 42V to 304V and the initial thickness of the 1-decanol oil layer is 17.2μm. The solid lines are the square of the first kind of the Bessel function $J_q^2(f(t))$.

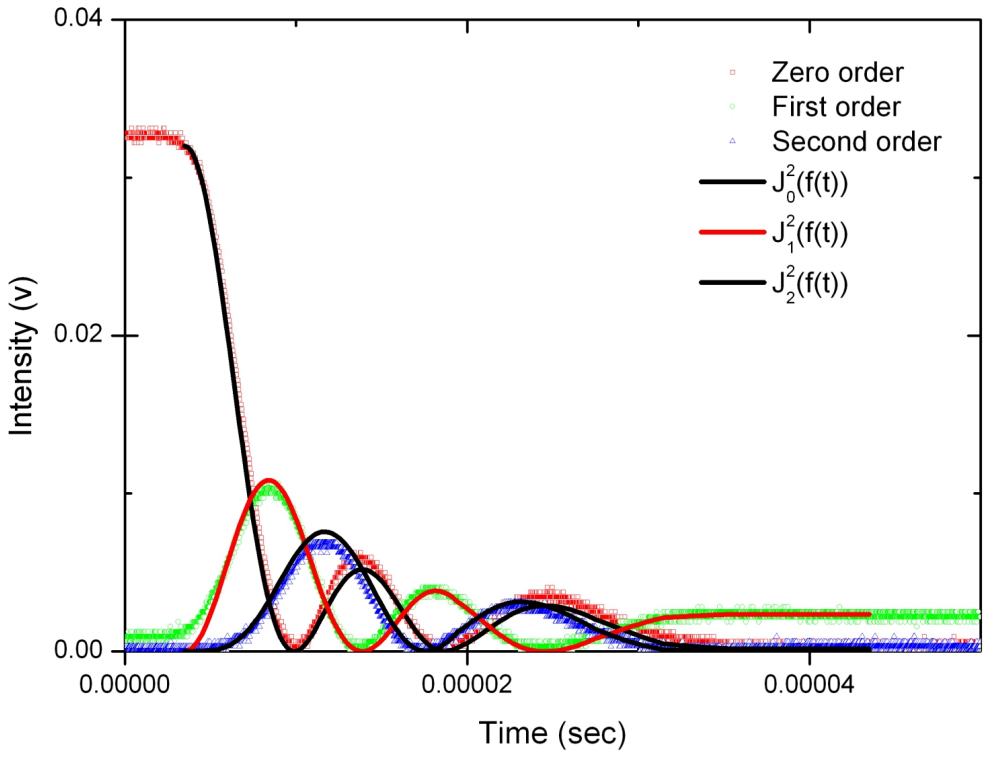

Figure 6.13: Graph showing the fitting of the Bessel function to the zero, first and second diffracted orders after switching ON the voltage.

The 0^{th} order intensity is decreased whilst the 1^{st} and 2^{nd} order spots intensi-

ties increased and the intensities are varied between maxima and minima as the amplitude of the wrinkle is increased. As previously described in the section 6.7.1 the actual data (intensities of the diffracted spots) was fitted with a theoretical prediction (the Fraunhofer approximation) to show amplitude of the wrinkle consistent with thin sinusoidal phase grating theory. This assumes that the wrinkle profile is a pure sinusoidal during the switching process. The times of the peaks and troughs of the 0^{th}, 1^{st} and 2^{nd} orders were obtained from the actual data (figure 6.9) and the m (phase delay) values of the peaks and trough for J_0, J_1 and J_2 were obtained from the table 6.2. Experimental data have shown that the ratio of the intensity of the first order (first peak) to the 0th order (first peak) is 31% which is similar to the Fraunhofer approximation for a thin sinusoidal phase grating is 38%. .

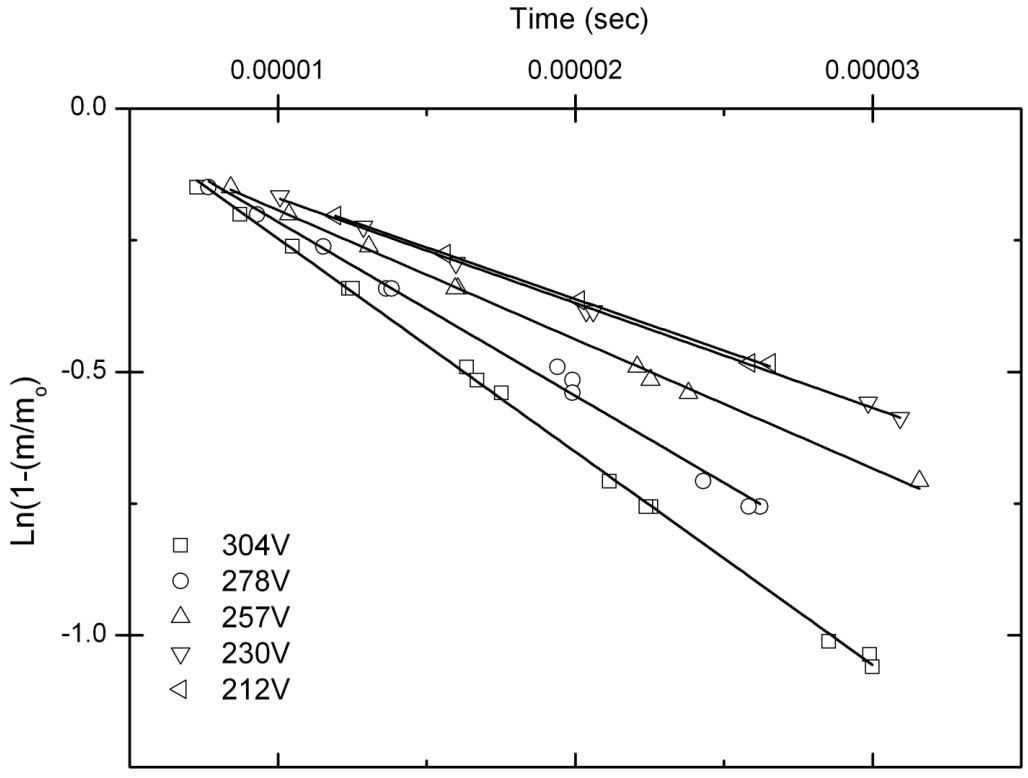

Figure 6.14: Data shows the $ln(1 - m/m_o)$ as a function of the time at different applied voltages. The maximum voltage represents the voltage was switching from minimum voltage (40V) to maximum voltage (127V, 161V, 194V, 212V, 230V, 257V, 278V and 304V).

This experiment has also been repeated on the same oil layer with different maximum voltages such as 278V, 257V, 230V, 212V, 194V, 161V and 127V where the minimum voltage is 42V. For each voltage experiment the m value and time of the peaks and troughs of the 0^{th}, 1^{st} and 2^{nd} orders were obtained as previously described in section 6.6.3.

The thickness was measured at 304V, 230V and 160V and they are 17.2μm, 16.4μm and 15.2μm respectively. The thickness of the oil layer is reduced between 278V and 127V by 12% due to the joule heat from the device or from the atmospheric temperature.

The phase delay (m) is directly proportional to the amplitude of the wrinkle [17, 49]. The following relationship of the form $m = m_o(1 - e^{(t/t_{on})})$ where t is the actual time and t_{on} is the switching time was used to model/fit the time dependence of the phase delay. The exponential form was simplified to a linear equation.

$$ln(1 - m/m_o) = t/t_{on} \tag{6.16}$$

The t_{on} is determined from the linear fit between the natural logarithm of the $(1 - m/m_o)$ and time for each voltage. The best fits were obtained by adjusting the m_o values and this was adjusted to minimize the error of the gradient. The linear equation gives the t_{on} from 1/gradient and $ln(m_o)$ from the intercepted.

Figure 6.14 shows the $ln(1 - m/m_o)$ values as a function of time at different voltages and exponential fit. The t_{on} at different voltages (304V, 278V, 257V, 238V and 212V) on the 40μm line width are 24.7μsec, 18.8μsec, 27.1μsec, 32.7μsec and 36.5μsec respectively for the oil thickness of the 17.2μm.

This experiment was repeated on the three different electrode line width (20μm, 40μm and 80μm) and different initial oil thickness layers ranging from 17.2μm to 24.5μm. Figure 6.15 shows the switching times of the same oil layer at different voltages for 40μm and 80μm line width of IDT electrodes. The t_{on} is increased

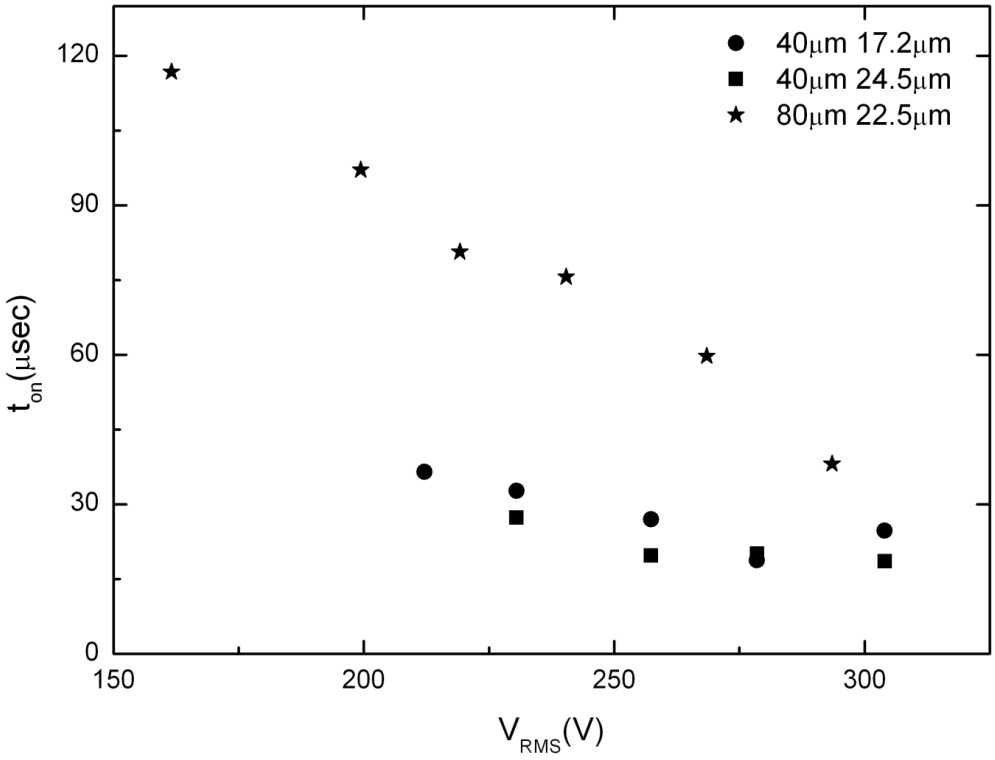

Figure 6.15: Graph shows the switch on time of the wrinkles as a function of applied voltage, thickness of the oil layer and width of the electrode line.

as the experiments are repeated by changing the RMS voltage (from 304V to 127V with around 25V steps) on the same oil layer. The data illustrates that the t_{on} depends on the line width of the electrode and the thickness of the oil layer. Switching of the lower pitch wrinkle is faster than the higher pitches and is shown in the figure 6.15.

6.6 Conclusion

We have demonstrated how to create a uniform thin layer of 1-decanol oil by placing a small droplet of 1-decanol oil on the interdigitated electrode array, which is coated with 2μm SU8 layer, and applied a AC voltage across the electrodes which allows the droplet to draw into a thin film. The thickness of the oil is independent of the applied voltage. On the application of higher voltages the wrinkles were created at oil/air interface because of dielectrophoresis. The quasi-static exper-

iment has demonstrated the amplitude of the wrinkle increased as the voltage increases. Data has shown that the phase delay is directly proportional to the applied voltage squared where the phase delay is proportional to the amplitude of the wrinkle.

To investigate the switching characteristics of the wrinkle, a 2.5kHz square signal which is modulated with another 100Hz square signal, is applied to IDT. This modulation causes the amplitude of the wrinkle to discontinuously switch between the flat and wrinkled surface where the peak to peak amplitude depends on the applied voltage and liquid properties such as surface tension, viscosity and dielectric constant.

Data has shown that the switch on and switch off time depends on the line width and thickness of the oil layer, for example switching and relaxation of lower pitch electrodes are faster than the higher pitch. The switch off time has been theoretically derived by considering the whole pressure on the system. The experimental has shown a correlation between the τ and p^4/h^3.

6.6.1 Concluding remarks

A mathematical approach of the switching is required to conclude the switching results.

The oil evaporation should be avoided to get the consisted results or the thickness of the oil should be measured for every repetition.

Chapter 7

Conclusion

7.1 Dielectrowetting

7.1.1 Statics

Our approach has been shown the wetting and de-wetting of a 1, 2 propylene glycol droplet on a interdigitated electrode (IDT) array, which is capped with a hydrophobic SU8 layer, and wetting is controlled in a voltage manner. When the voltage is applied to the electrodes it creates a non-uniform electric field and exponential decayed with penetration depth. In this case the penetration depth is much smaller than height of the liquid.

A prediction of dielectrowetting, the relationship between the cosine of the contact angle and voltage square, was derived by considering the three phase contact line shift which due to dielectric energy stored in the liquid. The dielectrowetting equation describes how the liquid dielectrophoresis (L-DEP) modifies the wetting property of the liquid which is similar to the EWOD prediction [81]. In our prediction the dielectrowetting strength depends on the liquid properties and the penetration depth which is defined by the periodicity of the electrodes, but in EWOD prediction the wetting strength depends on the dielectric layer thickness.

Wetting and de-wetting has exhibited with a hysteresis of $\sim 10^o$ and shown the ability to spread the droplet over wide contact angle range (70^o). No spreading or leaking across the electrode array was observed due to periodicity of the electrode geometry and it referred as an anisotropic spreading. The experimental results has been shown the cosine of the contact angle simple follows voltage square law [81]. Data has illustrated that the dielectrowetting energy is controlled by selection of the electrode pitch.

The different types of electrode geometry, such as radial and 0-offset, were introduced to produce isotropic wetting and dewetting. The wetting and dewetting is exhibited with a hysteresis of $\sim 10^o$. However the data has not followed the dielectrowetting prediction due to the electrode geometry;

(i) The periodicity of the electrodes is increased from region to another region in radial electrodes. Therefore strength of dielectrowetting is unequal in the geometry.

(ii) The θ was reduced in quantised steps as the voltage increases due to the energy barriers in the 0-offset geometry.

A preliminary investigation has shown the droplet wetting and dewetting in another liquid with a hysteresis of 0^o where the dielectric constant of the droplet is much higher than another liquid. The droplet was 1, 2 propylene glycol and another liquid was hexadecane. The data has shown that the ability to spread the droplet over wide contact angle range (135^o). It has shown that the cosine of the angle follows voltage square law.

7.1.2 Dynamics

We have investigated the dynamics of the wetting and dewetting of a 1, 2 propylene glycol on the IDT array a line width of 40μm which is coated with a 0.85μm hydrophobised SU8 layer and wetting is controlled by applying an AC voltage to the IDT electrode array. This investigation has shown that how the contact angle and contact width evolves as a function of time at different fixed voltages. The super-spreading has been illustrated without adding any surfactant in the liquid or changing the surface topography [85]. Our approach, voltage induced spreading, is complementary to the surface topographic modification or liquid modification such as adding a surfactant to the liquid.

The theory of voltage induced dynamic wetting has been derived using a modified Hoffman de Gennes law [85] for stripe spreading. It has demonstrated the three distinct spreading regime and spreading laws such as;

(i) Partial wetting (V$\ll V_{Th}$): the contact angle and contact width of the droplet is exponentially approached to equilibrium shape with time.

(ii) complete wetting (V$\simeq V_{Th}$): the dynamic contact angle is decreased ac-

cording to a -2/7^{th} power law and the dynamic contact width is increased according to a $1/7^{th}$ power law with time.

(iii) super-spreading wetting (V$\gg V_{Th}$): the dynamic contact angle is decreased according to a -2/3^{th} power law and the dynamic contact width is increased according to a $1/3^{th}$ power law.

In order to test three theoretical predictions, the experiments were performed where the droplet was examined from perpendicular to the electrode array at a fixed voltage. Voltage steps of 10V step in between 40V to 270V were used and back to 0V between steps. The dynamic contact angle and the dynamic contact width were extracted by image processing and it was limited at the higher voltages due to the droplet shape. For these experiments the threshold voltage was 230V $\pm$ 2V. Main advantage of this approach is the equilibrium contact angle can be tuned by adjusting the applied voltage. It is complementary to the electrowetting on dielectric (EWOD) and also it does not have contact with any external electrode.

The experimental data, $\Delta\theta vstime$ of the partial wetting (100V to 200V) has demonstrated the exponential approach to the equilibrium. The wetting behaviour was increased as the voltage was reached to the threshold voltage and also the data demonstrated the time constant follows the $\theta_e^{-7/2}$ power law as theoretically predicted. At higher voltage (such as above 250V), the droplet was spread to a thin film which is $\sim 10\times$ smaller than the actual droplet height but the width of the droplet from y-direction is unchanged (no spreading across the electrodes).

The experimental data of the 200V to 270V such as natural logarithmic of the contact angle versus natural logarithmic of the time has shown clear linear dependence (where the gradient is the n) which confirms the power law relationship ($\theta \propto 1/(t+t_o)^n$). The exponent in time goes from $-2/7^{th}$ power law to $-2/3^{th}$ power law as the voltage is increased from 200V to 270V as theoretically predicted [85]. The magnitude of the spreading exponent (n) is increased as the voltage is increased.

The super-spreading regime power law ($d \sim (t + t_o)^{1/3.39}$) has found at 270V which is consistent with the theoretically predicted power law ($d \sim (t + t_o)^{1/3}$) [85]. These data illustrates the rate of spreading stripes of liquid is controlled by voltage. Wetting strength depends on the voltage, electrode periodicity, liquid properties such as surface tension and viscosity.

Droplet dewetting: Dewetting was illustrated how the contact angle evolves with time as the voltage is removed. The strength of the dewetting from the partial wetting (where the initial $\theta \geq 40^o$) and super-spreading regime (where the initial $\theta \leq 15^o$) has quantified in terms of θ and time. At higher voltage (230V to 290V) the data has shown the offset because the droplet shape was not changed over this period. However for each voltage the equilibrium contact angle ($75^o \pm 3^o$) is obtained at 400msec.

7.2 Solid gratings

Our new approach has shown to fabricate the solid grating device in micrometer scale features (for example pitch of the grating from 20μm, 40μm and 80μm). The simple fabrication process has demonstrated how the 0^{th} order of the diffraction spots is suppressed by adjusting the applied voltage whilst UV curing [103].

Initial a 10 $\pm$ 1 μL droplet of UV curable resin solution (which is diluted in acetone with 10% by weight) was dispensed on the interdigitated electrode and it formed into a drying shape. A 10 kHz square signal was applied to create wrinkles at oil/air interface.

When a laser light 633nm wavelength was illuminated in transmission, a series of diffraction spots were created due to the periodic variation in the thickness of the UV epoxy layer. Well the intensities of the diffracted spots depend on the amplitude of the wrinkle which depends on the applied voltage. The minimum 0^{th} order was achieved at 105$\pm$5V for 10μm, 20μm and 40μm line width electrode array. These samples were cured with UV light for 720sec whilst the voltage was

adjusted to keep the intensity of the 0^{th} order minimum. The solid grating profile was obtained using Stylus profilometer. The average peak to peak amplitude for each line width of the electrode 10μm, 20μm and 40μm was $A = 0.8110\mu m$, $0.8410\mu m$ and $0.810\mu m$ respectively.

The minimum 0^{th} order intensity was achieved in the 10μm line width electrode array than the higher line width electrode devices because it has a closet sinusoidal shape. It also concluded that the intensities of the diffraction spots depend on the amplitude and shape of the wrinkle. These devices were illustrated low sensitivity to the polarization. The gratings are consisted 250 periods covering an area of 5mm.

7.3 Wrinkle dynamics

Our approach has shown to create a uniform thin layer of 1-decanol oil in the pre-fabricated interdigitated electrode array by applying a voltage across IDT and the uniform thickness of oil was independent of the voltage. The thickness of the oil layer was measured using the Mach-Zehnder interferometer. On the application of higher voltages the wrinkles were created at oil/air interface due to the dielectrophoresis. The amplitude depends on the voltage and liquid properties such as surface tension, viscosity and dielectric constant [17, 18].

In order to study the dynamics of the wrinkle switching and relaxing, initially a droplet of 1-Decanol (Dielectric constant 8.1, viscosity 0.113 NsM^{-2} and surface tension 28.4 mNm^{-1}) was dispensed on the center of 40μm line width IDT electrode array which was coated with a 2μm SU8 layer. By application of 300V the droplet was spread into a thin film and wrinkles were evolved at air/oil interface. These wrinkle devices act as a thin sinusoidal phase grating because of their thickness variation. A 543nm green laser was illuminated in transmission and it diffracted from the zero order into the higher order diffraction spots. The intensities of the diffraction spots and a number of the spots are related to the

amplitude of the wrinkle.

To investigate the relationship between the phase delay and applied voltage, quasi-static experiments were performed for 1-decanol oil where the voltage was linearly increased from minimum voltage to maximum voltage. The linear increment in the voltage was caused the evolution of the amplitude therefore the intensities of the diffraction orders was varied between maxima and minima. The phase delay values were extracted by fitting the actual data to the theoretical prediction (the Fraunhofer approximation for a thin sinusoidal phase grating) using manual methods. This assumes the wrinkle profile was sinusoidal during the evolution. The data shows that the phase delay is directly proportional to the applied voltage squared where the phase delay is directly proportional to the amplitude of the wrinkle which is consistent with theoretical prediction by Brown et al [17, 18] such as A $\propto V^2$.

An investigation of the switching characteristics of the device was performed by applying a 2.5 kHz square signal, which was modulated with another 100Hz square signal, to IDT electrode array. Therefore the amplitude of the wrinkle was discontinuously switched between the flat surface and higher amplitude since the voltage was discontinuously switched between a high voltage and a low voltage. The amplitude of the low voltage is 42V and high voltages are 304V, 278V, 257V, 230V, 212V, 194V, 161V and 127V. The intensities of the diffraction spots were recorded for switching and relaxing of a 1-decanol oil on electrode line widths of 40μm and 80μm at thicknesses ranging from 17.2μm to 24.5μm. The actual data was fitted with a theoretical prediction, square of the Bessel function of the first kind, to show amplitude of the wrinkle consistent with thin sinusoidal phase grating theory.

In switch off condition, the switching off time, τ, depends on the restorative force which is limited by the surface tension and viscosity of the oil. The data for 1-decanol oil on electrode line widths of 40μm and 80μm at thicknesses ranging from 13μm to 26μm have shown that switch off time is unequal for each volt-

age. This could be due to the oil evaporation from one voltage experiment to another voltage experiment. A first approximation for the τ has been derived by considering the pressure on the system. This model provides the relationship between the switch off time and particular parameters such as line width of the electrode, thickness of the oil layer, surface tension and viscosity of the liquid. The experimental has shown a correlation between the $\tau \propto p^4/h^3$

7.4 Future work

7.4.1 Dielectrowetting

In dynamics of dielectrowetting, we have a formulated a theory of voltage induced stripe spreading (anisotropic spreading) and it has experimentally demonstrated with a 1, 2 propylene glycol droplet using LDEP. The equilibrium contact angle and the strength of the super spreading were controlled by applied a voltage. However for axisymmetric (isotropic) spreading the same principles apply such as;

(i) At partial wetting regime, the contact angle is exponentially approach to the equilibrium contact angle with time and it follows $\Delta\theta \propto exp(-\beta\theta_e^{10/3}t)$.

where $\beta = k(\gamma_{LV}/\eta)(27\pi/4\Omega)^{1/3}\theta_e^{10/3}V$, $\Delta\theta = \theta - \theta_e$ and θ_e is the equilibrium contact angle.

(ii) At complete wetting ($V \simeq V_{th}$) the dynamic contact angle is decreased according to a -3/10 power law.

(iii) At complete wetting ($V \gg V_{th}$) the dynamic contact angle is decreased according to a -3/4 power law.

The cross-over from an exponent of -3/10 to -3/4 is the same as for topography induced super spreading, but with voltage rather than roughness controlling the transition and its strength.

Our dielectrowetting experiments have shown that an isotropic liquid droplet

can easily spread along the electrodes and then this behaviour is suggested a radial electrode geometry rather than stripes geometry (0-offset) to produce an axisymmetric spreading. A big challenge is to design radial electrodes where the periodicity of the electrode should be constant in the geometry. Well this theory and formulae can be demonstrated using an electrowetting configuration since this theory applies equally to dielectrowetting and electrowetting.

Two liquid spreading:

A preliminary experiment of a droplet spreading in a another liquid has shown voltage square law where one is high polar liquid than the another liquid and these liquids are immiscible liquids.

At higher voltage, 240V, this droplet was spread into a thin film and then at no voltage condition this film was divided into two equal volume droplets. At same voltage these two droplets were spread and combined as a thin film, and then at no voltage condition this film was formed into a single droplet. These fascinating scenes are needed to be explained in more scientific way, for example the droplet should be examined using a high speed camera which helps us to understand the desegregation.

It also unclear how the scaling of another liquid will affect the wetting and dewetting. In dewetting condition, it may be possible to create more than two droplets using high denser liquid.

7.4.2 Wrinkle dynamics

Our approach has shown how to create the undulations at air/oil interface. The wrinkle switching and relaxing experiments were performed. We have observed the oil evaporation during the experiments from one voltage to another voltage which led a change in thickness of the oil layer.

Due to the lack of thickness measurement we are not concluding the exper-

imental data with the theoretical prediction. Furthermore experiments are required where the oil evaporation should be avoided to get the consisted results and the thickness of the oil should be measured for every repetition.

Well the switch time of the wrinkles have shown a correlation between the t_{on} and thickness of the oil layer. We have collaborated with University of Strathclyde for a mathematical model of the wrinkle switching.

7.4.3 Feasible applications

- The ability to control the contact angle by dielectrowetting has significance for processes such as droplet-based microfluidics, lab on a chip systems, liquid-based optics, coating and other processes where enhanced or controlled spreading are desired.

- Dielectrowetting can be combined with superoleophobicity to create control of non-aqueous droplets.

- Superspreading approach is a complementary to the use of topographic of the solid surface or by adding surfactant to the liquid for modification of the liquid. This approach has relevance for control of films including inking and painting [106].

- In our approach, variable focal lens can be fabricated; it consists a droplet would be sitting on a centre of the radial electrodes and another liquid filled in an encapsulated box on top of the electrodes. The two liquids are immiscible liquids having different dielectric constant and similar density. L-DEP is able to spread droplets and that there is an initial regime, covering a very wide contact angle range (130^o).

- Using our electrode geometry (IDT) is possible that travelling wave dielectrophoretic force can be created to manipulate the cell. Mainly this kind of microfluidics system consists of number of parallel which is capped with

a rectangular straight micro channel, and operated under an AC voltage with phase shift at neighbouring electrodes. A solution of cells and a liquid is transmitted in the channel with a fixed pressure and then cell will be responded depending on the frequency of applied AC signals [107].

- The solid grating fabrication technique could also apply with more complex electrode geometries to the creation of light collection for solar cells or to the creation of concentration optical components for three dimensional stereoscopic displays [103].

References

[1] H Pellate. Force acting on the surface of separation of two dielectrics. *The Proceedings of meetings of the Academy of Sciences. Paris*, 119:675–678, 1894.

[2] T B Jones, M P Perry, and J R Melcher. Dielectric Siphons. *Science*, 174(4015):1232–1233, 1971.

[3] T B Jones, M Gunji, M Washizu, and M J Feldman. Dielectrophoretic liquid actuation and nanodroplet formation. *Journal of applied physics*, 89(2):1441–1448, 2001.

[4] T B Jones. On the relationship of dielectrophoresis and electrowetting. *Langmuir*, 18(11):4437–4443, 2002.

[5] P Tabeling. *Introduction to Microfluidics*. Oxford Press, 2005.

[6] D Mark, S Haeberle, G Roth, F Stetten, and R Zegerle. Microfluidic lab-on-a-chip platforms: requirements, characteristics and applications. *Chemical Society Reviews*, 39(3):1153–1182, 2010.

[7] K Ragil, J Meunier, D Broseta, J O Indekeu, and D Bonn. Experimental observation of critical wetting. *Physical Review Letters*, 77(8):1532–1535, 1996.

[8] E Bertrand, D Bonn, D Broseta, H Dobbs, J O Indekeu, J Meunier, K Ragil, and N Shahidzadeh. Wetting of alkanes on water. *Journal of Petroleum Science and Engineering*, 33(1-3):217–222, 2002.

[9] F Mugele and J C Baret. Electrowetting: from basics to applications. *Journal of Physics: Condensed Matter*, 17(28):705–774, 2005.

[10] R Shamai, D Andelman, B Berge, and R Hayes. Water, electric, and between on electrowetting and its applications. *Soft Matter*, 4(1):38–45, 2008.

[11] T.B. Jones. Liquid dielectrophoresis on the microscale . *Journal of Electrostatics*, 51-52:290–299, 2001.

[12] C C Cheng, C A Chang, and Yeh J A. Variable focus dielectric liquid droplet lens. *Optics Express*, 14(9):4101–4106, 2006.

[13] Y-C Wang, Y-C Tsai, and W-P Shih. Flexible PDMS micro-lens array with programmable focus gradient fabricated by dielectrophoresis force. *Microelectronic Engineering*, 88(8):2748–2750, 2011.

[14] L H Tanner. The spreading of silicone oil drops on horizontal surfaces. *Journal of Physics D: Applied Physics*, 12(9):1473–1484, 1979.

[15] D Bonn, J Eggers, J Meunier, and E Rolley. Wetting and spreading. *Reviews of Modern Physics*, 81(2):739–805, 2009.

[16] R L Hoffman. A study of the advancing interface. I. Interface shape in liquid-gas systems. *Journal of Colloid and Interface Science*, 50(2):228–241, 1975.

[17] C V Brown, W Al-Shabib, G G Wells, G McHale, and M I Newton. Amplitude scaling of a static wrinkle at an oil-air interface created by dielectrophoresis forces . *Applied Physics Letters*, 97(24):242904–3, 2010.

[18] C V Brown, G G Wells, M I Newton, and G McHale. Voltage-programmable liquid optical interface . *Nature Photonics*, 3(7):403–405, 2009.

[19] E Schaffer, T Thurn-Albrecht, T P Russell, and U Steiner. Electro hydrodynamic instabilities in polymer films. *Europhysics Letters*, 53(4):518–524, 2001.

[20] E Schaffer, T Thurn-Albrecht, T P Russell, and U Steiner. Electrically induced structure formation and pattern transfer. *Nature*, 403(6772):874–877, 2000.

[21] R V Caster and O K Matar. Dynamics and stability of thin liquid films. *Reviews of Modern Physics*, 81(3):1131–1198, 2009.

[22] A W Adamson and A P Gast. *Physical Chemistry of Surface*. Wiley-Interscience, 1997.

[23] G T Barnes and I R Gentle. *Interfacial Science*. Oxford press, 2005.

[24] P G de Gennes, F Brochard-Wyart, and D Quere. *Capillarity and Wetting Phenomena: Drops, Bubbles, Pearls, Waves*. Springer, 2003.

[25] D Bonn, E Bertrand, N Shahidzadeh, K Ragil, H Dobbs, A I Posazhennikova, D Broseta, J O Indekeu, and J Meunier. Complex wetting phenomena in liquid mixtures: Frustrated-complete wetting and competing intermolecular forces. *Journal of Physics: Condensed Matter*, 13(21):4903–4914, 2001.

[26] N Shahidzadeh, E Bertrand, J P Dauplait, J c Borgotti, and D Bonn. Effect of wetting on gravity drainage in porous media. *Transport in Porous Media*, 52(2):213–227, 2003.

[27] N Shahidzadeh, D Bonn, K Ragil, D Broseta, and J Meunier. Sequence of two wetting transitions induced by tuning the Hamaker constant. *Physical Review Letters*, 80(18):3992–3995, 1998.

[28] P G de Gennes. Wetting: statics and dynamics. *Reviews of Modern Physics*, 57(3):827–863, 1985.

[29] D Quere. Wetting and roughness. *Annual Review of Materials Research*, 38:71–99, 2008.

[30] T Onda, N Shibuichi, N Satoh, and T Tsuji. Super water-repellent fractal surfaces. *Langmuir*, 12(9):2125–2127, 1996.

[31] J Bico, C Tordeux, and D Quere. Rough wetting. *Europhysics Letters*, 55(2):214–220, 2001.

[32] P G de Gennes, F Brochart-Wyart, and D Quere. *Capillarity and Wetting Phenomena: Drops, Bubbles, Pearls, Waves*. Springer, 2003.

[33] H Dahms. Electrocapillary Measurements at the Interface Insulator-Electrolytic Solution. *Journal of The Electrochemical Society*, 116(11):1532–1534, 1969.

[34] B Berge and J Peseux. Variable focal lens controlled by an external voltage: An application of electrowetting. *The european physical journal E*, 3(2):159–163, 2000.

[35] H Moon, S K Cho, R L Garrell, and C J Kim. Low voltage electrowetting-on-dielectric. *Journal of Applied Physics*, 92(7):4080–4087, 2002.

[36] C Quilliet and B Berge. Electrowetting: a recent outbreak. *Current Opinion in Colloid and Interface Science*, 6(1):34–39, 2001.

[37] A Banpurkar, K P Nichols, and F Mugele. Electrowetting-based microdrop tensiometer . *Journal of Applied Physics*, 24(19):10549–10551, 2008.

[38] M Pollack, R B Fair, and A D Shenderov. Electrowetting-based actuation of liquid droplet for micro fluidic applications. *Applied physics letters*, 77(11):1725–1726, 2000.

[39] R B Fair. Digital microfluidics: is a true lab-on-a-chip possible? *Microfluidics and Nanofluidics*, 3(3):245–281, 2007.

[40] R A Hayes and B J Feenstra. Video-speed electronic paper based on electrowetting. *Nature*, 425(6956):283–285, 2003.

[41] S Kuiper and B H W Hendriks. Variable-focus liquid lens for miniature cameras. *Applied physics letters*, 85(7):1128–1130, 2004.

[42] F Li and F Mugele. How to make sticky surfaces slippery: Contact angle hysteresis in electrowetting with alternating voltage. *Applied Physics Letters*, 92(24):244108–244111, 2008.

[43] H A Pohl. *Dielectrophoresis: The behaviour of neutral matter in nonuniform electric fields*. Cambridge University Press, 1915.

[44] H A Pohl. Some effects of non-uniform field on dielectrics. *Journal of Applied Physics*, 29(8):1182–1188, 1958.

[45] H A Pohl. The motion and precipitation of suspensoids in divergent electric field. *Journal of Applied Physics*, 22(2):869–871, 1978.

[46] R Pethig. Using inhomogeneous AC electric fields to separate and manipulate cells. *Critical Reviews in Biotechnology*, 16(4):331–348, 1996.

[47] H A Pellat. Some effects of nonuniform fields on dielectric. *Journal of Applied Physics*, 29(8):1182–1188, 1958.

[48] H Morgan, A G Izquierdo, D Bakewell, N G Green, and A Ramos. The dielectrophoretic and travelling wave forces generated by interdigitated electrode arrays: analytical solution using Fourier series. *Journal of Physics D: Applied Physics*, 34(10):1553–1561, 2000.

[49] G Wells. *Voltage Programmable Liquid Optical Devices* . PhD thesis, 2009.

[50] K Khoshmanesha, S Nahavandia, S Baratchib, A Mitchellc, and K Kalantar-Zadehc. Dielectrophoretic platforms for bio-microfluidic systems. *Biosensors and Bioelectronics*, 26(5):1800–1814, 2011.

[51] A R Minerick, R Zhou, P Takhistov, and H-C Chang. Manipulation and characterization of red blood cells with alternating current fields in microdevices. *Electrophoresis*, 24(21):3703–3717, 2003.

[52] Z Gagnon and H-C Chang. Aligning fast alternating current electro osmotic flow fields and characteristic frequencies with dielectrophoretic traps to achieve rapid bacteria detection. *Electrophoresis*, 26(19):3725–3737, 2003.

[53] P R Gascoyne, J Noshari, T J Anderson, and F F Becker. Isolation of rare cells from cell mixtures by dielectrophoresis. *Electrophoresis*, 30(8):1388–1398, 2009.

[54] Q Ramadan, V Samper, D Poenar, Z Liang, C Yu, and T M Lim. Simultaneous cell lysis and bead trapping in a continuous flow microfluidic device. *Sensors and Actuators B: Chemical*, 113(2):944–955, 2006.

[55] R Prakash, R Paul, and K V I S Kaler. Liquid DEP actuation and precision dispensing of variable volume droplets. *Lab on a Chip*, 10(22):3094–3102, 2010.

[56] K V I S Kaler and R Prakash. Dispensing and bio-functionalization of giant unilamellar vesicles on a chip. *Proceedings of the 13th international conference on electrostatics: Electrostatics 2011*, 301(1):1–4, 2011.

[57] R Prakash and K V I S Kaler. Microbead dispensing and ultralow DNA hybridization detection using liquid dielectrophoresis. *Sensors and Actuators B-Chemical*, 169:274–283, 2012.

[58] D Chung and K V I S Kaler. Integrated liquid and droplet dielectrophoresis for biochemical assays. *Microfluidics and Nanofluidics*, 8(4):445–456, 2010.

[59] R Prakash and K V I S Kaler. DEP actuation of emulsion jets and dispensing of sub-nanoliter emulsion droplets. *Lab on a Chip*, 9(19):2836–2844, 2009.

[60] C Hui-Ying, Z Yue-Lin, L Yan, Z He-Teng, Y Le, and L Di. Manipulation and Separation of Particles of Metal Oxides by Dielectrophoresis. *Chemical Research in Chinese Universities*, 18(6):1034–1037, 2010.

[61] E Hecht. *Optics*. Addison Wesley, 1987.

[62] E Hallstig, J Stigwall, T Martin, L Sjoqvist, and M Lindgren. Fringing Fields in a liquid crystal spatial light modulator for beam steering. *Journal Of Modern Optics*, 51(8):1233–1247, 2004.

[63] J Chen, P J Bos, and H Vithana. An electro optically controlled liquid-crystal diffraction grating. *Applied Physics Letters*, 67(18):2588–3, 1995.

[64] W M Gibbons and S T Sun. Optically generated liquid-crystal gratings. *Applied Physics Letters*, 65(20):2542–2544, 1994.

[65] S Matsumoto, M Goto, S W Choi, Y Takanishi, K Ishikawa, H Takezoe, G Kawamura, I Nishiyama, and H Takada. Phase grating using a ferroelectric liquid-crystal mixture with a photo curable liquid crystal. *Journal of Applied Physics*, 99(11):113709–5, 2006.

[66] B Apter, U Efron, and E Bahat-Treidel. On the fringing-field effect in liquid-crystal beam-steering devices. *Applied Optics*, 43(1):11–19, 2004.

[67] D P Resler, D S Hobbs, R C Sharp, L J Friedman, and T A Dorschner. High-efficiency liquid-crystal optical phased-array beam steering. *Optics Letters*, 21(9):689–691, 1996.

[68] M Lee, P Pichon, C Sauvan, J C Rodier, P Lalanee, M Hutley, D Joyeux, P Chavel, E Cambril, and Y Chen. Transmission blazed-binary gratings for visible light operation: performances and interferometric characterization. *Journal Of Optics A-Pure And Applied Optics*, 5(5):244–249, 2003.

[69] R A Guerrero, J T Barretto, J L Uy, I B Culaba, and B O Chan. Effects of spontaneous surface buckling on the diffraction performance of an Au-coated elastomeric grating. *Optics Communications*, 270(1):1–7, 2007.

[70] C Harrison, C M Stafford, WH Zhang, and A Karim. Sinusoidal phase grating created by a tunably buckled surface. *Applied Physics Letters*, 85(8):4016–4019, 2004.

[71] J W Goodman. *Introduction to Fourier Optics*. Standford University, Third edition, 2004.

[72] C L Trabi. *Investigation of flexoelectricity and ionic contamination in nematic liquid crystals* . PhD thesis, 2009.

[73] N Doy. *Characterising Room Temperature Ionic Liquids With Acoustic Wave Devices* . PhD thesis, 2010.

[74] N J Shirtcliffe, S Aqil, C Evans, G McHale, M I Newton, C C Perry, and P Roach. The use of high aspect ratio photoresist (SU-8) for super-hydrophobic pattern prototyping. *Journal of Micromechanics and Microengineering*, 14(10):1384–1389, 2004.

[75] C Kowalski. Online dektak 6m manual, http://www.scribd.com/doc/56615274/dektak-6m-manual, veeco metrology, 2002.

[76] F Thomsen. Practical contact angle measurement, http://www.kruss.de/de/home.html, kruss, 2008.

[77] L H Tanner. The Optics of the Mach-Zehnder Interferometer. *Aeronautical Research Council Reports and Memoranda*, 3069:1–62, 1959.

[78] N J Shirtcliffe, G McHale, S Atherton, and M I Newton. An introduction to superhydrophobicity. *Advances in colloid and interface Science*, 161(1):124–138, 2010.

[79] M Vallet, B Berge, and L Vovelle. Electrowetting of water and aqueous solutions on poly(ethylene terephthalate) insulating films. *Polymer*, 37(12):2465–2470, 1996.

[80] T B Jones, K L Wang, and D J Yao. Frequency-dependent electro mechanics of aqueous liquids: electrowetting and dielectrophoresis. *Langmuir*, 20(2):1441–1448, 2004.

[81] G McHale, C V Brown, M I Newton, G G Wells, and N Sampara. Dielectrowetting Driven Spreading of Droplets. *Physical Review Letters*, 107(4):186101–4, 2011.

[82] G McHale, M I Newton, S M Rowan, and M K Banerjee. The Spreading of small viscous stripes of oil. *Journal of Physics D: Applied Physics*, 28(9):1925–1929, 1995.

[83] G McHale, M I Newton, and N J Shirtcliffe. Dynamic wetting and spreading and the role of topography. *Journal of Physics: Condensed Matter*, 21(46):464122–11, 2009.

[84] G McHale, M I Newton, S M Rowan, and M Banerjee. Topography driven spreading. *Physical Review Letters*, 28(3):6102–6105, 1995.

[85] G McHale, C V Brown, and N Sampara. Voltage Induced Spreading and Super-Spreading of Liquids. *Nature Communications*, 4(1605), 2013.

[86] C Hugh and L E Scriven. Hydrodynamic model of steady movement of a solid/liquid/fluid contact line. *Journal of Colloid and Interface Science*, 35(1):85–101, 1971.

[87] O V Voinov. Hydrodynamics of wetting. *Fluid Dynamics*, 11(5):714–721, 1976.

[88] R G Cox. The dynamics of the spreading of liquids on a solid surface. Part 1. Viscous flow. *Journal of Fluid Mechanics*, 168:169–194, 1986.

[89] G McHale, S M Rowan, and M I Newton. Frenkel's method and the spreading of small spherical droplets. *Journal of Fluid Mechanics*, 27(12):2619–2623, 1994.

[90] G Jin and G Kim. Pressure/Electric-Field-Assisted Micro/Nanocasting Method for Replicating a Lotus Leaf. *Langmuir*, 27(2):828–834, 2011.

[91] A J Das and K S Narayan. Observation of Bessel beams from electric-field induced patterns on polymer surfaces. *Optics Letters*, 34(21):3391–3393, 2009.

[92] S Yang, T N Krupenkin, P Mach, and E A Chandross. Tunable and latchable liquid microlens with photopolymerizable components. *Advanced Materials*, 15(11):940–943, 2003.

[93] F T O'Neill, G Owen, and J T Sheridan. Alteration of the profile of ink-jet-deposited UV-cured lenses using applied electric fields. *Optik*, 116(4):158–164, 2005.

[94] Z Zhan, K Wang, H Yao, and Z Cao. Fabrication and characterization of a spherical lens manipulated by electrostatic field. *Applied Optics*, 48(22):4375–4380, 2009.

[95] D Salac, W Lu, C-W Wang, and Sastry A M. Pattern formation in a polymer thin film induced by an in-plane electric field. *Applied Physics Letters*, 85(7):1161–1163, 2004.

[96] K Amundson, E Helfand, D D Davis, X Qian, S S Patel, and S D Smith. Effect of an electric field on block copolymer microstructure. *Macromolecules*, 24(24):6546–6548, 1991.

[97] C H Wang, P Chen, and C Y Lu. Phase separation of thin-film polymer mixtures under in-plane electric fields. *Physical Review E*, 81(6):061501–9, 2010.

[98] Y Kim, J Francl, B Taheri, and J L West. A method for the formation of polymer walls in Liquid/Crystal polymer mixtures. *Applied Physics Letters*, 72(18):2253–2255, 1998.

[99] A E Buyuktanir, N Gheorghiu, J L West, M Mitrokhin, and B Holter. Field-induced polymer wall formation in a bistable smectic-A liquid crystal display. *Applied Physics Letters*, 88(3):031101–3, 2006.

[100] H Ren, S T Wu, and Y H Lin. In Situ Observation of Fringing-Field-Induced Phase Separation in a Liquid-Crystal-Monomer Mixture . *Physics Review Letters*, 100(11):117801–4, 2008.

[101] R D Deegan, O Bakajin, and T F Dupont. Capillary flow as the cause of ring stains from dried liquid drops. *Nature*, 389(6653):827–829, 1997.

[102] R D Deegan. Pattern formation in drying drops. *Physical Review E*, 61(1):475–485, 2000.

[103] G G Wells, N Sampara, E E Kriezis, J Fyson, and C V Brown. Diffraction grating with suppressed zero order fabricated using dielectric forces. *Optics Letters*, 36(22):4404–4406, 2011.

[104] C V Brown, G McHale, and N J Mottram. Analysis of a static undulation on the surface of a thin dielectric liquid layer formed by dielectrophoresis forces . *Journal of Applied Physics*, 110(2):024107–5, 2010.

[105] *Online Knovel critical tables, Second edition, 2009.*

[106] F Liu and W Shen. Forced wetting and dewetting of liquids on solid surfaces and their roles in offset printing. *Colloids and Surfaces A: Physicochemical and Engineering Aspects*, 316(1-3):62–69, 2008.

[107] U Lei, C W Huang, J Chen, C Y Yang, Y J Lo, A Wo, and T W Fung. A travelling wave dielectrophoretic pump for blood delivery. *Lab on a Chip*, 9(10):1349–1356, 2009.